ALMA MATER STUDIORUM - UNIVERSITÀ DI BOLOGNA

Dipartimento di Fisica e Astronomia “Augusto Righi”

EXPLORING THE WHITE DWARF COOLING SEQUENCE IN GLOBULAR CLUSTERS

DOTTORATO DI RICERCA IN
ASTROFISICA
Ciclo XXXV

Presentata da: Jianxing Chen

Supervisore:
Prof. Francesco R. Ferraro

Coordinatore Dottorato:
Andrea Miglio

Co-supervisori:
Dr. Mario Cadelano,
Prof. Barbara Lanzoni

Esame finale anno 2023

Settore Concorsuale: 02/C1 - Astronomia, Astrofisica, Fisica della Terra e dei Pianeti
Settore Scientifico Disciplinare: FIS/05 – Astronomia e Astrofisica

© Copyright by **JIANXING CHEN**, 2023
All Rights Reserved

Abstract

White Dwarfs (WDs) are electron-degenerate structures that are commonly assumed to evolve via a pure cooling process, with no stable thermonuclear activity at work. Their cooling rate is adopted as a cosmic chronometer to constrain the age of several Galactic populations, including the disk, Globular Clusters (GCs) and open clusters.
This thesis work is aimed at the study of the WD populations in globular clusters and is articulated in two branches.
The first was focused on the study of the bright portion of the WD cooling sequence. By analyzing high resolution UV data acquired with the Hubble Space Telescope (HST), we compared the WD luminosity functions (LFs) in four Galactic GCs (namely M13, M3, NGC6752, and M5) finding an unexpected over-abundance of WDs in M13 and NGC6752 with respect to M3 and M5. Theoretical models suggest that, consistently with the blue-tail horizontal branch (HB) morphology of M13 and NGC6752, this overabundance is due to a population of slowly cooling WDs, i.e., WDs fading more slowly than in a pure cooling process thanks to an extra-energy source provided by stable thermonuclear burning in their residual hydrogen-rich envelope. This is the first empirical evidence of WDs fading at a slower rate than usually assumed, and has a crucial impact on the use of the cooling sequence as a cosmic chronometer.
The second branch was focused on the search for the companion star to binary millisecond Pulsars (MSP) in the globular clusters M13 and NGC 6652: the identified companions turned out to be helium-core WDs, and provided a invaluable constraints on the mass of the neutron star and the epoch of the MSP formation.

Dedicated to the future.

Contents

Chapter 1

Introduction

1.1 Globular Clusters

Globular Clusters (GCs) are spheroidal agglomerates of large numbers of stars ($\sim 10^4 - 10^6$ stars) bound together by their mutual gravitational interactions, they are among the oldest (typical values of about 12 Gyr) and metal-poor ([Fe/H] $\sim -2 - -1$) stellar systems and characterized by being bright (Mean absolute magnitude $M_V \approx -7$) and compact (half-light radius up to a few tens of pc, typically $\sim 3 - 5$ pc) in the Galaxy (commonly referred to as Galactic Globular Clusters (GGCs)). Thus far, around 162 GCs (Baumgardt et al., 2021) have been discovered in the Galaxy and mainly distributed in the halo, bulge, and thick disk.

For a long time, globular clusters have been used to constrain stellar evolution models under the assumption that they are composed of a Simple Stellar Population (SSP), a homogeneous group of stars that share the same age and initial chemical composition. While over the past two decades, it has been discovered that nearly all GGCs contain multiple populations within them. The internal variations of some light elements (e.g. He, C, N, O, and Na) were revealed with the ground-based spectroscopic surveys (e.g. Carretta et al., 2009a,b,c; R. Gratton et al., 2004), and the unprecedented view of multiple population pattern were presented with the space-based telescope, especially in the UV/near-UV band. (Milone et al., 2017; Piotto et al., 2015).

The formation of most GGCs occurred 12.5 billion years ago, corresponding to a redshift of $z \sim 5$, which was not only the peak time for the formation of the progenitor stars of GGCs,

but also a crucial stage in the early formation of the Galaxy and even the re-ionization of the universe (Renzini, 2017). GCs play an important role in connecting individual star to their host Galaxy (Bica et al., 2016), as well as in exploring early Galaxy and special stellar populations (Moehler et al., 2008). Figure 1.1 shows an example of the colored image of globular cluster M3, which is one of the samples of the work in this thesis.

Figure 1.1: HST colored image of globular cluster M3. Credit: ESA/Hubble & NASA, G. Piotto et al.

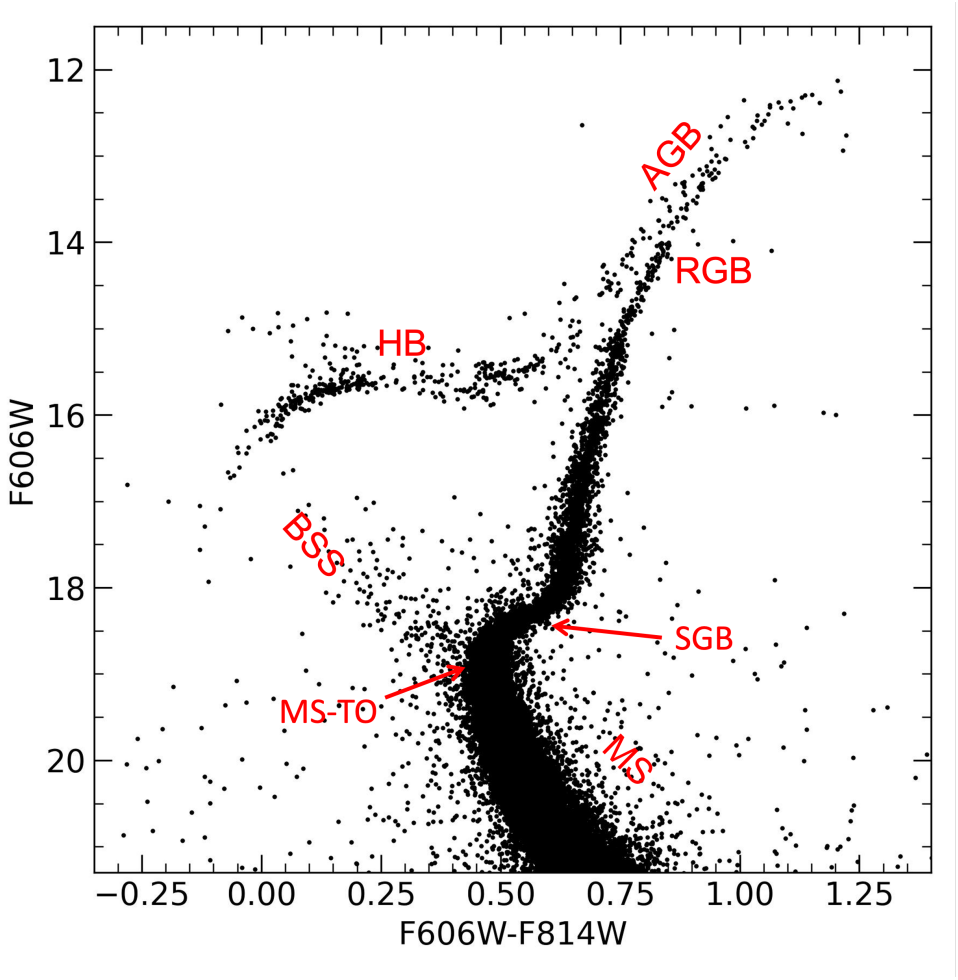

Figure 1.2: An example of optical CMD of globular cluster M3, data from Nardiello et al. (2018)

1.2 Stellar Evolutionary Phases

1.2.1 CMD

The evolutionary track of individual stars is commonly represented in an Hertzsprung–Russell Diagram (HR-diagram) with temperature on the horizontal axis and luminosity on the vertical axis, while its observational counterpart, the Color Magnitude Diagram (CMD), is more frequently to describe the population of stars in clusters using a combination of magnitudes in different photometric band. Like an HR diagram, the CMD is also composed of the 'color', represented by difference in measured magnitudes (blue mag minus red mag) as the x-axis, and the 'luminosity', represented by one of the admired magnitudes as the y-axis.

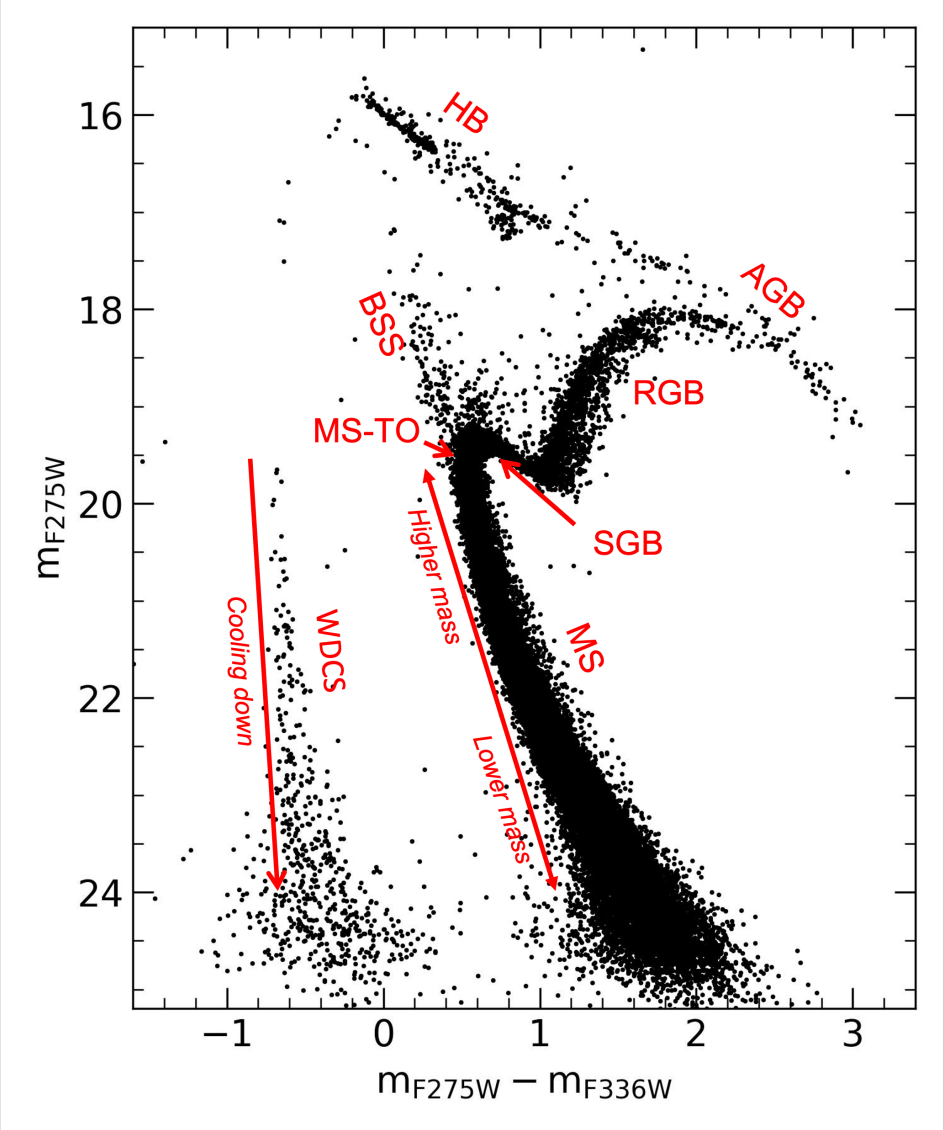

Figure 1.3: An example of near-UV CMD of globular cluster M3.

As the stars in clusters share almost the same distance from the observer, the relative magnitudes and color index of these stars are dependent on their physical properties, such as surface temperature and intrinsic luminosity. On the other hand, several stellar sequences in GGCs can be well reproduced by isochrones, which are obtained by connecting the dots of evolutionary tracks at the same time. This means that GCs are still good approximations of SSP and ideal astrophysical laboratories to explore stellar evolution.

CMD is employed to graphically depict the properties of globular clusters and the target objects throughout this thesis. An example of the CMD of globular cluster M3, one of

target object in my work, is shown in Figure 1.2. With the exception of the WD cooling sequence, which is too faint to be visible, almost all the evolutional sequences are clearly present. In the optical band (F606W, F814W, see section 1.6), RGB stars are the brightest stars, and their surface temperature drops (trend to redder) along the luminosity increases (radius increases). The horizontal branch stars are arranged in a morphology that tends to be horizontal, as described by their names. While at different wavelengths, the CMD of GCs will be completely different, as demonstrated by the near-UV (F275, F336W, see section 1.6) CMD of M3 shown in Figure 1.3. HB stars become the brightest branch and the RGB stars are strongly suppressed, even luminosity decreases in redder color, while the hottest WDs are comparable to MS-TO stars. The evolutionary sequences are briefly introduced in following section.

1.2.2 The evolutionary phases

All potential stellar evolutionary phases, ranging from the Zero-Age Main Sequence to the final phase, WD Cooling sequence, are highlighted in Figure 1.3 (see also Figure 1.2).

- When the internal pressure of interstellar molecular clouds can't prevent the gravitational collapse due to the so-called *Jeans instability*, the formation of a protostar begins. It will then continually contract until the center reaches the ignition temperature of nuclear reactions. After several million years, it will settle down to the **Main Sequence (MS)** and a star's life will start.

  During the phase of the MS for solar-type stars, the interior energy produced from the transmutation of Hydrogen to Helium through the *p-p chain* (for stars with masses $0.4-1.2\ M_{\odot}$) to maintain the stability, this is the longest stage in a star's life and can reach $\sim$ 10 Gyr for solar-type stars. The energy emitted follows the *Stefan-Boltzmann law*, and the center nuclear reaction rates are dependent on the central temperature. However, massive stars with masses larger than $1.2\ M_{\odot}$ reach a temperature large enough to produce energy through the *CNO-Cycle*, with a higher sensitivity to temperature.

  Along the MS, stars with larger masses tend to have higher temperatures and higher luminosities, while stars with lower mass such as solar-type stars, are characterized by lower temperatures and lower luminosities, see the arrow line in Figure 1.3. Since massive stars have faster evolution rates, the bend off of the Main Sequence will move downwards to lower mass stars, going from upper to lower. The region extending from low-mass stars to high-mass stars is where a class of objects known as **Blue Straggle**

Star (BSS) can be found. BSS are not part of standard single stellar evolution theory, so they will not be discussed here (F. R. Ferraro et al., 1992, 1993; Hills et al., 1976; Leonard, 1989; McCrea, 1964; Portegies Zwart et al., 2019; Sandage, 1953; Zinn et al., 1976).

The stellar evolutionary history and all physical properties are uniquely determined by the mass and composition of the star, following the so-called *Vogt-Russell Theorem* (Carroll et al., 2017). While it is not a rigorous law, it is highly effective for qualitatively analyzing stellar evolution. The mass is considered the most important parameter for stellar evolution:

- $M_* \lesssim 0.01\ M_\odot$: Objects that are too small to reach the ignition of hydrogen-burning, like Jupiter, will remain as gas giant planets;
- $0.01\ M_\odot \lesssim M_* \lesssim 0.08\ M_\odot$: Its mass is still too small to fuse hydrogen in the core, so it will become a type of sub-stellar object called brown dwarfs, instead of reaching the MS.
- $0.08\ M_\odot \lesssim M_* \lesssim 0.4\ M_\odot$: These stars are real stars that will ignite hydrogen in their cores and reach the main sequence, but they will live for a very long time, their cores will not reach temperatures high enough to fuse helium or undergo the triple-alpha process. In theory, they will eventually evolve into helium-core white dwarfs, but they will require longer than the age of the universe to do so (see section 1.3.2.)
- $0.4\ M_\odot \lesssim M_* \lesssim 1.2\ M_\odot$: Solar-type stars, as discussed, will experience the *p-p chain* and the *Triple-alpha process*, and eventually end as carbon-oxygen core white dwarfs, which is the most common fate of stars.
- $1.2\ M_\odot \lesssim M_* \lesssim 8\ M_\odot$: Similar to the last one. While the temperature at the core of a star may be high enough to fuse hydrogen through the *CNO-cycle*, it may not be hot enough to burn carbon to neon.
- $8\ M_\odot \lesssim M_*$: Massive stars have a very short lifespan on the main sequence and primarily fuse hydrogen through the *CNO-Cycle*. They may form massive O-Ne-Mg White dwarfs, but if their core is larger than $1.4\ M_\odot$, the so-called *Chandrasekhar limit*, they may end their lives as neutron stars or black holes after a spectacular explosion.

- During the nuclear reaction in the core, as hydrogen is consumed and the helium-core mass increases, the effective temperature and surface luminosity slowly and monotonically increase, while the star slightly contracts until it completely exhausts the hydrogen in the core. The end of this process is marked by the **Main Sequence Turn-Off Stars (MS-TO)**, which roughly corresponds to the hottest point on the main sequence.

- When a star exhausts the central hydrogen, it remains a helium core and does not contribute to energy production because the temperature is too low for igniting the helium. At the **Sub-Giant Branch (SGB)** stage, the helium core continually increases, as the nuclear hydrogen burning at the base of thick shell. With the stellar core contracting and the envelope expanding, the effective temperature drops and the surface luminosity remains almost constant or slightly increases. This transitional phase lasts several million to one billion years depending on their masses. For intermediate-mass or massive stars, the duration can even be too short to cause the so-called *Hertzsprung gap*, as only a few stars can be observed.

  When intermediate or massive stars experience an expansion of their outer layers, the cooling of these layers and a significant increase in opacity leads to more efficient energy trapping in the envelope, further promoting the expansion of the outer layers. While the difference in low-mass stars is that the helium-core is degenerate.

- As the star's envelope expands, its effective temperature decreases and photospheric opacity increases, resulting in the formation of an important structure, the convection zone. The growing convection zone extends to the interior region, making energy transport to the surface highly efficient, causing the star to enter the **Red Giant Branch (RGB)** and rapidly upward along the branch. For low-mass stars ($0.4\ M_\odot \lesssim M_* \lesssim 2.3\ M_\odot$), the partially degenerate helium core is surrounded by a hydrogen-burning shell. At this stage, the effective temperature is too low to ignite the central helium. As the core mass grows, its contraction releases gravitational energy, raising the temperature in both the core and the shell, which in turn, increases the rate of nuclear reactions in the outer layer and boosts the growth of the helium core mass. In this feedback loop, the energy produced is more than enough to power the star's luminosity. The surplus energy drives the expansion of the stellar envelope against its own gravity, causing the atmosphere to grow by a factor of ~ 200 and resulting in a brighter but cooler star, the path is essentially the same as the Hayashi track. The

process continues until thermal instability is reached, resulting in the classical portion of the gas igniting He-burning in a partially degenerate environment explosively at the tip of the RGB: this event is *He-flash*. The thermal runaway being independent of the star's total mass means the magnitude of the tip RGB can be utilized as a standard candle for measuring distances. However, the entire process only persists for several seconds and the majority of the energy never reaches the surface.

During the convective process in the envelope, it progressively penetrates the interior until it reaches an area contaminated by fused materials from thermonuclear reactions, bringing the fusion products to the surface for the first time and increasing the Helium abundance on the surface, which process is referred to as *the first dredge-up*. When the H-burning shell encounters a discontinuity, the rate of the star's ascent up the RGB temporarily decreases and may even temporarily reverse, causing the star to temporarily stall, which is seen as the *RGB-bump* in the luminosity function.

Intermediate-mass and massive stars are massive enough to ignite helium in their cores under classical conditions. As the total mass increases, the contraction of the core is faster, shortening the time needed to reach the temperature for helium ignition, resulting in a significantly shorter lifespan for massive stars.

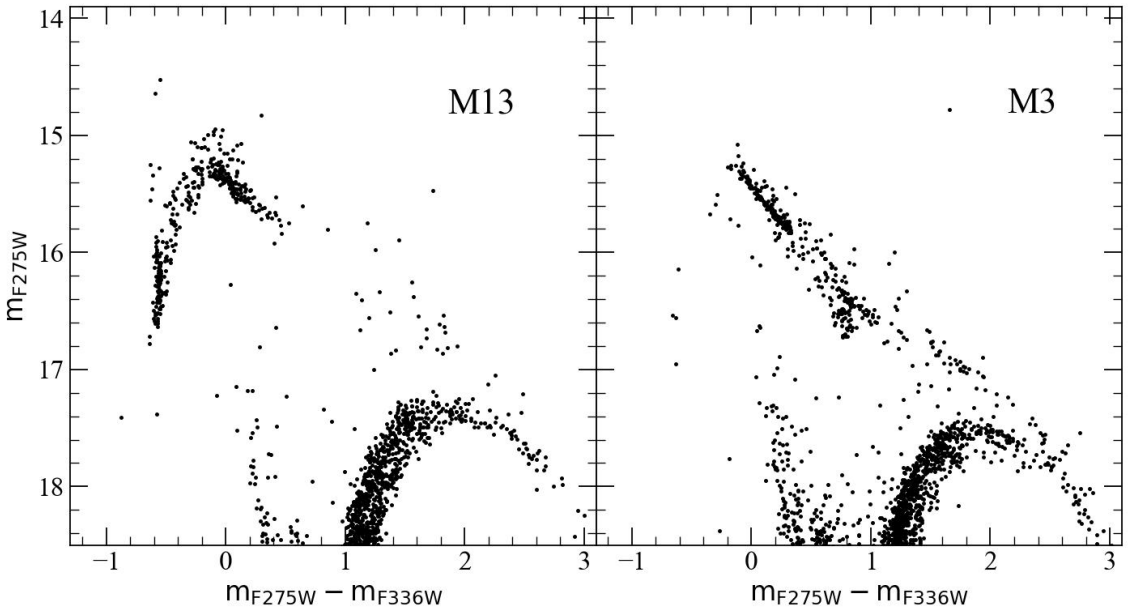

Figure 1.4: The near-ultraviolet CMDs of M13 and M3 are zoomed in on the horizontal branch region.

- One million years after the helium-flash in the core, the star reaches the **Horizontal Branch (HB)**, where its surface luminosity dramatically decreases and degeneracy is entirely removed. This stage of evolution is similar to the main sequence but involves a hydrogen burning shell and helium burning in the core, instead of just hydrogen. In general, the positions along the horizontal branch are dependent on the masses of the stars.

  Low-mass stars that have undergone a helium flash have similar masses of the helium core, so the position along the horizontal branch depends on the mass of the stellar envelope. Smaller envelope stars result in higher surface temperatures and are located on the blue side of the horizontal branch, while larger envelope stars are located on the red side. As shown in Figure 1.4, the HB stars in the blue extension of M13 are populated by lower-mass stars, while in M3 the HB stars are more likely to be populated by higher-mass stars. When HB stars have large stellar envelopes, they can populate a sort of *red clump* (e.g. 47Tuc), which can mislead the identification of red giant branch stars in the field, while asteroseismology is a powerful method that can be used to distinguish them (Bedding et al., 2011). In old stellar populations, metallicity is usually the first (the main) parameter controlling the distribution of HB stars, horizontal branch morphology may depend on other parameters, this is the so-called *second parameter problem* to be solved.

- After the central helium is almost consumed, a carbon-oxygen core is formed, surrounded by a helium-burning shell and a hydrogen envelope. The star's luminosity increases and its effective temperature decreases, leading it to enter the **Asymptotic Giant Branch (AGB)**. This is the final evolutionary stage for many stars before reaching the endpoint, the white dwarf cooling sequence. During the Early-AGB stage, the helium-burning shell primarily contributes to energy production. Intermediate and massive stars may experience a significant convective episode known as the *second dredge-up*. After the helium shell is nearly depleted, the Thermal Pulsing-AGB stage begins, with the hydrogen-burning shell becoming the dominant energy source. Some stars may experience the *third dredge-up*, the deepest convection event in their lifetime. On the other hand, stars with insufficient envelope masses may skip the complete or partial AGB phase, e.g. AGB manqué stars (Greggio et al., 1990), PE-AGB stars (Bressan et al., 2012).

- The essence of the evolutionary history of stars is that their existence is a constant

struggle against their own gravitational forces (Kippenhahn et al., 2013). My work is mainly focused on the end products, white dwarfs, which are described in detail in the following section.

1.3 White Dwarfs

White Dwarfs (WDs) are the final evolutionary stage of the vast majority ($\sim$ 98%) of stars in the Universe (Winget et al., 2008). Indeed, all stars with initial mass below 8 $M_{\odot}$, with a possible extension to 11 $M_{\odot}$, are expected to end their evolution as WDs (Córsico et al., 2019; Woosley et al., 2015). Their study can provide a large amount of information about the physical properties and the evolutionary mechanisms of their progenitors. Moreover, WDs are the ideal stellar structures to test physical processes occurring under extreme matter density conditions (Giddings et al., 2008; Isern et al., 2008; Malec et al., 2001).

WDs are commonly envisaged as the naked cores of the progenitor stars that, at the end of their life, have lost the envelope. Their evolution in time is generally described as a pure cooling process, during which WDs evolve towards cooler temperatures and fainter luminosities because essentially they cannot produce energy, either through nuclear reactions, or by gravitational contraction, and radiate away the residual thermal energy of their ions. This produces a tight relation between WD luminosities and their cooling ages, which has been commonly adopted as cosmic chronometer to constrain the age of several populations of our Galaxy, including the disk, globular and open clusters (e.g., Bedin et al. 2010; Hansen et al. 2007; Jeffery et al. 2016; Mukremin Kilic et al. 2017).

The assessment of cooling ages of WDs are strongly dependent on precise measurements of their cooling rates, as well as the corresponding theoretical models. In general, there are two independent methods to test the cooling rates of WDs (Isern et al., 2022): for a single white dwarf star, we can derive the rate of period change when experiencing the variable stage in their instability strip (Benvenuto et al., 2002; Chen et al., 2019; Hermes et al., 2017; Kepler et al., 2021; Su et al., 2021); for white dwarf populations, like in GCs, the White Dwarf Luminosity Functions (WDLFs) can convey tremendous information about the cooling sequences (Moehler et al., 2008), as well as checking many physical speculations (Catalán et al., 2008; Goldsbury et al., 2016; Isern et al., 2018).

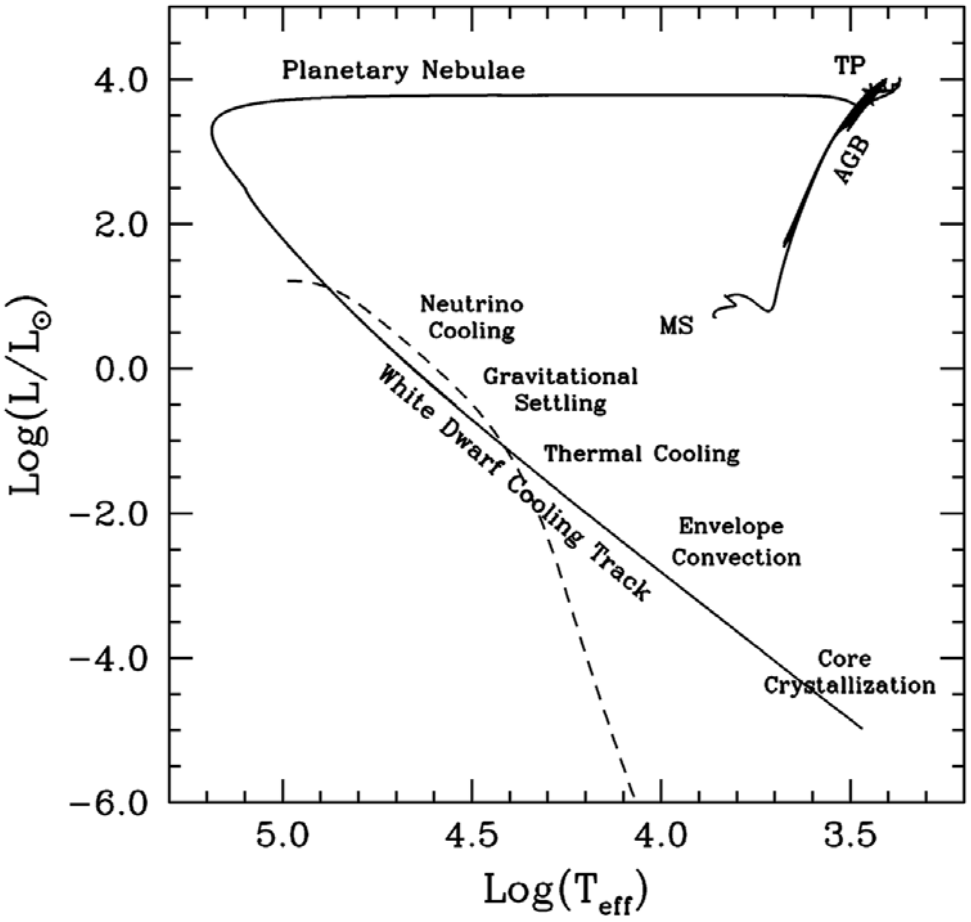

Figure 1.5: Hertzsprung–Russell Diagram (HR-diagram) of the evolutional track of a 1.5 $M_{\odot}$ star, the neutrino luminosity is marked with dashed line (Isern et al., 2022).

1.3.1 Carbon-Oxygen core white dwarfs

WDs are characterized by a relatively simple structure consisting of a degenerate Carbon-Oxygen (CO) core and a partially degenerate Helium envelope ($\sim 10^{-2}$ $M_{\odot}$), more than $\sim$ 80% of WDs are surrounded by a thin Hydrogen-atmosphere (10^{-4} – 10^{-10} $M_{\odot}$ even thinner), which are DA WDs according to the spectral type. Remaining are non-DA WDs, typically DB-type, with only a He-atmosphere. The other remaining small part in non-DA includes DO, DC, DQ, DZ etc. with different spectroscopic properties (Eisenstein et al., 2006).

The vast majority of WDs contain a CO core and the mass distribution shows a narrow peak at 0.59 $M_{\odot}$(Mukremin Kilic et al., 2020), while $M_{WD} > 1.05$ $M_{\odot}$ or more (lower than chandrasekhar limit), massive WDs may have a Oxygen-Neon (ONe) or Oxygen-

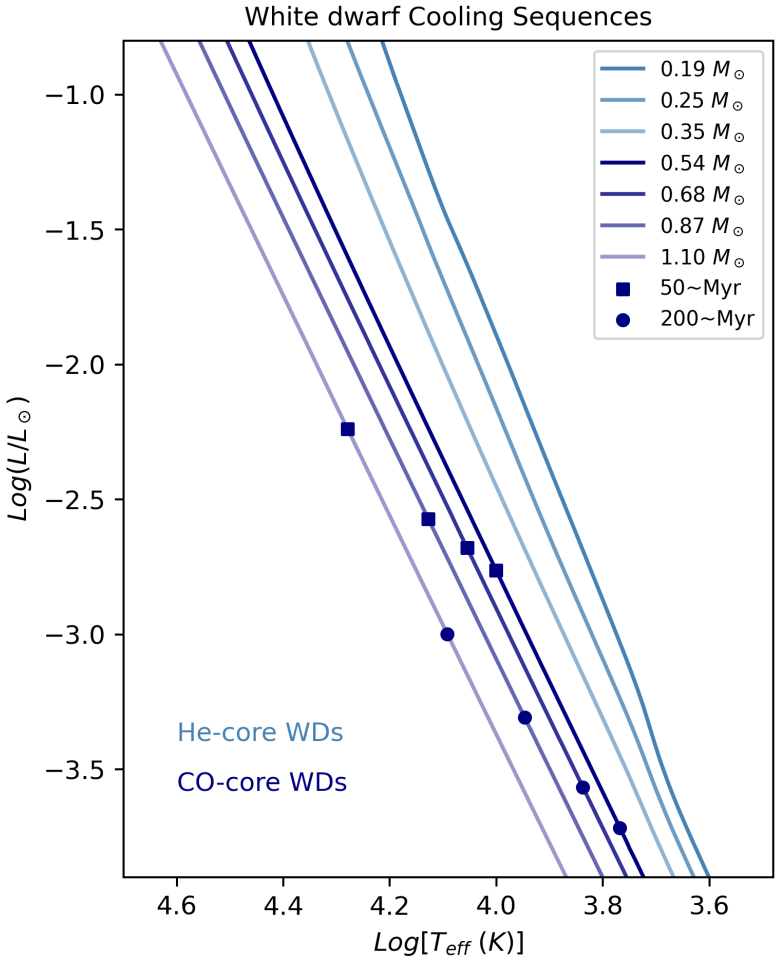

Figure 1.6: HR-diagram of the theoretical white dwarf cooling tracks with different masses (M. Salaris et al., 2013).

Neon-Magnesium (ONeMg) core (Enrique Garcia-Berro et al., 1997). Thus, white dwarf populations in GCs are mainly composed of CO-core WDs.

The evolution of CO-core WDs

Mestel (1952) presented the first predictive model of WD Cooling sequence as:

$$\Delta t \propto (L/M)^{-5/7} \tag{1.1}$$

where Δt is in years, L and M are luminosity and mass, respectively. The zero-order approximation equation of the cooling model is the so-called "*Mestel's law*", which simplifies

the cooling process with the physical parameters as a power-law, so that one can easily find that the cooling rate is related to its mass and luminosity. Although Mestel's law can be used to approximate the cooling process during the median stage, the neutrino emission are even dominates the energy loss in the very hot phase ($-1 \lesssim log(L/L_{\odot})$), which leading to a cooling rate faster than that derived from the Mestel's law. An example of WD Cooling track is given in Figure 1.5, after the very hot neutrino cooling stage is fluid cooling ($-3 \lesssim log(L/L_{\odot}) \lesssim -1$), when reaching the very faint stage of core crystallization ($log(L/L_{\odot}) \lesssim -3$), the additional energy provided by latent heat and gravitational sedimentation causes the cooling slows down with respect to the Mestel's law.The final stage comes when the star as a whole is almost completely solidified, the specific heat follows the Debye's law and the star cools rapidly again even approaching or exceeding than that of the Mestel's law.

WD Luminosity Function

Luminosity Function (LF) defined as the number of stars of a given luminosity per unit luminosity interval. As mentioned in section 1.3, WD LF plays a key role in exploring WD populations, whatever in constraining the age of the host Clusters, or testing the physical mechanism along the cooling sequences, etc. As shown in Figure 1.6, where the dark blue lines represent different CO WD Cooling track with different masses, and the same age location is marked with the same dots. WDs with different masses follow different cooling tracks and different cooling rates, so the cooling rate changes due to the physical process will be presented in the luminosity function. For example, the cooling rate of massive white dwarfs is slower than that of less massive ones, so that at the end of the WDCS, a kind of "hook" appears that can be projected onto the corresponding luminosity function and used to constrain the age of the GC. In a word, WD luminosity function is the powerful tool for exploring in many aspects.

1.3.2 Helium-core white dwarfs

Helium-core white dwarfs are generally the Extremely low-mass white dwarfs (ELM WDs) with masses below $\sim 0.3\ M_{\odot}$, Helium-core WD CSs are redder and brighter than the CO-core WD CSs in Color Magnitude Diagram (CMD) (see Figure 1.6), thus it is easy to distinguish the He-core WDs with respect to the CO-core WDs when the precise observational data are obtained.

Since the timescale required for He-core WDs to evolve from single stars through the nu-

clear reaction is exceeds the current age of the universe (except in some extreme conditions), almost all observed He-core WDs are thought to have formed from binary evolution(Istrate et al., 2016; Mukremin Kilic et al., 2007), and a large number of ELM WDs have been discovered in GCs as companion stars to MSPs (van Kerkwijk et al., 2005), the introduction of binary MSPs is detailed in Section 1.4.

1.4 WDs as the companion stars to MSPs

1.4.1 Millisecond Pulsars

MSPs are rapidly spinning Neutron Stars (NSs) with periods less than 30 ms (Andrew G. Lyne et al., 1998) that are distinguished from the “Normal" pulsars population, which have longer spinning periods. Since the first MSP was discovered in the Globular Cluster (GC) M28 in 1987 (A. G. Lyne et al., 1987), further 236 MSPs have been discovered in 36 Galactic GCs so far[1]. More than half of these MSPs are located in a binary system. Although $\sim$ 600 MSPs have been discovered in the Milky Way[2], more than one-third of them are hosted by GCs, thus suggesting a link between the MSP formation rate and the environment in which are formed.

MSPs are generally considered the outcome of the evolution of Low-Mass X-ray Binaries (LMXBs) with a NS primary (see Bhattacharya et al. (1991), F. R. Ferraro et al. (2015), and Wijnands et al. (1998)). According to this scenario, a slowly rotating NS is spun-up through mass accretion and angular momentum transfer from an evolving companion star. At the end of a $\lesssim$ 1 Gyr long accretion phase, an exhausted and envelope stripped companion star is left, commonly a He-core white dwarf (WD) (John Antoniadis et al., 2016a; M. Cadelano et al., 2015a; Driebe et al., 1998; F. R. Ferraro et al., 2003; Istrate et al., 2014b; Thomas M. Tauris et al., 1999). A special class of binary MSPs in tight orbits with Period $<$ 1 d are called “Spider" MSPs (Roberts, 2013). They are characterized by having non-degenerate companion stars which are usually tidally distorted and heated by the interaction with the pulsar and its relativistic wind (Douglas et al., 2022). The formation of MSPs can be also explained through alternative channels such as the Accretion-Induced Collapse (AIC) of a massive Oxygen-Neon or Oxygen-Neon-Magnesium WD. These systems should be characterized by large orbital periods (Ablimit et al., 2022; Paulo C. C. Freire et al., 2014;

[1]Pulsars in GCs: http://www.naic.edu/~pfreire/GCpsr.html
[2]The ATNF pulsar catalog: https://www.atnf.csiro.au/research/pulsar/psrcat/

Nomoto, 1987; T. M. Tauris et al., 2013, 2017; B. Wang et al., 2022).

In most cases MSPs are expected to form in the LMXB channel. Mass accretion during this phase can in principle produce NSs with masses higher than standard slowly rotating pulsars. Therefore, MSPs studies can provide a tool to determine through observations the NS mass distribution and maximum mass sustainable by a NS, which is the one of the most valuable parameter to constrain the equation of state of ultra-dense matter (see John Antoniadis et al., 2016a; James M. Lattimer, 2012; Özel et al., 2016).

1.4.2 Companion stars

In the case of MSPs with degenerate companions, such as WDs or NSs, precise mass measurements of both the binary components can be directly obtained through the timing analysis if relativistic effects are observed (e.g. periastron precession, Shapiro delay, etc...; see Section 2 in Özel et al., 2016). If they are not, mass measurements can be indirectly performed through the analysis of the WD companions, usually observable through UV and optical observations. In fact, by comparing the UV-optical magnitudes with appropriate binary evolution models, the mass of the companion star can be evaluated and such a value, combined with the orbital properties of the system, can place constraints on the NS mass (e.g. M. Cadelano et al., 2015a, 2019; Dai et al., 2017; Kirichenko et al., 2020). Furthermore, spectroscopic observations can also be used to determine the companion radial velocity curve. This can be combined with the radial velocity curve of the NS to measure the binary mass ratio, thus providing additional constraints on the NS mass (e.g. F. R. Ferraro et al., 2003). In some cases, the spectroscopic data is good enough to allow the determination of the WD mass as well, which combined with the mass ratio allows the determination of the NS mass (J. Antoniadis et al., 2012; John Antoniadis et al., 2013; Mata Sánchez et al., 2020). Spectroscopic studies of WD companions have been also very useful for tests of gravity theories (e.g. John Antoniadis et al., 2013)[3].

1.5 GCs as ideal observational laboratories

With respect to this thesis work, the conglomeration of stars hosted in GCs provide the ideal environment where a large and homogeneous amount of WDs originated by relatively

[3] An updated list of NS masses determined from timing and precise optical measurements can be found at https://www3.mpifr-bonn.mpg.de/staff/pfreire/NS_masses.html

low-metallicty progenitors with respect to the Galactic field can be found. GCs are ideal astrophysical laboratories to explore the White dwarf cooling sequences (WDCSs), since WDs are resulting from the same environment and they appear at the same distance from the observer. The study of the morphology and star distribution (e.g. Luminosity Function (LF)) along the WD cooling sequence can provide crucial information about the WD physics (e.g. cooling time and other processes), and it provides a unique opportunity to conduct a census of the evolved population of massive stars, thus tracing the cluster star formation history.

Moreover, GCs are collisional systems where the high stellar densities and frequent dynamic interactions favor the formation of a large number of exotic objects such as Millisecond pulars (MSPs) (e.g. M. Cadelano et al., 2018; P. C. C. Freire et al., 2017; Ransom et al., 2005; Ridolfi et al., 2022), Blue Straggle Stars (BSSs) (e.g. Mario Cadelano et al., 2022; F. R. Ferraro et al., 1993, 1997, 1999; Francesco R. Ferraro et al., 2004) and cataclysmic variables (e.g. Belloni et al., 2019, 2020; Rivera Sandoval et al., 2018). Therefore, GCs provide the ideal stellar laboratories to study the formation and evolution of exotic systems, as well as the complex interplay between stellar evolution and dynamics (M. Cadelano et al., 2017a; Dalessandro et al., 2013a; F. R. Ferraro et al., 2009, 2012, 2018, 2019; Francesco R. Ferraro et al., 2020; Barbara Lanzoni et al., 2019; Libralato et al., 2022).

1.6 The Ideal Instrument: the Hubble Space Telescope

In this thesis, all the photometric observational data sets are based on the Advanced Camera for Surveys (ACS) or Wide Field Camera 3 (WFC3) mounted on the Hubble Space Telescope (HST) and retrieved from the MAST[4]. Thanks to the deep and high-resolution data captured by the HST, even the faint WDs in the dense GCs could be well resolved.

The HST was launched into near-Earth orbit ($\sim$ 540 kilometers above the Earth) in 1990 and has been in operation for more than 30 years with maintenance support at several times (Four service missions between 1993 and 2009). It is a Cassegrain reflector telescope features a 2.4 m (diameter) primary mirror and a 0.3 m secondary mirror. Because the HST is commanded from the ground, several spacecraft systems are in place to keep it running smoothly, including communications antennas, solar panels, thermal protection, pointing system (the science instrument FGSs is one of them), and computers and automation. The structure and instruments diagram is shown in Figure 1.7.

There are currently six science instruments (WFC3, ACS, STIS, COS, NICMOS, FGSs)

[4]Mikulski Archive for Space Telescopes (MAST): https://archive.stsci.edu/

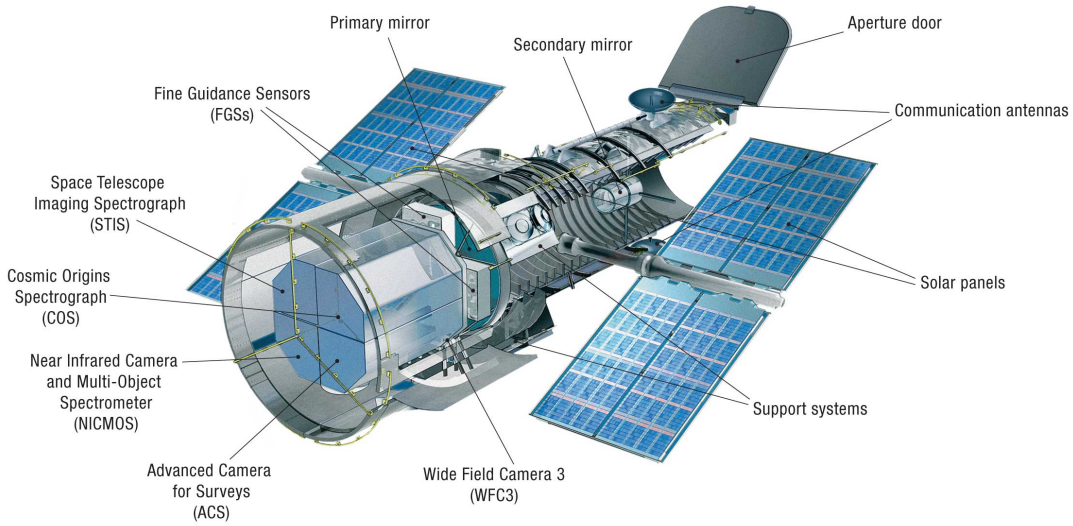

Figure 1.7: Cutaway diagram of the Hubble Space Telescope (HST). Credit: NASA/STScI.

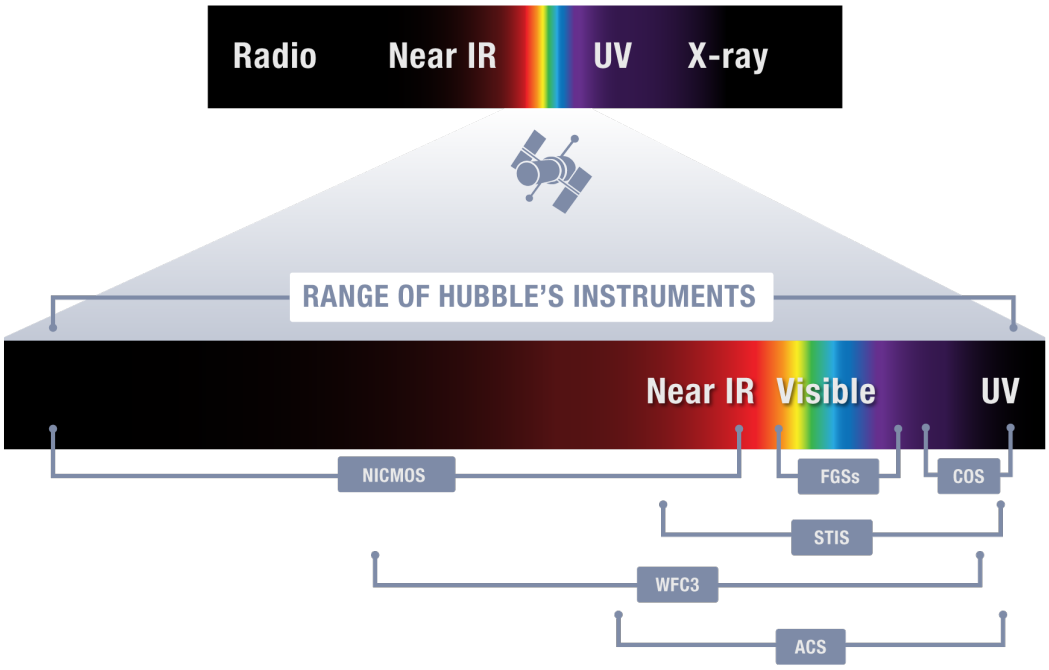

Figure 1.8: The observe wavelengths of Hubble's six scientific instruments. Credit: NASA/STScI.

mounted on the HST, covering from ultraviolet through infrared in the spectrum, the ACS and WFC3 are designed to operate as the imaging camera (ACS also for spectroscopy, HRC is not operational.) that are powerful in exploring faint objects in dense clusters. The STIS, COS, and NICMOS (disabled now) are mainly designed to obtain the spectrum in different wavelengths, while the FGSs are the targeting cameras to keep the HST pointed in the correct direction, as well as the scientific instrument for measuring the positions of stars. The working spectral range of six scientific instruments are shown in Figure 1.8. My work is mainly based on the WFC3 and ACS. Therefore, they are described in the following sections.

1.6.1 Wide Field Camera 3

Instrument

WFC3, as the successor of the Wide Field Planetary Camera 2 (WFPC2), is the fourth generation also the last instrument mounted in the HST (in 2009, during Servicing Mission 4.) for taking image in the visible spectrum, which composed by two channels, Ultraviolet-Visible channels (UVIS) and Infrared channel (IR), covering from the near-Ultraviolet(near-UV, 200 nm) through near-Infrared (near-IR, 1700 nm) band (Gennaro, 2018). Since the WDs are hot objects, all data sets obtained from WFC3 in my work use the UVIS channel.

The UVIS channel covers from 200 nm through 1000 nm with a high resolution of $0.04''/pixel$, which composed of two 4096×2051 back-illuminated CCDs, with a gap of 35 pixel (corresponding to $\sim 1.4''$ on the sky) between chip1 and chip2, the final field of view covers a nominal area of $\sim 2.7' \times 2.7'$. There are 62 wide, medium and narrow-band filters available, in my work mainly used F275W, F336W, and F438W (F-indicates that it is a broad-band filter, 275/336/438-refers to the central wavelength of the filter in nanometers, W-stands for Wide).

Data products

The raw images taken by WFC3 in orbit and their calibrated products could be retrieved from the MAST, there are kinds of products provided in different calibration stage with different suffixes. In general, the "fits" images with the "_flc" suffix are used, which are UVIS standard calibrated images (flat fielding, dark and bias subtraction, etc.) including Charge Transfer Efficiency (CTE) corrected.

The final product (take the example of fits image with suffix "_flc"), or the retrieved single FITS file, including all the images collected from the two chips, as well as the new information from the data processing by CALWFC3 and AstroDrizzle. For instance, a single FITS file has 16 (7 + 9) extensions, the first 7 extensions includes 1 Global Header, and 2 image sets (for chip2 and chip1, respectively.), each image set contains 3 data arrays, the science image [SCI], the error array [ERR], and the data quality array [DQ]. For final products with suffix of "_flt" and "_flc" have an additional 9 extensions with the astrometric information. Therefore, before the photometric data reduction, the first step is to split and extract the science images of chip1 and chip2 from the stacked FITS image.

1.6.2 Advanced Camera for Surveys

Instrument

ACS is the third generation instrument and was installed in the HST during Servicing Mission 3B in 2002 (Dressel, 2022), replacing the original instrument Faint Object Camera (FOC). It has three channels for imaging or spectroscopy, covering from 1150 Å through 11000 Å: Wide Field Channel (WFC) is designed for deep imaging and spectroscopic survey; High Resolution Channel (HRC) is for imaging faint object around bright stars but has been disabled since 2007; Solar Blind Channel (SBC) is designed for imaging and spectroscopy in far-Ultraviolet. My work is based on the images captured by WFC in blue and optical band.

The WFC covers from 350 nm through 1100 nm with a resolution of $0.049''/pixel$, its field of view is $\sim 3.37' \times 3.37'$. Like the UVIS in WFC3, the WFC employs also a mosaic of two 2048×4096 back-illuminated CCDs with a 50 pixel ($\sim 2.49''$ on the sky) gap between chip1 and chip2. The WFC and HRC share filter wheels, which contain filters of two different sizes for optical and ultraviolet wavelengths, the full-sized filters can be used with both channels, while the small-sized filters cover only $72'' \times 72''$ for WFC. The filter wheels are composed of two sets on one axle, so when a desired filter is selected in one filter wheel, the other one will automatically rotate to the CLEAR 1L/2L aperture. The full-sized filters (F435W, F625W, F606W, F814W) were used in my work.

Data products

The raw data obtained from the ACS/WFC are used in the similar calibration pipeline with WFC3/UVIS, the final structure of the data products is the same as described in section 1.6.1,

the structure of data products see Figure 1.9.

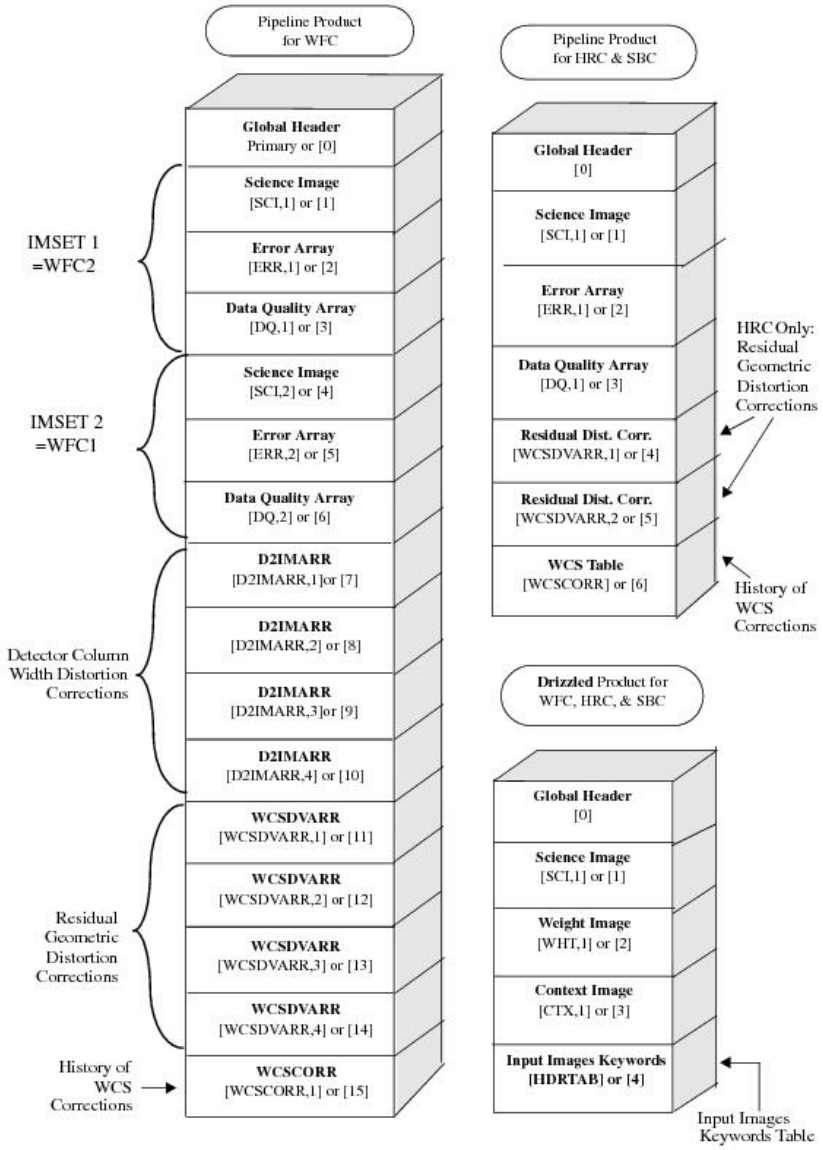

Figure 1.9: ACS File structure after Calibrated and Drizzled. Credit: NASA/STScI.

Chapter 2

Slowly cooling white dwarfs in M13 from stable hydrogen burning

Mainly based on Chen et al. 2020, Nature Astronomy, Volume 5, p.1170-1177

2.1 Introduction

White Dwarfs (WDs) are the electron-degenerate core remnants of low-mass stars that have concluded their thermonuclear activity: all stars below 8 $M_{\odot}$, with a possible extension up to 11 $M_{\odot}$, are expected to end their evolution as WDs (Córsico et al., 2019; Woosley et al., 2015). Their study provides a large amount of information on the physical properties and the evolution of their progenitors, which constitute $\sim$ 98% of all the stars in the Universe. They are thought to be characterized by the absence of thermonuclear activity and, in fact, in the vast majority of theoretical models (Bédard et al., 2020; M. Salaris et al., 2010) stable nuclear burning in the residual hydrogen-rich envelope (with mass thickness in the range $10^{-4} - 10^{-7}\ M_{WD}$) is assumed to be negligible (L. G. Althaus et al., 2005; Bradley, 1998) and their evolution, in essentially all the astrophysical textbooks, is described as a pure cooling process. Because of this relatively simple structure and evolution, the faint-end of the WD cooling sequence has been proposed as accurate cosmic chronometer to constrain the age of several Galactic populations, including the disk, globular and open clusters. For this reason, a notable observational effort with the Hubble Space Telescope (HST) has been devoted to

the exploration of the WD cooling sequence in Galactic stellar systems (Bedin et al., 2010, 2019; Bellini et al., 2013; Campos et al., 2016; Richer et al., 2008, 2013) , especially in Globular Clusters (GCs) that are the oldest and richest ones. This is because, in spite of their relatively large distances (typically $\sim$ 10 kpc), GCs provide large and homogeneous samples of WDs from coeval progenitors, all located at the same distance from the observer (Moehler et al., 2008).

However, recent computations (Leandro G. Althaus et al., 2015; Miller Bertolami et al., 2013; Renedo et al., 2010) demonstrate that even a relatively small amount of residual hydrogen (a few 10^{-4} $M_{\odot}$) left by the previous evolutionary stages is sufficient to allow quiescent thermonuclear burning. For low-mass (< 0.6 $M_{\odot}$) and low-metallicity (Z<0.001) WDs this can provide a non-negligible source of energy (larger than 40%) in the brightest portion of the cooling sequence, which then rapidly becomes negligible at a luminosity L, in units of solar luminosity $L_{\odot}$, corresponding to $log(L/L_{\odot}) \approx -4$ (or at $log(T_e) \approx 3.7$, where T_e is the star effective temperature in kelvin; see Extended Data Figure 2.6). This (usually neglected) energy source slows down the cooling process, with a consequent observable impact on the WD Luminosity Function (LF), since an increased cooling time naturally translates into a larger number of WDs. The delay in cooling time cumulates during the H-burning phase and reaches a value as large as $\sim$ 760 Myr, which then remains constant and affects the reading of the cooling time at fixed luminosity along the entire cooling sequence (see Extended Data Figure 2.6). Models (Leandro G. Althaus et al., 2015; Miller Bertolami et al., 2013; Renedo et al., 2010) show that the phenomenon is particularly relevant in the low metallicity regime (Z<0.001). Hence it should poorly affect the high-metallicity WDs orbiting the Galactic disk, while it is expected to become observable in the typical metallicity regime of old GCs populating the Galactic halo.

2.2 Results

With the aim of constraining the physics of hot WDs and their cooling processes, here we present the detailed comparison between the brightest portion of the WD cooling sequence in two twin old and massive GCs: M3 and M13. These systems represent a classical "Horizontal Branch (HB) morphology pair" (Francesco R. Ferraro et al., 1997, 1998), because they share many physical properties (see Extended Data Table 2.1), as the metallicity ($[Fe/H] \approx -1.6$) and the age ($t \approx 13$ Gyr) (Denissenkov et al., 2017; Dotter et al., 2010; M. Salaris et al., 2002; VandenBerg et al., 2013), but, at the same time, they display quite different HB morphologies:

a very pronounced blue tail is present in the Color Magnitude Diagram (CMD) of M13, while it is absent in M3. The origin of such a difference is not completely understood yet, although various hypotheses have been suggested (Catelan, 2009; Dalessandro et al., 2013b). For the present study, we used a set of ultra-deep HST observations of these two clusters, acquired in the near-ultraviolet with the UVIS channel of the Wide Field Camera 3 (WFC3)(see Section 'Data-set and Analysis' in Methods). The resulting $(m_{F275W}, m_{F275W} - m_{F336W})$ CMDs of M3 and M13 are shown in Figure 2.1. Their superb quality provides a full view of the stellar populations of the two systems down to $m_{F275W} = 25$, allowing a clear definition of all the evolutionary sequences. As expected in old stellar populations, the bluest portion of the HB dominates in the F275W band, blue stragglers are comparable in magnitude to Red Giant Branch (RGB) stars, and bright WDs reach approximately the same luminosity of Main Sequence Turn-Off Stars (MS-TO) (see Section 'M3 and M13: differences and similarities' in Methods). Indeed, a quite well defined WD cooling sequence, extending by 5 magnitudes in the F275W filter, is clearly visible in the blue side of both CMDs. To make the comparison between the WD cooling sequences of the two clusters as straightforward as possible, we shifted the CMD of M3 to match that of M13. We found that only a shift in magnitude ($\Delta m_{F275W} = -0.55 \pm 0.02$) is required (see Section 'M3 and M13: differences and similarities' in Methods), providing an impressive match of all the evolutionary sequences and further confirming that the two systems have approximately (within a few 0.1 Gyr) the same age. At this point the two CMDs are fully homogeneous and we can focus on the properties of the WD cooling sequences: the two CMDs (after alignment) zoomed on the WD region are shown in Figure 2.2. In the following analysis, we conservatively selected the WD samples down to a magnitude limit $m_{F275W} \leq 23.5$, where the completeness level is larger than 50% at any distance from the center in both clusters (see Section 'Artificial star experiments and completeness' in Methods and Extended Data Figure 2.7), and we excluded the stars located at more than 3 σ from the mean ridge line of the cooling sequence (σ being the photometric error at each magnitude level). The comparison with theoretical WD cooling sequences (M. Salaris et al., 2010) suggests that the adopted magnitude cut corresponds to a luminosity $log(L/L_{\odot}) \approx -1.7$, which limits the following analysis to the first $\approx$ 100 Myr of cooling (see Figure 2.2).

The adopted selection criteria provide 418 and 284 WDs in M13 and M3, respectively. Their LFs, both before and after correction for incompleteness, and computed in bins of 0.5 magnitudes are shown in Figure 2.3a. It can be seen that the conservative assumptions adopted for the sample selection strongly limit the impact of incompleteness: the global

correction to the adopted samples is smaller than of 15%, with completeness-corrected populations counting 467 and 326 WDs in M13 and M3, respectively. Hence, the completeness correction does not significantly alter the ratio between the number of WDs in the two clusters, with M13 showing a population that is approximately 1.4 times larger than that of M3. Furthermore, also the luminosity distribution along the cooling sequences appears to be different. To quantify this, we built the normalized m_{F275W} cumulative distributions of the two samples (Figure 2.3b) and performed a Kolmogorov-Smirnov test. We found that the probability that the two WD samples are extracted from the same parent population is 9×10^{-3}, indicating that the discrepancy is indeed significant and worth to be investigated in detail.

To take into account the different intrinsic richness of the two clusters, we normalized the observed samples of WDs to the RGB population (see Section 'Normalizing the WD samples' in Methods and Extended Data Figure 2.8), finding that the global population ratios are $N_{WD}/N_{RGB} = 467/1176 = 0.40 \pm 0.02$ in M13 and $N_{WD}/N_{RGB} = 326/1235 = 0.26 \pm 0.02$ in M3. This corresponds to a factor $\sim$ 1.5 more WDs per RGB star (or unit mass) in the former. Further insights can be obtained from the WD LFs normalized to the RGB reference populations (namely, the number of WD counted in each magnitude bin, divided by the total number of RGB stars in the same cluster), which is shown in Figure 2.4. This comparison clearly confirms the result above.

To understand the origin of this difference we first need to assess whether it is due to an excess of WDs in M13, or a deficit of WDs in M3. We thus compared the observations to theoretical expectations. The selected portion of the cooling sequence is made of WDs formed at most $\sim$ 80 Myr ago (see Figure 2.2), while the selected portion of the RGB population samples a time interval (Pietrinferni et al., 2006) of $\sim$ 320 Myr (see Section "Normalizing the WD samples" in Methods). Given that the ratio between the number of WDs and RGB stars is proportional to the ratio of the corresponding lifetimes, we should find $N_{WD}/N_{RGB} = t_{WD}/t_{RGB} = 80/320 = 0.25$, largely independent of the WD mass and the details of the WD structure (see Section 'WD lifetime ratio' in Methods). The number ratio in M3 ($N_{WD}/N_{RGB} = 0.26 \pm 0.02$) is fully consistent with the theoretical expectation (Pietrinferni et al., 2006; M. Salaris et al., 2010), whilst the value measured in M13 is significantly larger, $N_{WD}/N_{RGB} = 0.40 \pm 0.02$. The comparison of the normalized differential LFs and the corresponding theoretical expectation based on the evolutionary time ratio of WDs (M. Salaris et al., 2010) and RGB stars (Pietrinferni et al., 2006) (black dashed line in Figure 2.4) further confirms that the discrepancy pertains to the faintest portion

of surveyed cooling sequence of M13. We can thus conclude that the detected difference between the two clusters is due to a significant excess of WDs in M13 (see also Section 'Excess of WDs or lack of RGBs?' in Methods).

2.3 Discussion

As first step, we can safely exclude that the detected WD excess in M13 arises from the long-term internal dynamical evolution of the cluster (as suggested (Richer et al., 2008), instead, in the case of NGC 6397), because the sampled cooling time (80 Myr) is much smaller than the cluster central relaxation time ($t_{rc} \approx 320$ Myr; see Section 'The different BSS and HB content in M3 and M13' in Methods and Table 2.1).

An increase in the number of WDs could be due to a slower cooling process, or an additional channel of WD formation. The mechanism needs to be active just in M13 and could therefore be related to other well-known differences between these two "twin" systems. Indeed, the observed difference in the WD populations could be linked to the different morphologies of the HB. In fact, because of their small envelope mass, the bluest HB stars are expected to completely or partially skip the subsequent Asymptotic Giant Branch (AGB) phase, with a significant impact on the size of the residual hydrogen-envelope in the forming WD and its cooling time (Leandro G. Althaus et al., 2015).

The adopted BaSTI theoretical models (Pietrinferni et al., 2006) show that, at metallicity Z=0.001, HB stars with masses smaller than $\sim 0.56\ M_{\odot}$ do not experience the thermal pulse-AGB stage, where helium and hydrogen are alternatively burned in two separate shells surrounding the Carbon-Oxygen (CO) core, and during which the third dredge-up can occur. This is the deepest convective event occurring in a star's life. It takes place when the (more external) hydrogen-burning shell is temporarily turned off and the surface convection penetrates in the stellar interior extending down to the inter-shell region, which was previously mixed by inner convection during a temporary ignition of the He-burning shell (a thermal pulse). During the third dredge-up, a significant amount of carbon is carried into the convective envelope and, in turn, a significant amount of hydrogen is brought down inside the star, and there it is burned. Thus, the occurrence (or not) of the third dredge-up affects the residual mass of hydrogen with which the proto-WD reaches its cooling track, consequently impacting the WD structure and cooling time. More specifically, appropriate theoretical models (Leandro G. Althaus et al., 2015) found that the proto-WD stars skipping the third dredge-up have hydrogen envelopes thick enough to guarantee stable hydrogen-

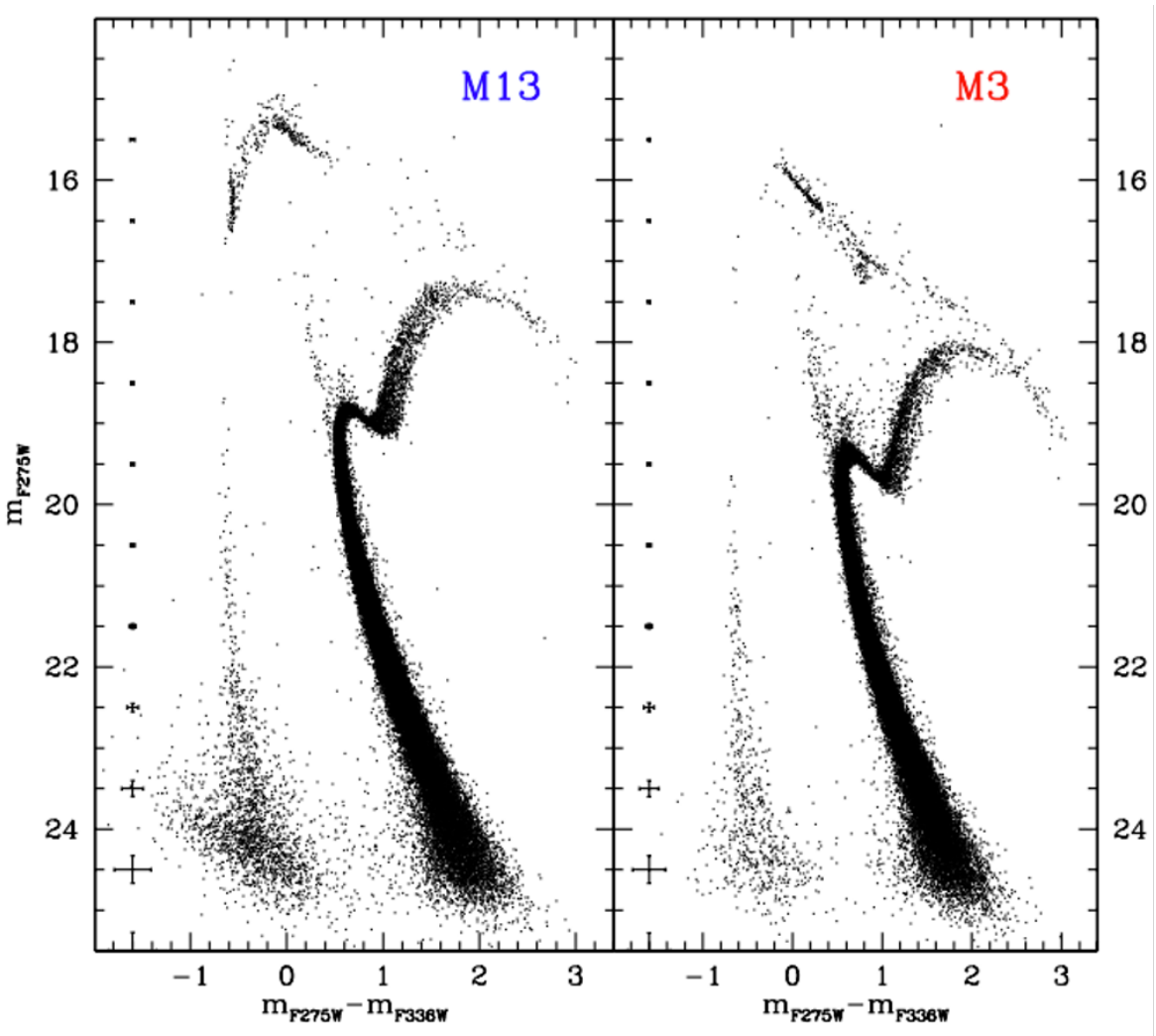

Figure 2.1: The color-magnitude diagrams of M13 and M3. Observed ($m_{F275W}, m_{F275W} - m_{F336W}$) CMDs of M13 (left-hand panel) and M3 (right-hand panel). The mean photometric errors (1 s.e.m.) in bins of 1 magnitude are also reported on the right side of each panel.

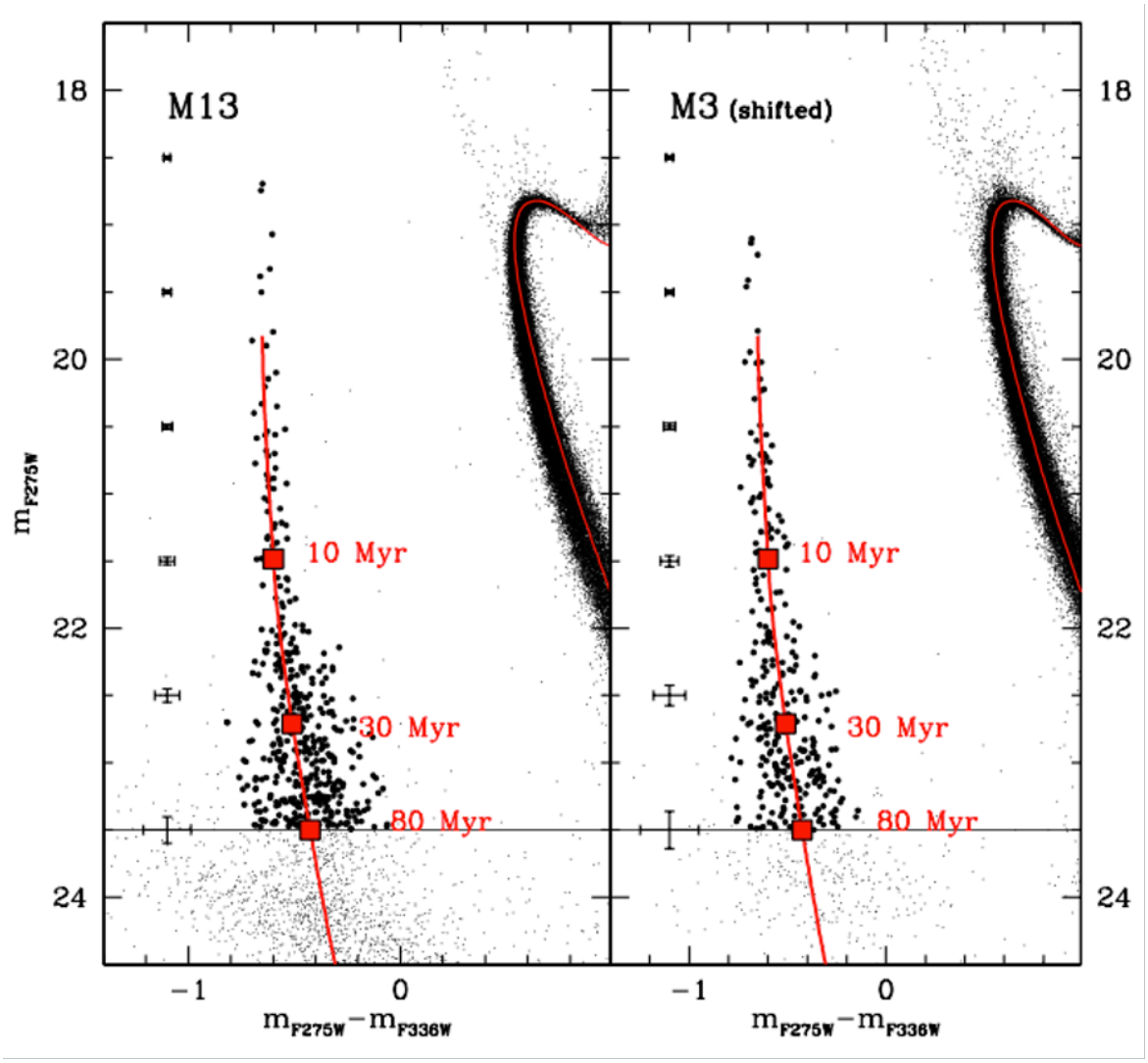

Figure 2.2: The WDs cooling sequences in M3 and M13. WD cooling sequences in the CMDs of M13 (left) and M3 (right, after the alignment). The WDs selected for the present analysis are marked with large black dots. The red lines are theoretical models reported onto the observational diagram by assuming the distance modulus and the reddening of M13 (F. R. Ferraro et al., 1999), $(m-M)_0$ = 14.43 and $E(B-V)$ = 0.02. As apparent, the MS and MS-TO region of both clusters are well reproduced by a 12.5 Gyr old and $\alpha-enhanced$ isochrone from the BaSTI dataset (Pietrinferni et al., 2006), with metal and helium mass fractions Z = 0.001 and Y = 0.246, respectively, corresponding to a global metallicity [M/H]= -1.27 and an iron abundance [Fe/H]= -1.62. Both the WD cooling sequences are well matched by the cooling track (M. Salaris et al., 2010) of a 0.54 $M_{\odot}$ CO-WD with hydrogen atmosphere, transformed (Bellini et al., 2013) to the WFC3 filters. The mean errors (1 s.e.m.) are also marked.

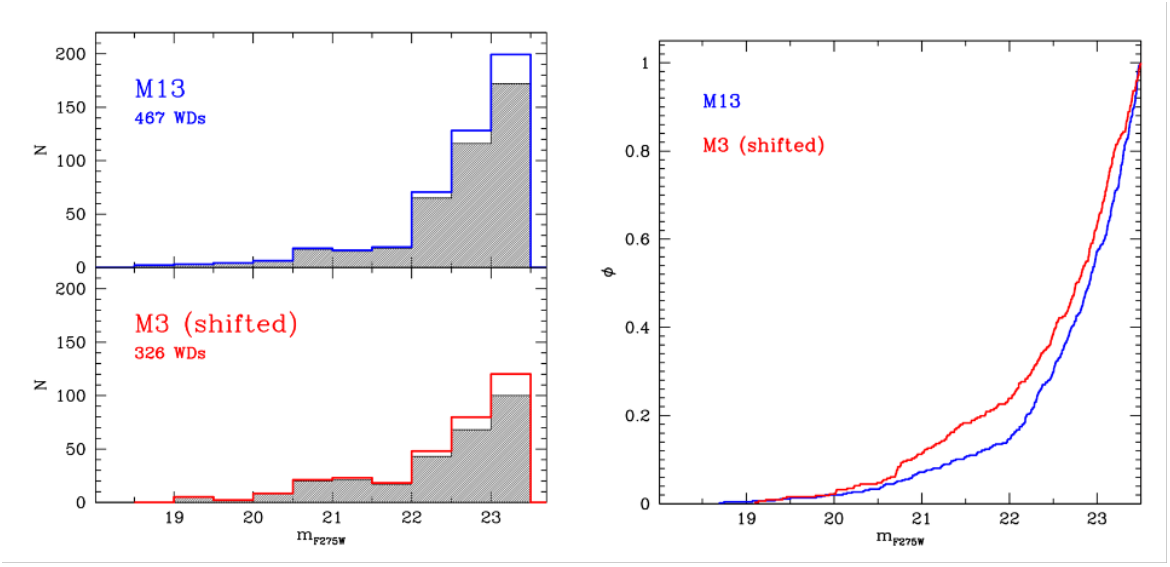

Figure 2.3: Comparing the WD LFs of M3 and M13. a, Observed and completeness-corrected differential luminosity functions (grey shaded histograms and colored lines, respectively) of the WDs selected in the two clusters. b, Cumulative luminosity functions obtained from the completeness-corrected WD samples in M3 (red line) and M13 (blue line), normalized to the total number of WDs in the respective cluster.

burning during the WD cooling evolution, with a resultant extra-energy production that increases the cooling time. At the metallicity of M3 and M13, the minimum thickness needed (Renedo et al., 2010) to sustain hydrogen-burning is $\sim 1.7 \times 10^{-4}\ M_{\odot}$ and the cooling time is increased by $\sim 75\%$ at the minimum WD luminosity sampled in our study ($log(L/L_{\odot}) \approx -1.7$; see Extended Data Figure 2.9).

These arguments support the fact that, along with "standard WDs" well described by models (Bédard et al., 2020; M. Salaris et al., 2010) with no hydrogen-burning, also "slow WDs" may exist, generated by progenitors that do not experience the third dredge-up during the thermal pulses. Due to their longer cooling times, these slow WDs could explain the observed pile-up along the WD LF in M13. The HB morphology of this cluster and its AGB-HB population ratio (see Section 'AGB manqué stars in M13' in Methods and Extended Data Figure 2.10) seem to suggest that a fraction of its stars does indeed skip this evolutionary stage and could therefore give origin to slow WDs. In fact, not only some AGB manqué star (i.e., stars missing the AGB phase completely) is observed in the CMD (see Section 'AGB manqué stars in M13' in Methods), but also other objects are expected to leave the AGB before the onset of thermal pulses.

Overall, theoretical models predict that all the stars with HB mass smaller than 0.56 $M_{\odot}$

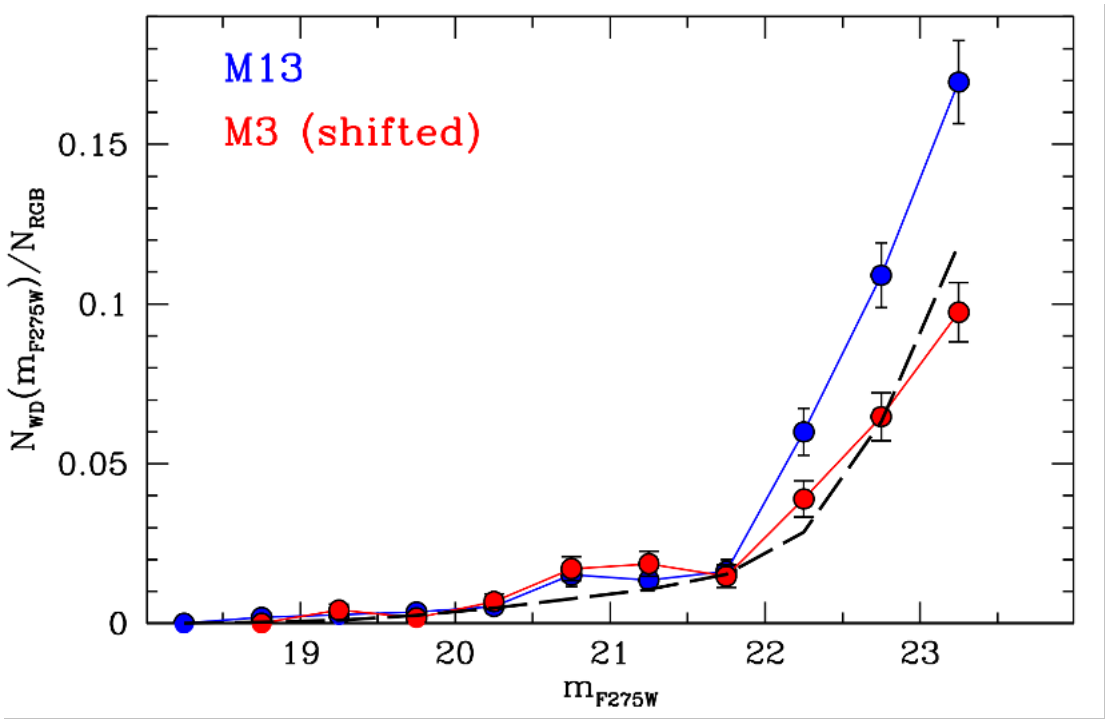

Figure 2.4: The Normalized WD LFs in M3 and M13. WD differential LFs normalized to the total number of RGB stars selected in the two clusters (see Extended Data Figure 2.3): red circles for M3 and blue circles for M13. The mean errors (1 s.e.m.) are also reported. The black dashed line corresponds to the theoretical ratio between the standard WD and RGB evolutionary times (Pietrinferni et al., 2006; M. Salaris et al., 2010) as a function of the WD magnitude.

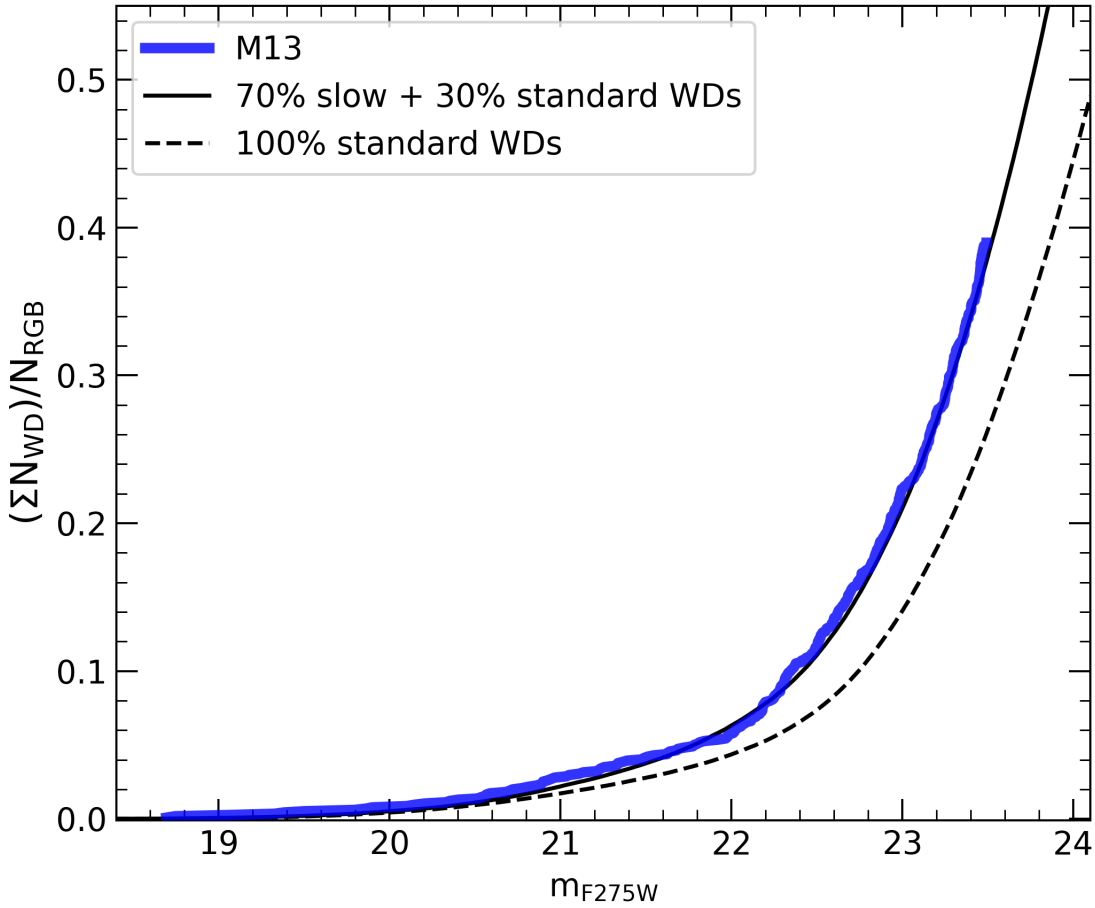

Figure 2.5: Comparison with theoretical cooling models including slow WDs. Comparison between the cumulative, completeness-corrected, WD luminosity function of M13 normalized to the number of RGB stars (blue line), and the theoretical predictions obtained by assuming WD evolution (Leandro G. Althaus et al., 2015) with no hydrogen-burning (100% standard WDs; dashed line), and a combination of 70% (slow) WDs with active hydrogen-burning and 30% (standard) WDs with no hydrogen-burning (solid line).

(this limit depending on the metallicity) do not experience the thermal pulses (hence the third dredge-up) and can thus generate slow WDs. To estimate the fraction of HB stars with mass below this threshold in M13 and M3 we adopted the HB mass distributions determined in previous studies (Dalessandro et al., 2013b) that not only match the observed number distribution of HB stars in magnitude and color, but also reproduce, within 1%, the observed N_{AGB}/N_{HB} ratio of both clusters. We found that only a very small percentage (well below 10%) of HB stars has masses below 0.56 $M_{\odot}$ in M3, thus suggesting that the WD population in this cluster descends from objects that experienced the third dredge-up. The fraction, instead, increases up to 65% in M13.

Putting all these arguments together, we should expect that in M13 (and possibly in any cluster with extended blue HB), two populations of WDs exist:

(1) standard WDs, whose progenitors experienced thermal pulses and third dredge-up, reaching the cooling sequence with a hydrogen envelope not massive enough to ignite stable burning;

(2) slow WDs, originated by stars with HB mass smaller than $\sim 0.56 M_{\odot}$ that skipped the third dredge-up and maintained a residual hydrogen envelope thick enough to allow burning during the subsequent WD evolution, significantly increasing their cooling times.

Could this double WD formation channel be at the origin of the bright WD excess detected in M13? To quantitatively test this scenario we have performed Monte Carlo simulations of the entire RGB-HB-WD evolutionary path appropriate for M3 and M13 (see Section 'Monte Carlo simulation' in Methods), randomly extracting a large set (one million) of age values from a uniform distribution between zero (the base of the adopted RGB selection box; see Extended Data Figure 2.8) and the maximum WD age at the bottom of the considered cooling sequence ($m_{F275W} = 23.5$), and determining the position of the corresponding synthetic stars along the full (RGB-HB-WD) evolutionary sequence.

For the WDs in M3 we used only cooling models (Leandro G. Althaus et al., 2015) with no hydrogen burning, and we found $N_{HB}/N_{RGB} = 0.29$ and $N_{WD}/N_{RGB} = 0.25$, in very good agreement with the observed values (0.28 ± 0.02 and 0.26 ± 0.02, respectively). This fully confirms that essentially all the WD progenitors in M3 experienced the third dredge-up. In M13 we imposed that 35% of the synthetic HB stars generate standard WDs and 65% give origin to slow WDs, described, respectively, by cooling models with non-active and active hydrogen burning. Given the longer cooling times of the WDs from the "slow channel", we find that they contribute to 70% of the total WD population in the relevant magnitude range. From these simulations we obtained $N_{HB}/N_{RGB} = 0.34$, in satisfactory agreement with the

observed value (0.31 ± 0.02), and $N_{WD}/N_{RGB} = 0.37$ that now compares well with the observed ratio (0.40 ± 0.02). Moreover, the observed cumulative LF in M13 is impressively well matched by the simulations including a majority of slow WDs, while it turns out to be completely inconsistent with the curve obtained by assuming 100% of standard WDs (see Figure 2.5).

2.4 Conclusions and future perspectives

Our results suggest that residual hydrogen-burning on the WD surface is the physical phenomenon responsible for the bright WD excess observed in M13. The fact that this phenomenon occurs in M13 and not in M3 is well consistent with the different HB morphology of the two clusters. Actually, at odds with M3, the HB of M13 shows a long extension to the blue that is populated by lower mass stars; these are destined to skip the third dredge-up occurring along the AGB, during which most of the hydrogen remaining in the stellar envelope is consumed. Thus, a significant fraction of the stars in M13 are expected to end their evolution as WDs characterized by a hydrogen envelope massive enough to allow thermonuclear burning that, in turn, slows down the cooling process and consequently affects the observed LF. At the moment, this appears to be the most viable and natural explanation, while alternative scenarios should invoke ad hoc and unknown mechanisms able to increase the production or slow down the cooling process of the WDs in M13, and not in M3. The discovery reported in this paper represents the first direct evidence for the occurrence of stable nuclear burning in the residual hydrogen envelope of cooling WDs and offers an empirical measure of the delay in the flow of time marked by the WD clock in the presence of slowly cooling WDs. Even considering the relatively small portion of the cooling sequence studied here, the effect turns out to be notable: the cooling age at $m_{F275W} = 23.5$, (corresponding to $log(L/L_{\odot}) \approx -1.7$) as read from canonical WD models is 80 Myr and increases to 140 Myr ($\Delta t = 60$ Myr, corresponding to an increment of 75%) when WD models with active hydrogen-burning are adopted.

Systematic and quantitative studies (even of the bright portion, only) of the WD cooling sequence in star clusters with different HB morphologies and different metallicities are now urged to firmly establish and empirically characterize the connection between the HB morphology and the WD excess, and its dependence on the metal content of the system. This will provide the needed observational constraints to advanced models of WD evolution, and it will allow a correct use of WDs as cosmic chronometers, removing systematic uncertainties

that can be as large as 1 Gyr.

2.5 Methods

2.5.1 Data-set and Analysis

For this study we have used a set of ultra-deep, high-resolution images acquired with the UVIS channel of the Wide Field Camera 3 (WFC3) on board the Hubble Space Telescope (HST). The data-set in each cluster is composed of 6 images (each one with exposure time of 415 s in M3, and 427 s in M13) in the F275W filter, and 4 images (each one 350 s long in both clusters) in the F336W.

The photometric analysis was performed via the Point Spread Function (PSF) fitting method, by using DAOPHOT IV (Stetson, 1987) and following the "UV-route" approach used in previous works (Mario Cadelano et al., 2020; Dalessandro et al., 2018a,b; F. R. Ferraro et al., 1997; Francesco R. Ferraro et al., 2001a, 2003a; S. Raso et al., 2017). Briefly, the photometric analysis was carried out on the "_flc" images (which are the UVIS calibrated exposures, including Charge Transfer Efficiency (CTE) correction) and it consists in first searching for the stellar sources in the near-UV images, then force-fit the source detection at longer wavelengths at the same positions of the UV-selected stars. Because the crowding effect generated by giant and turn-off stars (which are increasingly brighter at increasing wavelengths) is strongly mitigated in the near-UV images of old stellar populations (as Galactic globular clusters), this procedure allows the optimal recovering of blue and faint objects, like WDs. So, at first, we selected 200-300 bright and unsaturated stars, relatively uniformly distributed in the sampled field of view, to determine the PSF function of each F275W exposure. The resulting model was then applied to all the sources detected above 5 σ from the background, and the stars found at least in half of the UV images were combined to create a master list. The photometric fit was then forced in all the other frames at the positions corresponding to the master list stars, by using DAOPHOT/ALLFRAME (Stetson, 1994). Finally, the magnitudes estimated for each star in different images of the same filter were homogenized, and their weighted mean and standard deviation have been adopted as the star magnitude and its related photometric error. The instrumental magnitudes were calibrated to the VEGAMAG system and the instrumental coordinates have been put onto the International Celestial Reference System by cross-correlation with the catalogue obtained from the HST UV Globular Cluster Survey (Piotto et al., 2015). The analysis of the sharpness

quality parameter of the PSF fitting procedure shows no significant evidence of non-stellar sources in the WD sample under analysis ($m_{F275W} < 23.5$).

2.5.2 M3 and M13 differences and similarities

The CMDs shown in Figure 2.1 clearly illustrates the well-known similarities and differences between the two clusters. First of all, the different HB morphology, with a lack of stars redder than $(m_{F275W} - m_{F336W}) = 0.5$ and a blue tail extension becoming apparent at colors bluer than $(m_{F275W} - m_{F336W}) = 0$ in M13. A copious population of RR Lyrae (observed at random phases) is, instead, clearly visible in the CMD of M3, as a sort of stream of stars at $m_{F275W} > 16.5$ and $(m_{F275W} - m_{F336W}) > 0.8$. Also, the different BSS content is well apparent, with a significantly larger population in M3 compared to M13 (F. R. Ferraro et al., 2012, 2018; Francesco R. Ferraro et al., 1997; B. Lanzoni et al., 2016).

Apart from these differences, the overall morphology of the CMDs appears to be very similar. To make the comparison more direct, we shifted the CMD of M3 to match that of M13. Indeed the two clusters share many physical properties (see Extended Data Figure 2.6) and, in particular, they have approximately the same metallicity ($[Fe/H] \approx -1.6$) and age ($t \approx 13$ Gyr) (Denissenkov et al., 2017; Dotter et al., 2010; M. Salaris et al., 2002; VandenBerg et al., 2013). Hence, the MS-TO and the sub-giant branch appear to be optimal reference sequences in the UV-CMD to determine the shifts in magnitude and color needed to make the two CMDs coincident. We found that only a shift in magnitude ($\Delta m_{F275W} = -0.55 \pm 0.02$) is required to superpose the CMD of M3 onto that of M13, providing an impressive match of all evolutionary sequences.

2.5.3 Artificial star experiments and completeness

For a quantitative study of the WD populations in terms of star counts, it is necessary to take into account the completeness of the photometric catalogues. We thus evaluated the completeness level of the stars observed along the WD cooling sequences in M3 and M13, at different magnitudes and different distances from the cluster centers, by performing artificial stars experiments. To this end, we followed the standard prescriptions (Bellazzini et al., 2002; M. Cadelano et al., 2020; Dalessandro et al., 2015) that we briefly summarize here. For each cluster, we created a list of artificial stars with a F275W (input) magnitude extracted from a LF modelled to reproduce the observed one. Then, each of these stars was assigned a F336W magnitude obtained by interpolating along the mean ridge line of the WD cooling

sequence in the $(m_{F275W}, m_{F275W} - m_{F336W})$ CMD. The artificial stars thus generated were then added to the real images by using the DAOPHOT/ADDSTAR software, and the entire photometric analysis was repeated following exactly the same steps described in Section 'Data-set and Analysis' above. To avoid artificial crowding, the added stars were placed into the frames in a regular grid of 23×23 pixels (corresponding to about fifteen times the FWHM of the stellar sources), each cell containing only one artificial star during each run. The procedure was iterated several times and more than 150,000 artificial stars have been overall simulated in the entire field of view sampled by each cluster.

The ratio between the number of artificial stars recovered at the end of the photometric analysis (N_o) and the number of stars that were actually simulated (N_i) defines the completeness parameter $C = N_o/N_i$. As well known, the value of C strongly depends on both crowding and stellar luminosity, becoming increasingly smaller in cluster regions of larger density and at fainter magnitudes. We thus divided the sample of simulated stars in bins of cluster-centric distances (stepped by 5″) and F275W magnitudes (from $\sim$ 18 to $\sim$ 25, in steps of 0.5 mags) and, for each cell of this grid, we counted the number of input and recovered stars, calculating the corresponding value of C. The sizes of the radial and magnitude bins were chosen to secure enough statistics while keeping as high as possible both the spatial resolution and the sensitivity of the completeness curve to changes in the stellar luminosity. The uncertainties assigned to each completeness value (σ_C) were then computed by propagating the Poisson errors, and typically are on the order of 0.05. The construction of such a completeness grid allowed us to assign the appropriate C value to each observed WD with given F275W and F336W magnitudes, located at any distance from the cluster center (see Extended Data Figure 2.7). As expected, C progressively decreases toward the cluster center and for fainter and fainter magnitudes. However, the completeness level remains relatively high down to very faint magnitudes, being larger than 50% for $m_{F275W} \approx 24$ and $m_{F275W} \approx 24.2$ in M3 and M13, respectively.

2.5.4 Normalizing the WD samples

To take into account the intrinsic richness of the two clusters, we used as normalization the number of stars counted in a post-main sequence stage, which is directly observable, independent of parameters like distance and reddening, expected to be the same in systems of equal total mass, age and metallicity, and only dependent on stellar evolutionary times (Renzini et al., 1986). In particular, because of their large luminosities (corresponding to large completeness levels at any distance from the center), we adopted as reference the RGB

population. Taking advantage of the excellent alignment obtained between the CMDs of the two clusters, we used the same selection box, sampling the entire RGB extension nearly down to base of the RGB (located at $m_{F275W} \approx 18.9$) up to the tip (see Extended Data Figure 2.8). We counted 1176 RGB stars in M13 and 1235 in M3. According to the BaSTI evolutionary track25 of a 0.8 $M_{\odot}$ star with appropriate metallicity, the time needed to evolve across the selected portion of the RGB is $\sim$ 320 Myr.

2.5.5 WD lifetime ratio

The derived lifetime (Pietrinferni et al., 2006; M. Salaris et al., 2010) ratio between the cluster WDs down to the considered limiting magnitude ($m_{F275W} \approx 23.5$) and the selected RGB stars is equal to $t_{WD}/t_{RGB} = 0.25$, independent of the adopted WD mass for values between 0.50 and 0.60 $M_{\odot}$, which are appropriate for the present study. The same ratio, and in general the same cooling times at each point across the relevant magnitude range, are found when we employ independent calculations by other authors (Bédard et al., 2020), both their models with hydrogen mass fraction equal to 10^{-4} times the total WD mass (like in the adopted computations (Leandro G. Althaus et al., 2015)), and those with much thinner hydrogen layers ($10^{-10} \times M_{WD}$).

2.5.6 Excess of WDs or lack of RGBs?

In principle, the large N_{WD}/N_{RGB} ratio measured in M13 does not necessarily imply an excess of WDs in this cluster: it could also be explained by a severe lack of RGB stars. Indeed, because of some mass-loss enhancement during this phase, a fraction of RGB stars in M13 could evolve directly to the helium-core WD stage before the helium flash: after all, the bluest objects along the cluster HB have masses only slightly larger than the helium-core mass at helium ignition, as discussed below. However, the study (Sandquist et al., 2010) of the luminosity function of RGB stars in M13 discloses no convincing evidence that a sizeable fraction of stars leaves the RGB before undergoing the helium flash. We can thus safely conclude that M13 hosts a genuinely larger population of WDs with respect to M3.

2.5.7 The different BSS and HB content in M3 and M13

It has been noted in many previous papers (F. R. Ferraro et al., 1997, 2012, 2018; B. Lanzoni et al., 2016), that these two clusters host quite different populations of blue stragglers. This

is apparent also in the CMDs presented in Figure 2.1, where we count 153 BSSs in M3 and only 62 in M13, if we adopt the same prescriptions and selection box used in previous works (F. R. Ferraro et al., 2018). In addition, the BSS radial distribution, which can be used as "dynamical clock" (F. R. Ferraro et al., 2012, 2018; B. Lanzoni et al., 2016), is different in the two systems, testifying that M3 is more dynamically evolved than M13, also in agreement with the values of the central relaxation time derived from the cluster structural parameters (Harris, 1996)(see Table 2.1). The relaxation times of both systems are larger than the age of the oldest WDs here considered, denoting that the observed difference cannot be due to internal dynamical processes. In general, it is seemingly hard to associate the different blue straggler properties and the different cluster dynamical stages to the observed excess of bright WDs in M13.

We then investigated the role that the well-known difference in the HB morphology might play. As it is apparent in Figure 2.1, the HB of M13 has a long extension to the blue (hot temperatures), at odds with that of M3, and many studies in the literature have tried to explain this difference. A detailed comparison (Catelan, 2009) between the two clusters, concluded that, independent of the adopted mass-loss recipe, the HB morphology cannot be reproduced in terms of an age difference (Denissenkov et al., 2017; Dotter et al., 2010; M. Salaris et al., 2002; VandenBerg et al., 2013), which (if any) must be very small. Hence, at least one additional parameter should be invoked to account for the blue HB extension observed in M13, and subpopulations of helium-enhanced stars are in principle a viable solution. In fact, for any given cluster age, MS-TO and RGB stars belonging to a helium-enhanced subpopulation have masses lower than their helium-normal counterparts, thus producing bluer HB stars (for fixed RGB mass-loss) with thinner envelopes around the helium cores. A recent detailed analysis (Dalessandro et al., 2013b) estimated that, to account for the observed HB morphologies, the HB stars in M3 had to have a spread $\Delta Y \approx 0.02$ in their initial helium mass fraction, whilst in the case of M13 $\Delta Y \approx 0.05$. A larger Y spread among the HB stars of M13 was estimated also in other similar analysis (Denissenkov et al., 2017). Other authors (Milone et al., 2018) instead, found that the maximum internal helium variation between the reddest and bluest HB stars in each of the two clusters is essentially the same, implying a difference of just 0.01 in the helium mass fraction of the two systems. Although these results demonstrate that the origin of the discrepancy it still not clear, as a matter of fact the HB morphology is strikingly different in the two clusters.

2.5.8 AGB manqué stars in M13

Interestingly, the extreme blue group in the HB blue-tail of M13 defines a sort of vertical sequence (here named extreme-HB) that counts $\sim$ 96 stars, corresponding to approximately 25 % of the total HB population of the cluster (see Extended Data Figure 2.10). In addition, seven evolved HB stars are also visible in the CMD at $m_{F275W} < 15.6$, lying exactly on the extension of the extreme-HB sequence and tracing a sort of evolutionary path. According to our adopted BaSTI models25, these objects have masses below $\sim 0.5\ M_{\odot}$. Hence, they likely are AGB-manqué stars (Greggio et al., 1990), i.e., objects that completely skip the AGB phase and directly evolve toward the WD stage, because their envelope is so thin that no helium-burning can be ignited in a shell surrounding the carbon-oxygen core after the HB stage. Indeed, this seems to be consistent with the population ratios measured in the two clusters. We adopted appropriate selection boxes to count the AGB and HB populations in the optical and UV-CMDs, respectively (see Extended Data Figure 2.10). The AGB-HB ratio turns out to be significantly (at 2 σ level) smaller in M13 ($N_{AGB}/N_{HB} = 30/368 = 0.08 \pm 0.01$) than in M3 ($N_{AGB}/N_{HB} = 45/344 = 0.13 \pm 0.02$), in agreement with the hypothesis that a fraction of HB stars in M13 miss the entire AGB phase (and give rise to 'slow WDs'), while this does not happen in M3, where no HB blue-tail is present.

2.5.9 Monte Carlo simulations

To test quantitatively the proposed scenario, we have performed Monte Carlo simulations, using WD cooling models (Leandro G. Althaus et al., 2015) with a thick hydrogen envelope and efficient hydrogen-burning (obtained from the full evolution of progenitors that do not experience the third dredge-up), and their counterpart with hydrogen-burning artificially switched off. The output luminosities have been transformed (Bellini et al., 2013) to the magnitudes of the WFC3 photometric system the same way as done for the standard models (M. Salaris et al., 2010). In the relevant magnitude range, the models (Leandro G. Althaus et al., 2015) with no hydrogen-burning have the same cooling times of the "standard" models (M. Salaris et al., 2010) employed before, despite a hydrogen-envelope a few times thicker.

For the RGB evolution, we have considered BaSTI tracks (Pietrinferni et al., 2006) of appropriate metallicity (Z=0.001), with helium abundance (and evolving mass) in agreement with the distribution derived (Dalessandro et al., 2013b) in each cluster. We emphasize that the evolutionary timescale in the considered RGB portion (see Extended Data Figure 2.8) is essentially insensitive to the precise value of the stellar mass around a value of 0.8 $M_{\odot}$ and

to the initial helium abundance, for values up to $Y \approx 0.30$. The model age has been set to zero at the faint limit of the adopted RGB selection box (see Extended Data Figure 2.8). For the HB and subsequent WD evolution, we treated M3 and M13 separately.

For M3 we considered the evolutionary timescales of a 0.66 $M_{\odot}$ BaSTI HB model (Pietrinferni et al., 2006) for the same Z and initial Y, finding $t_{HB} \approx 92$ Myr (this value is essentially independent of the initial Y in the relevant helium mass fraction range). The adopted mass value corresponds to the mode of the HB mass distribution (Dalessandro et al., 2013b). The total age (RGB plus HB) has then been added to the cooling age of 0.54 $M_{\odot}$ WD models (Leandro G. Althaus et al., 2015) without nuclear burning. The neglected AGB evolution, between the end of the HB phase and the beginning of WD cooling, provides a negligible contribution to the total age of the WD models.

In the case of M13 we have performed the same kind of simulations, employing the same RGB mass, but two different HB masses for the two WD channels. To simulate the progenitors of slow WDs, we have considered a HB model with mass equal to 0.51 $M_{\odot}$, which corresponds to the mode of the distribution (Dalessandro et al., 2013b) of the HB masses below 0.56 $M_{\odot}$. The corresponding HB lifetime is $\sim$ 117 Myr (this value is not affected appreciably by the fact that such a star is predicted to be enhanced in helium by $\Delta Y \approx 0.045$). For the standard WDs, we have instead considered a HB model with mass equal to 0.60 $M_{\odot}$ (the mode of the mass distribution of HB stars more massive than 0.56 $M_{\odot}$), with a lifetime of 93 Myr. Finally, for the evolution of standard WDs we used the same WD models (Leandro G. Althaus et al., 2015), without nuclear burning, employed in M3, whilst for the slow WDs we adopted models with the same mass but with active hydrogen burning. These models have a cooling age of about 140 Myr at the faint magnitude limit considered in our analysis, a factor 1.75 higher than for models without nuclear burning in the envelope. We proceeded as for M3, but separately for the 'standard' and 'slow' WD channels, and then added together the two samples of RGB+HB+WD synthetic stars with the constraint that the number of HB stars from the simulation of the 'slow' WD channel must be equal to 65% of the total number of synthetic HB objects.

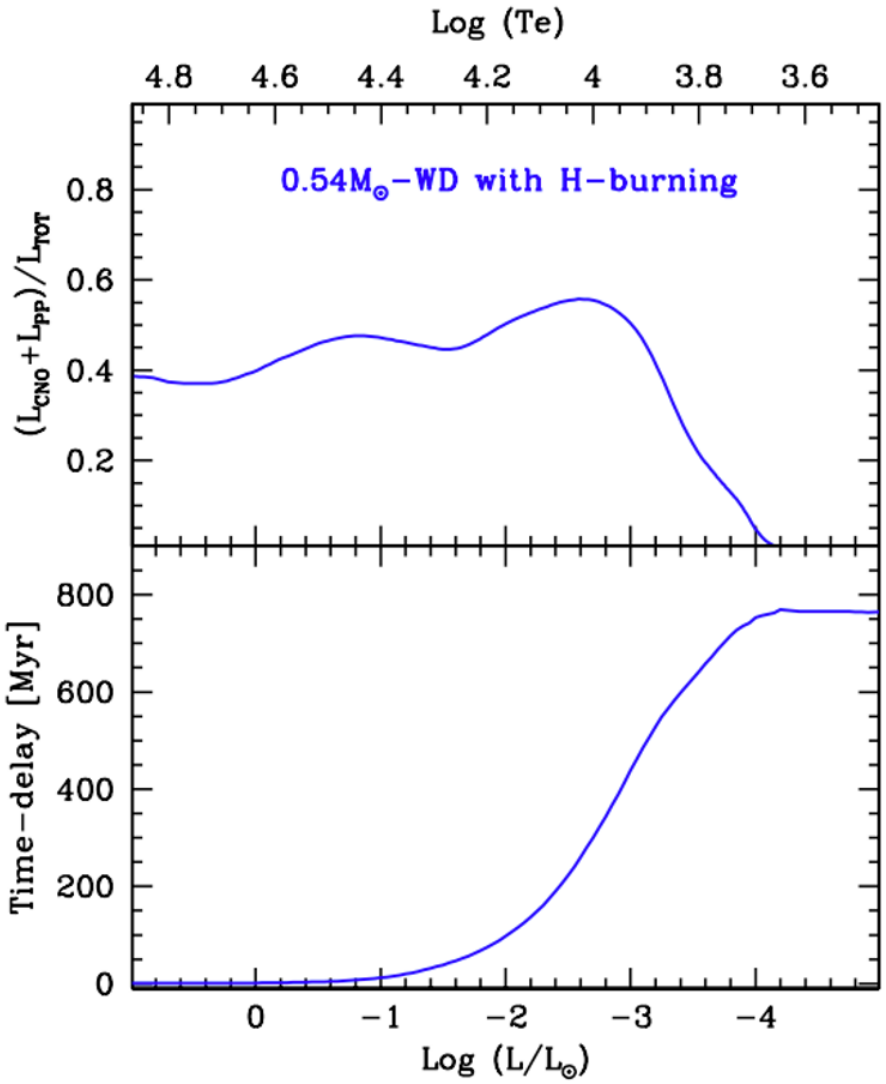

Figure 2.6: The effect of stable H-burning on a low mass WD. a, Contribution of stable H-burning (Leandro G. Althaus et al., 2015; Miller Bertolami et al., 2013) (via PP and CNO chain) to the global luminosity of a low metallicity (Z=0.001), low mass (0.54 $M_{\odot}$) WD as a function of its decreasing luminosity. H-burning provides a significant contribution (larger than 40%) to the WD luminosity in the brightest portion of the cooling sequence, becoming negligible at $log(L/L_{\odot}) \approx -4$ and $log(Te) \approx 3.7$ (see the temperature scale in the top axis). b, Delay (Leandro G. Althaus et al., 2015; Miller Bertolami et al., 2013) in the cooling time induced by stable H-burning, with respect to a model without burning. The time delay keeps increasing during the phase of active H-burning and reaches a value as large as $\sim$ 760 Myr, which then remains constant during the entire subsequent evolution.

Table 2.1: Physical parameters of M3 and M13. From top to bottom, the listed parameters are: metallicity, age, V-band absolute integrated magnitude, logarithm of the central luminosity density (in units of $L_{\odot}pc^{-3}$), logarithm of the central relaxation time (in years).

Parameter	M3(NGC 5272)	M13(NGC 6205)	Reference
[Fe/H]	−1.50	−1.53	Harris (1996)(2010 edition)
Age	12.6	12.9	Denissenkov et al. (2017)
M_V	−8.88	−8.55	Harris (1996)(2010 edition)
$\log(\nu_o)$	3.57	3.55	Harris (1996)(2010 edition)
$\log(t_{rc})$	8.31	8.51	Harris (1996)(2010 edition)

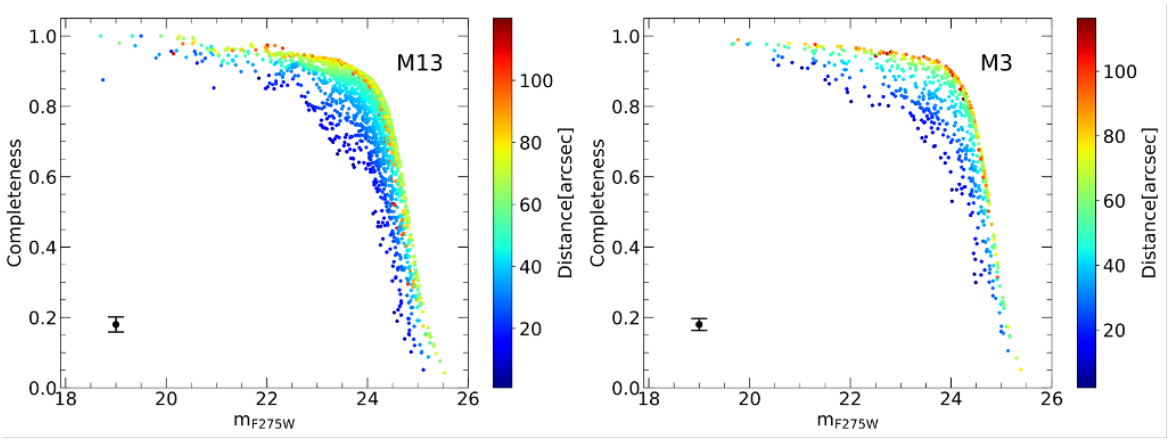

Figure 2.7: The completeness distribution of the WD populations of M13 and M3. Completeness parameter as a function of the F275W magnitude and color-coded in terms of the distance from the cluster center (see color bars) for each WD detected in M13 (left-hand panel) and in M3 (right-hand panel). The mean error (1 s.e.m.) is also reported.

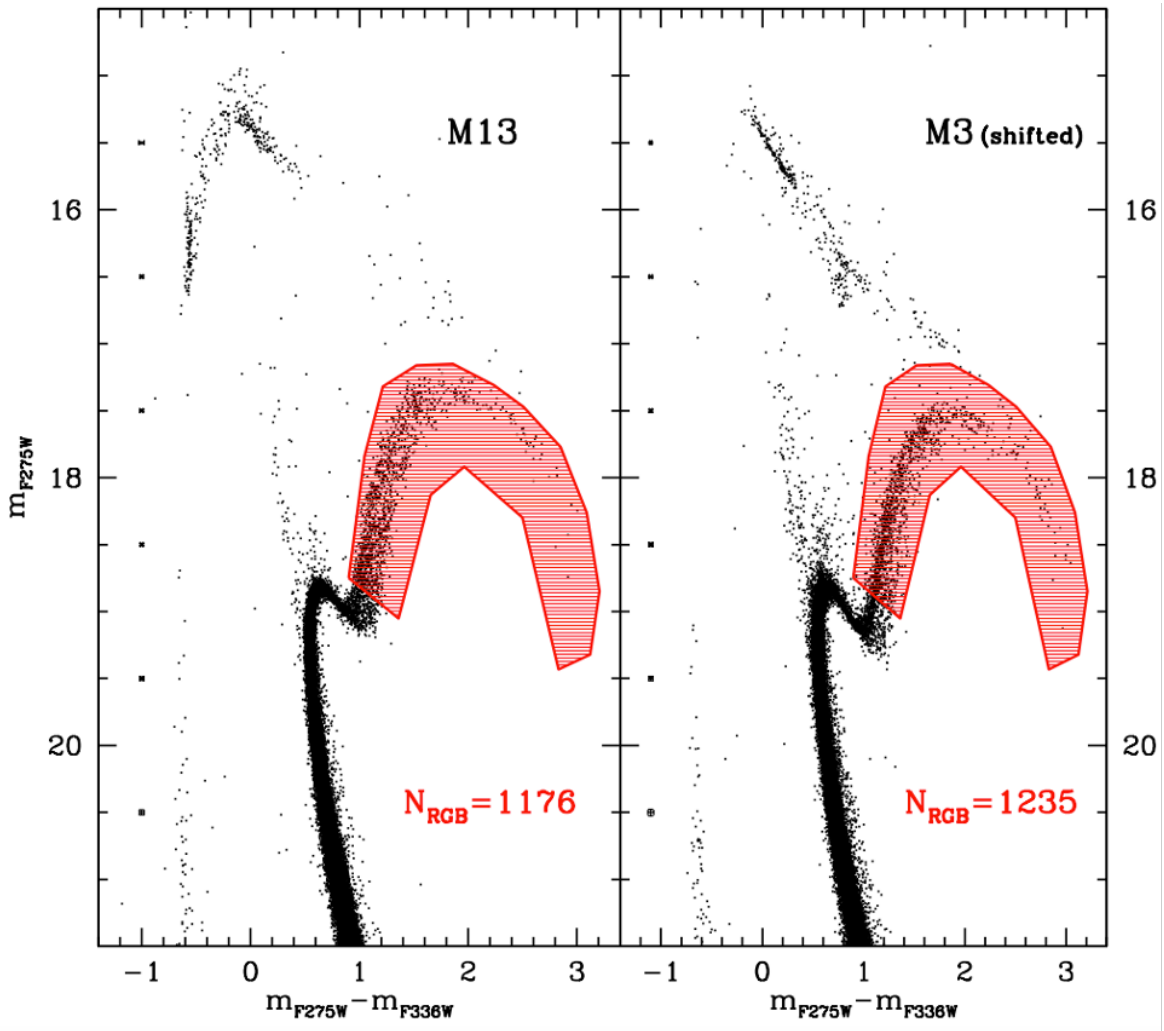

Figure 2.8: The RGB reference population. Selection box (red shaded area) adopted to define the RGB "reference population" in the observed and realigned CMDs of M13 and M3. The number of red giants counted in each cluster is also marked. The mean errors (1 s.e.m.) are also marked.

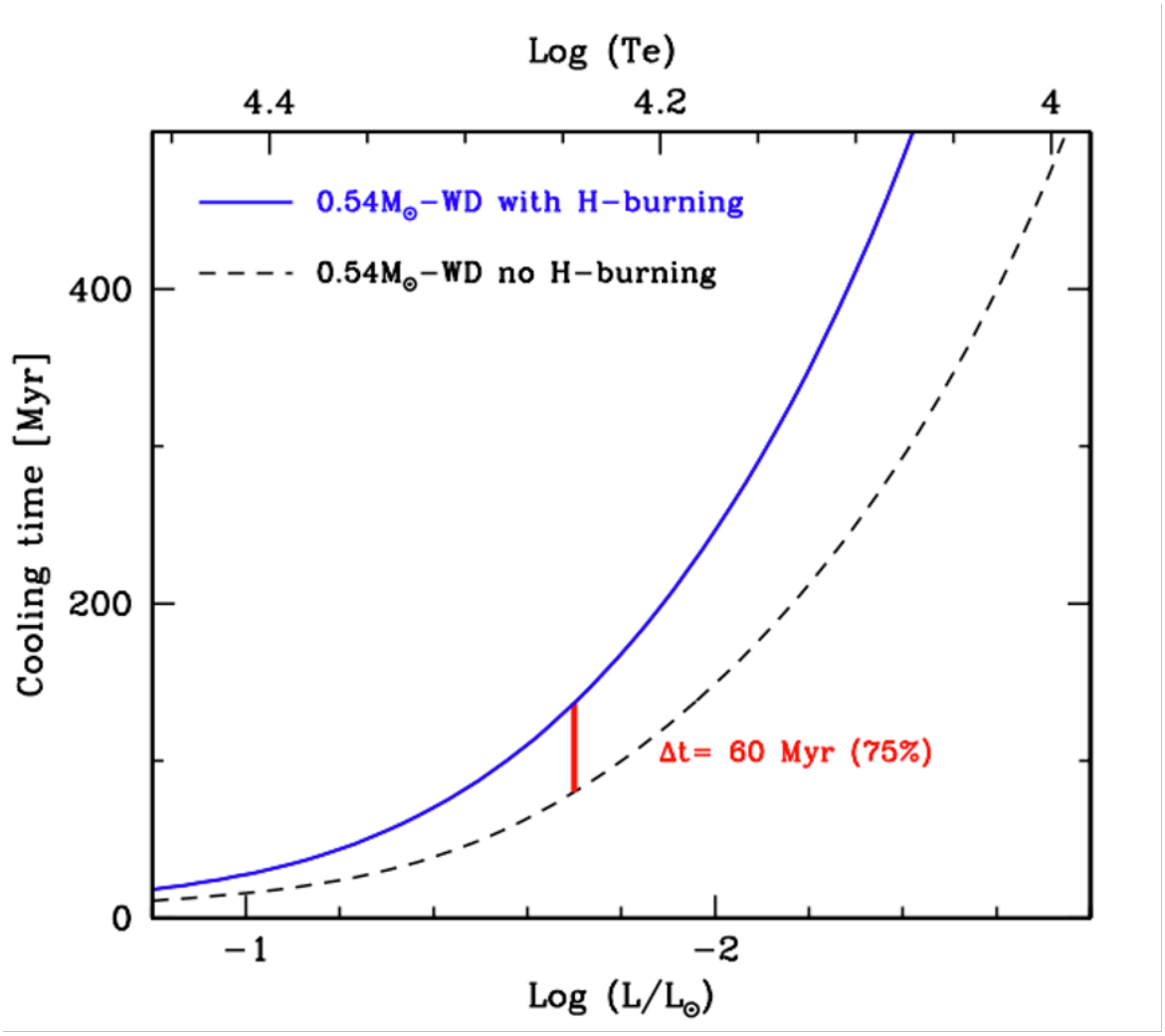

Figure 2.9: WD cooling time for models with and without hydrogen burning. Comparison between the cooling times of a low metallicity, 0.54 $M_{\odot}$ WD with and without hydrogen-burning (Leandro G. Althaus et al., 2015) (solid and dashed lines, respectively). The red segment marks the difference in the cooling time at the luminosity of the faintest WD considered in this study, $log(L/L_{\odot}) = -1.7$ and reports the absolute difference between the two cooling time values (60 Myr), corresponding to a 75% increase if hydrogen-burning is active, with respect to the 'standard' (no-burning) case.

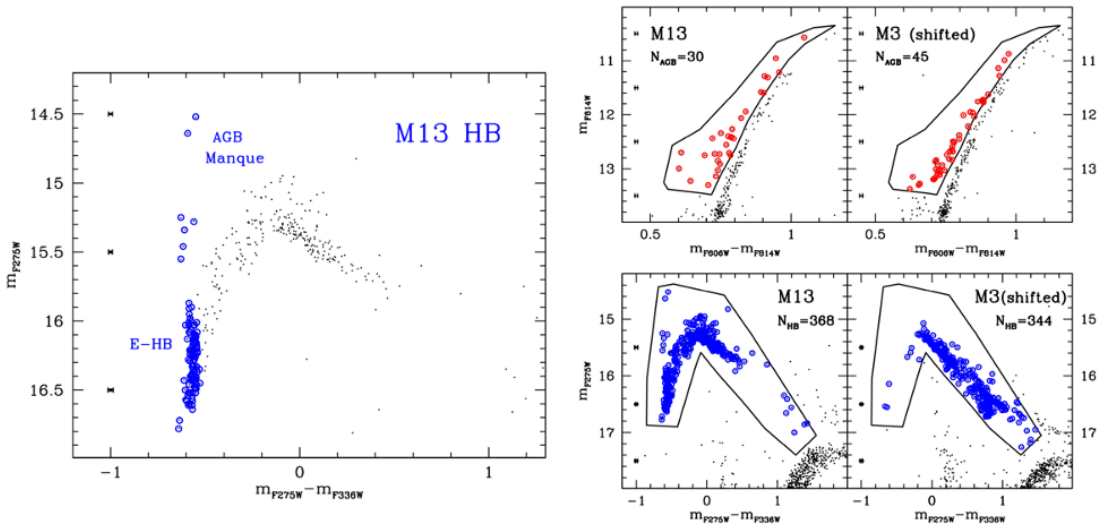

Figure 2.10: HB and AGB populations in M3 and M13. a, UV-CMD of M13 zoomed in the HB region. The extreme-HB (E-HB) and the 7 candidate AGB-manqué stars are highlighted as blue circles. b, AGB and HB selection boxes in the optical- and UV-CMD (top and bottom panels, respectively) for the two clusters. The population star counts are also marked in each panel. The mean photometric errors (1 s.e.m.) are also marked in all panels.

Chapter 3

Slowly Cooling White Dwarfs in NGC 6752

Mainly based on Chen et al. 2022, ApJ, Volume 934, Number 2

3.1 Introduction

Recent models (Leandro G. Althaus et al., 2015) show that even an extraordinary small amount of residual hydrogen (a few $10^{-4} M_{\odot}$) left over from the previous evolutionary stages is sufficient to allow quiescent thermonuclear burning. This can provide a non-negligible source of energy that slows down the cooling rate, especially in the low-mass ($< 0.6 M_{\odot}$) and low-metallicity ($Z < 0.001$) regimes, which are typical of Globular Clusters (GCs) in the Galactic halo. In turn, an increased evolutionary time-scale naturally translates to an increased number of WDs for any fixed luminosity, with a consequent observable impact on the WD Luminosity Function (LF).

The first observational evidence of slowly cooling WDs has been recently provided (Chen et al., 2021, hereafter C21) by the analysis of *Hubble Space Telescope* (HST) ultra-deep photometric data acquired in the near-ultraviolet for M3 (NGC 5272) and M13 (NGC 6205). These two Galactic GCs are considered "twin" systems because they have very similar iron abundance ([Fe/H]$\simeq -1.5$), age ($t \sim 12.5$ Gyr), total mass, and central density (see, e.g., C21). In spite of such a similarity, C21 discovered a clear excess of WDs in the LF of

M13 with respect to M3, and showed that the detected overabundance is very well described by assuming that $\sim$ 70% of the WD population in M13 is composed of slowly cooling objects, while the objects in M3 cool down as expected from standard models. This result is fully consistent also with the different morphology of the horizontal branch (HB) observed in the two systems (e.g., Dalessandro et al., 2013b; F. R. Ferraro et al., 1997): The HB of M13 shows a pronounced extension to the blue, while no blue tail is observed in M3, where the HB is populated in both the red and the blue side of the instability strip, with a sizeable population of RR Lyrae stars. The different morphology is the direct manifestation of different stellar mass distributions along the HB, with the stars populating the blue tail of M13 being less massive than those at the red edge, and those on M3 HB. In turn, the stellar mass during the HB phase is the parameter mainly determining the occurrence (or not) of the so-called 'third dredge-up', a mixing process taking place during the Asymptotic Giant Branch (AGB) phase, which is the evolutionary phase immediately following the HB and preceding the WD stage. This process efficiently mixes the material present in the envelope of AGB stars, bringing most of the hydrogen deeper into the stellar interior, where it is burned. As a consequence, stars experiencing the third dredge-up reach the WD stage with not enough residual hydrogen to have an efficient burning. On the other hand, stars evolving from the blue side of the HB have envelope masses too small to reach the AGB and therefore do not experience the third dredge-up, and they reach the WD stage with a residual hydrogen envelope thick enough to sustain stable thermonuclear burning, thus delaying their aging (Leandro G. Althaus et al., 2015). Most of the stars in M13 (those populating the blue side of the HB) skip the third dredge-up (the so-called post-early AGB and AGB-manqué stars) ending their lives as slowly cooling WDs. On the other hand, according to the observed HB morphology, the HB stars in M3 have large enough masses to reach the AGB and therefore evolve later as standard WDs. The presence of slowly cooling WDs in M13 and the lack thereof in M3 explains the observed numerical excess in the LF of the former.

C21 therefore demonstrated that the presence of slowly cooling WDs can be recognized from the analysis of the WD LF, and it is connected to the HB morphology. Specifically, slowly cooling WDs are expected in clusters with moderate metallicity and blue-tail HB. In this context, here we present the analysis of the bright portion of the WD cooling sequence of NGC 6752, a Galactic GC with metal abundance and HB morphology very similar to those of M13 (see its main parameters in Table 3.1). NGC 6752 and M13 also share a very low value of the R_2 parameter, defined as the ratio between the number of AGB and that of HB stars: $R_2 = N_{\rm AGB}/N_{\rm HB}$ = 0.06-0.07 (Cassisi et al., 2014; Cho et al., 2005; Sandquist et al., 2004).

Table 3.1: Main physical parameters of NGC 6752.

Parameter		References
$E(B-V)$	0.046 ± 0.005	R. G. Gratton et al., 2005
	0.040	Harris, 1996(2010 edition)
$[Fe/H]$	-1.48 ± 0.01	R. G. Gratton et al., 2005
	-1.54	Harris, 1996(2010 edition)
$(m-M)_0$	13.13	F. R. Ferraro et al., 1999
Age (Gyr)	12.5 ± 0.75	Dotter et al., 2010
$\log \nu_0(L_\odot/pc^3)$	5.04	Harris, 1996(2010 edition)
$\log t_{rc}$ (yr)	6.88	Harris, 1996(2010 edition)

This is consistent with the findings of R. G. Gratton et al. (2010), who empirically showed that the R_2 parameter correlates with the HB morphology (clusters with blue extended HB have lower R_2 values), because the stars located in the bluest portion of the HB skip the AGB phase.[1] The simulations of Cassisi et al. (2014) also confirmed that the parameter R_2 of NGC 6752 is well reproduced by standard HB models, and they show that the distribution of stellar masses along the HB in this cluster is essentially the same as in M13 (Dalessandro et al., 2013b).

Because of its similarity with M13 in terms of metallicity ([Fe/H]~ -1.5; R. G. Gratton et al., 2005), age ($t \sim 12.5$ Gyr; e.g., Dotter et al. 2010; M. Salaris et al. 2002; VandenBerg et al. 2013), HB morphology, and HB mass distribution, NGC 6752 thus offers the ideal conditions to further test the presence of a substantial population of slowly cooling WDs in GCs with blue HB morphology. Being closer to Earth than M13, it also allows us to extend the study of this new class of objects to fainter magnitudes.

The paper is organized as follows. Section 3.2 describes the adopted data reduction, calibration and completeness-correction procedures. The analysis of the WD cooling sequence and LF is presented in Section 3.3, which is followed by the discussion of the results and conclusions in Section 3.4.

[1]Note that Simon W. Campbell et al. (2013)(see also S. W. Campbell et al. 2017) claimed that all stars of second generation (i.e., with [Na/Fe]$<$ 0.2; see Raffaele G. Gratton et al. 2012 for a review) skip the AGB. However, this result has been challenged by synthetic HB simulations (Cassisi et al., 2014), and by both spectroscopic (Lapenna et al., 2016; Mucciarelli et al., 2019) and photometric observations (Gruyters et al., 2017) that found evidence of both first and second generation stars along the AGB of NGC 6752.

3.2 Data reduction

The high-resolution photometric data-set of NGC 6752 used in this work has been acquired in the near-ultraviolet (near-UV) with the *HST* under GO-12311 (PI: Piotto) and GO-11729 (PI: Holtzman), using the UVIS channel of the Wide Field Camera 3 (WFC3). It is composed of 12 long exposures (369 s each) in the F275W filter and 3 images in the F336W (2×500 s, and 1×30 s).

The photometric analysis was carried out on the $\_flc$ images (which are the UVIS calibrated frames, also corrected for Charge Transfer Efficiency (CTE)), after applying the Pixel Area Map (PAM) correction. We used DAOPHOT IV (Stetson, 1987) to follow the so-called 'UV-route', which consists in first searching for stellar sources in the near-UV images, then force-fit the source detection at the same positions of the UV-selected stars in longer wavelength images (M. Cadelano et al., 2019; Mario Cadelano et al., 2020; Dalessandro et al., 2018a,b; F. R. Ferraro et al., 1997; Francesco R. Ferraro et al., 2001a, 2003a; S. Raso et al., 2017). This procedure allows the optimal recovering of blue and faint objects, like WDs, because the crowding effect generated by giants and Main Sequence Turn-Off Stars (MS-TO) (which get brighter with increasing wavelengths) is strongly mitigated in near-UV images of old stellar populations (as Galactic GCs).

At first we selected $\sim$ 250 bright and unsaturated stars, relatively uniformly distributed in the sampled field of view, to determine the Point Spread Function (PSF) function of each exposure. The resulting model was then applied to all the sources detected above 5σ from the background, and the stars found at least in half of the UV images were combined to create a *master list*. The photometric fit was then forced in all the other frames at the positions corresponding to the master list stars, by using DAOPHOT/ALLFRAME (Stetson, 1994). Finally, the magnitudes estimated for each star in different images of the same filter were homogenized, and their weighted mean and standard deviation have been adopted as the star's magnitude and its related photometric error. The instrumental magnitudes were calibrated to the VEGAMAG system and the instrumental coordinates, once corrected for geometric distortions (Bellini et al., 2011), have been put onto the International Celestial Reference System by cross-correlation with the catalog obtained from the *HST* UV Globular Cluster Survey (Piotto et al., 2015). A selection in sharpness was applied to remove non-stellar objects (background galaxies) mainly affecting the faintest end of the sample. All stars with sharpness parameter larger than 0.2 have been removed. An accurate additional visual inspection of the images was then necessary to decontaminate the sample from spurious

detections and artifacts in the regions surrounding heavily saturated stars (Annunziatella et al., 2013).

3.2.1 Color-magnitude diagram and comparison with M13

The final ($m_{\rm F275W}, m_{\rm F275W} - m_{\rm F336W}$) CMD of NGC 6752 is shown in Fig. 3.1. It spans approximately 11 magnitudes, providing us with a full view of the cluster stellar population down to nearly $m_{\rm F275W} = 25$, and with a clear definition of all the evolutionary sequences. As expected in the UV-band, the luminosity of RGB stars is substantially decreased with respect to optical wavelengths, while hot HB stars are the brightest objects. Also a sparse population of blue straggler stars is clearly visible (see Sabbi et al. 2004), covering a magnitude range comparable to that spanned by the RGB. Notably, the bright portion of the WD cooling sequence appears well defined and populated, reaching luminosities comparable to those of MS-TO stars, and covering ~ 6 magnitudes in the CMD.

The comparison with Fig. 1 of C21 reveals that the overall morphology of the CMD evolutionary sequences in NGC 6752 is very similar to that observed in M13. Indeed, the MS-TO and the sub-giant branch can be adopted as optimal reference sequences to determine the shifts in magnitude and color needed to superpose one CMD on the other. We found that a magnitude shift $\Delta m_{\rm F275W} = -1.04 \pm 0.02$ and a small color shift $\Delta(m_{\rm F275W} - m_{\rm F336W}) = +0.04 \pm 0.01$ are required to move the CMD of M13 onto that of NGC 6752. The measured differences are compatible with the shorter distance (~ 3 kpc closer, F. R. Ferraro et al. 1999) and the larger reddening ($\delta E(B-V) = 0.02 - 0.03$, see Table 3.1 and Harris 1996) of NGC6752 with respect to M13. Indeed the superposition provides an impressive match of all the evolutionary sequences, including the cooling sequence (see Fig. 3.2). In particular we notice that, although being less populated, the HB of NGC 6752 shares the same morphology observed in M13: HB stars are distributed over the same color range, $-0.6 < (m_{\rm F275W} - m_{\rm F336W}) < 0.4$, with no redder HB stars being detected in both clusters. Also the WD cooling sequences are well superposed, with that in NGC 6752 reaching fainter magnitudes, consistently with its shorter distance from Earth.

3.2.2 Artificial star tests

To perform a quantitative study of the WD population of NGC 6752 in terms of star counts, it is necessary to take into account the photometric completeness of the WD cooling sequence at different magnitudes and different distances from the cluster centre. This is particularly

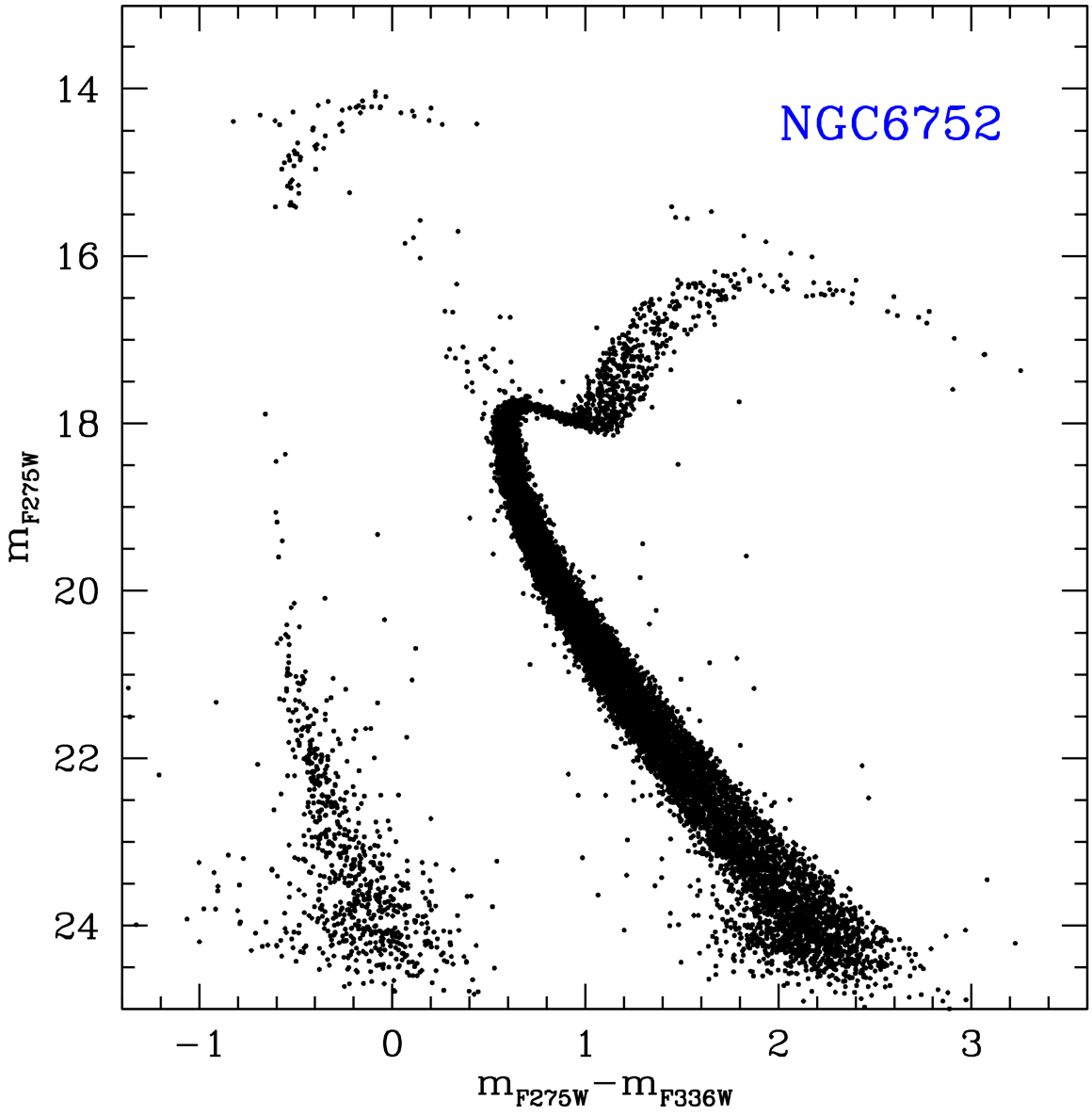

Figure 3.1: Near-UV Color Magnitude Diagram (CMD) of NGC 6752.

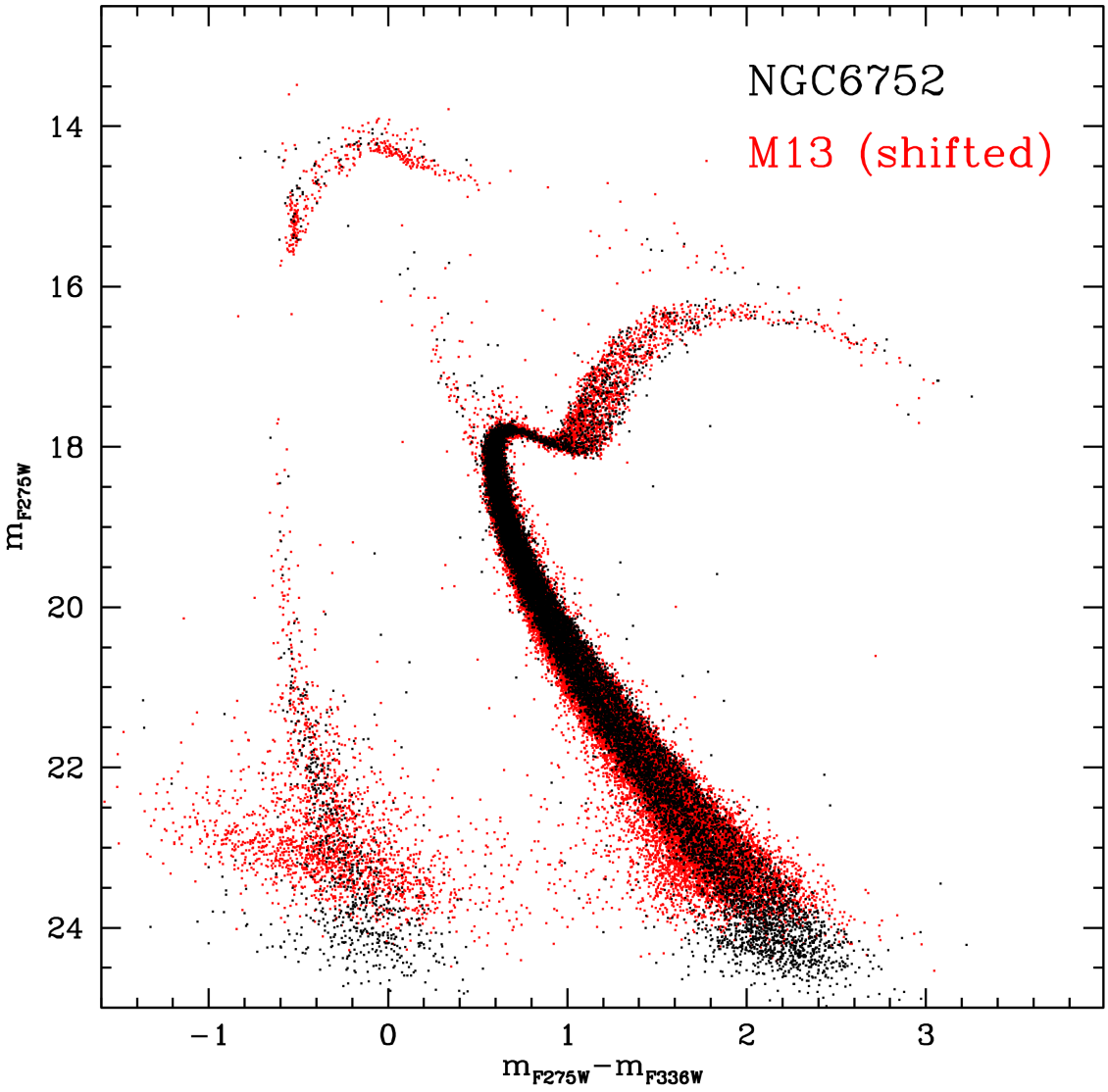

Figure 3.2: Observed (Co-added $m_{\rm F275W}, m_{\rm F275W} - m_{\rm F336W}$ CMDs of NGC 6752 (black dots) and M13 (red dots, from C21). A magnitude shift $\Delta m_{F275W} = -1.04$ and a color shit $\Delta(m_{F275W} - m_{F336W}) = 0.04$ have been applied to the CMD of M13 to match that of NGC 6752.

important in dynamically evolved stellar systems like NGC 6752, which is classified as a post core collapse cluster (Harris, 1996). Indeed, the innermost portion ($r < 10''$) of the stellar density profile shows a clear excess with respect to the King (1966) model that properly fits the external regions (Francesco R. Ferraro et al., 2003a), consistently with its post core collapse classification.[2]

To estimate the photometric completeness, we performed artificial stars experiments following the prescriptions described in detail in Bellazzini et al. (2002)(see also M. Cadelano et al. 2020; Dalessandro et al. 2015), that we summarize quickly here. As first step, we created a list of artificial stars with an input F275W magnitude sampling the observed extension of the WD cooling sequence. Then, each of these stars was assigned a F336W magnitude obtained by interpolating along the mean ridge line of the WD cooling sequence in the $(m_{\rm F275W}, m_{\rm F275W} - m_{\rm F336W})$ CMD. The artificial stars thus generated were then added to the real images by using the DAOPHOT/ADDSTAR software, and the entire photometric analysis was repeated following exactly the same steps described in Section 3.2. To avoid artificial crowding, the added stars were placed into the frames in a regular grid of 23×23 pixels (corresponding to about fifteen times the FWHM of stellar sources), each cell containing only one artificial star during each run. The procedure was iterated several times and, at the end, more than 100,000 artificial stars were simulated in the entire field of view.

The ratio between the number of artificial stars recovered at the end of the photometric analysis (number of output stars, N_o) and the number of stars that were actually simulated (number of input stars, N_i) defines the completeness parameter $\Phi = N_o/N_i$. As it is well known, the value of Φ strongly depends on both crowding (hence, the distance from the cluster center) and stellar luminosity, becoming increasingly smaller in cluster regions of larger density and at fainter magnitudes. We thus split the sample of simulated stars into bins of cluster-centric distances (stepped by $5''$) and F275W magnitudes (from $\sim$ 18, to $\sim$ 25, in steps of 0.5 mag) and, for each cell of this grid, we counted the number of input and recovered stars, calculating the corresponding value of Φ. The sizes of the radial and magnitude bins were chosen to secure enough statistics while keeping as high as possible both the spatial resolution, and the sensitivity of the completeness curve to changes in the stellar luminosity. The uncertainties assigned to each completeness value (σ_Φ) were then computed by propagating the Poissonian errors, and typically are on the order of 0.05. As

[2]The advanced stage of dynamical evolution of this system is further certified by the high radial concentration of its blue straggler stars (see F. R. Ferraro et al. 2018; B. Lanzoni et al. 2016), which is a powerful indicator of dynamical age (the "dynamical clock", see F. R. Ferraro et al. 2012, 2018, 2019; Francesco R. Ferraro et al. 2020).

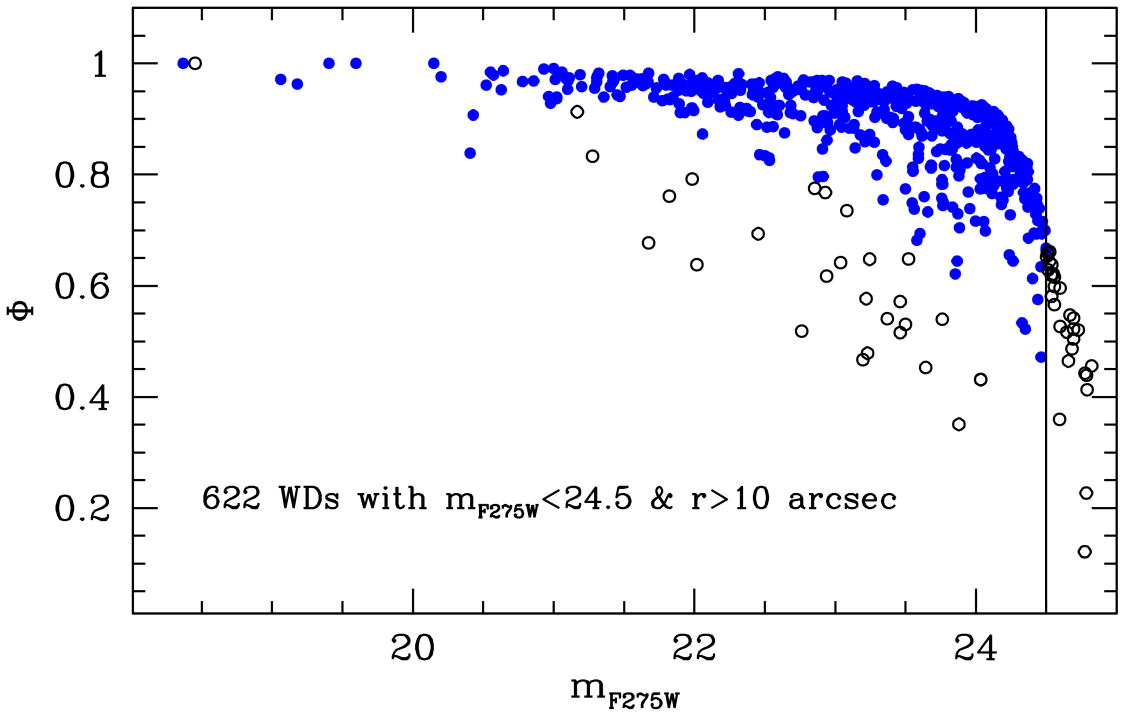

Figure 3.3: Distribution of the WD completeness parameter Φ, as a function of the F275W magnitude. The 622 selected WDs are plotted as blue circles: they all have $\Phi > 0.45$, while those fainter than $m_{\rm F275W} = 24.5$, or located at distances smaller than $10''$ from the cluster center (empty circles) have been excluded from the analysis, to avoid the risk of inappropriate completeness corrections.

coordinates of the center of gravity we adopted the values quoted in Francesco R. Ferraro et al. (2003a): $C_{\rm grav}$ is located at $\alpha_{\rm J2000} = 19^{\rm h}\,10^{\rm m}\,52^{\rm s}.04$, $\delta_{J2000} = -59°59'04''.64$ with a typical 1σ uncertainty of $0''.5$ in both $\alpha_{\rm J2000}$ and δ_{J2000}.The $C_{\rm grav}$ has been computed by averaging the coordinates of all stars detected in the central portion of the cluster (see B. Lanzoni et al. 2007b, 2010; Barbara Lanzoni et al. 2019; Miocchi et al. 2013)

The construction of such a completeness grid allowed us to assign the appropriate Φ value to each observed WD, with a given F275W and F336W magnitude, located at any distance from the cluster center. The behavior of the completeness parameter as a function of magnitude is shown in Fig. 3.3 for all the detected WDs. By excluding the overcrowded innermost region ($r < 10''$) and the faintest end ($m_{\rm F275W} > 24.5$) of the cooling sequence (empty circles in the figure), we obtain a well sampled population of 622 WDs with completeness level larger than 45% (blue circles).

3.3 Analysis and results

3.3.1 Sample selection and WD LF

The impressive match between the CMDs of NGC 6752 and M13 shown in Fig. 3.2) allows us to perform a direct comparison among the properties of the two clusters, even using the same set of isochrones and cooling tracks adopted in C21 for M13. Indeed, Fig. 3.4 shows the cooling track of a $0.54 M_{\odot}$ carbon-oxygen core WD with hydrogen atmosphere (DA-type) from M. Salaris et al. (2010) nicely reproducing the position of the observed WD cooling sequence, and the 12.5 Gyr α-enhanced isochrone with metal abundance $Z = 0.001$ and helium mass fraction $Y = 0.246$ from the BaSTI models (Pietrinferni et al. 2006; see also Hidalgo et al. 2018; Pietrinferni et al. 2006) simultaneously reproducing the MS-TO region of the cluster.

The well-defined cooling sequence in the CMD allowed us to select the WD sample straightforwardly. First, we excluded the objects located more than 3σ away from the mean ridge line of the WD cooling sequence, with σ being the photometric error at the corresponding magnitude level. Then, as discussed above, we conservatively selected stars located at distances larger than $10''$ from the cluster center and at magnitudes $m_{\rm F275W} \leq 24.5$, to keep the completeness level above 45%. The adopted magnitude cut corresponds to a cooling time of $\sim$ 460 Myr, significantly longer than the case of M13, where the analysis was limited to the first 100 Myr of cooling (see C21). Thus, the cooling time sampled by the WD sequence in NGC 6752 is of the order of 0.5 Gyr. Although this is a significant range of cooling times, it corresponds to a negligible variation in terms of WD mass: indeed, the expected difference in mass between a WD that is currently starting the cooling process, and a WD with a cooling age of 0.5 Gyr is $0.001 M_{\odot}$ only.

The adopted selection criteria provide a total of 622 WDs in NGC 6752. The LFs computed in bins of 0.5 magnitudes are shown in Figure 3.5 for both the observed and the completeness-corrected samples (shaded and blue histograms, respectively). It can be seen that the conservative criteria adopted for the sample selection strongly limit the impact of incompleteness: the global correction to the adopted samples is smaller than 15%, with the completeness-corrected population of WDs counting 705 stars.

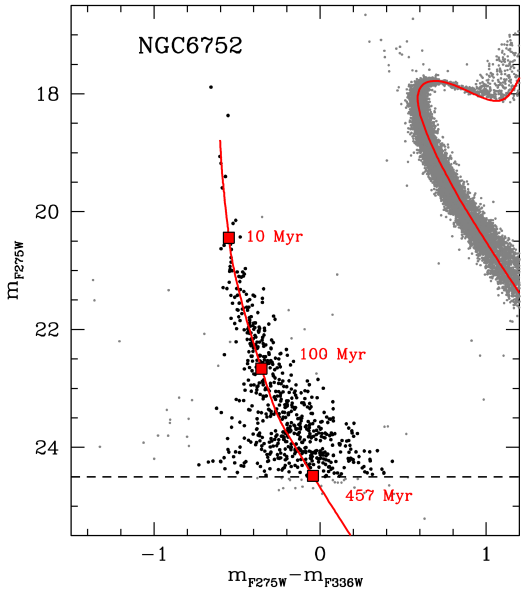

Figure 3.4: CMD on NGC 6752 zoomed on the WD cooling sequence, with the WD samples selected for analysis denoted by black dots. The red lines are the same set of theoretical models used in C21 to reproduce the evolutionary sequences observed in M13: a 12.5 Gyr old isochrone from the BaSTI dataset (Pietrinferni et al., 2006) well fitting the cluster MS, and the cooling sequence of a $0.54 M_{\odot}$ hydrogen atmosphere CO-WD from M. Salaris et al. (2010). The red squares flag three cooling ages along the cooling track. The dashed horizontal line marks the adopted magnitude limit of the analyzed WD sample, corresponding to a cooling age $t_{\rm cool} < 460$ Myr.

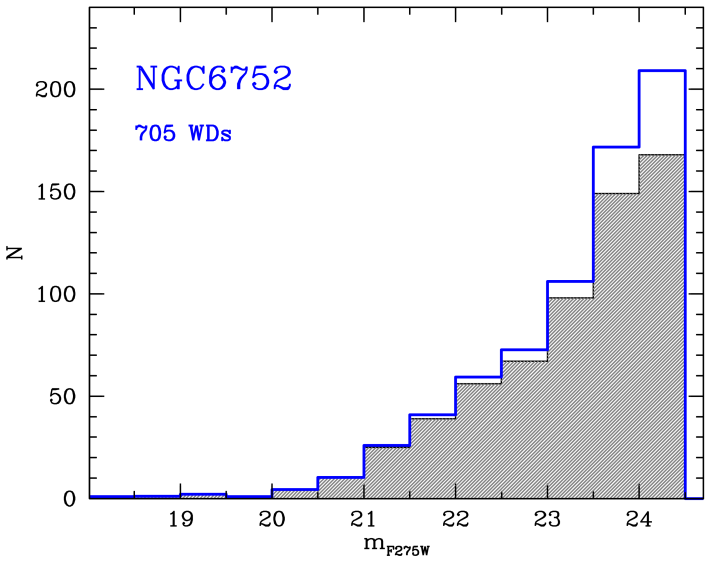

Figure 3.5: Observed and completeness-corrected luminosity functions (shaded and blue histograms, respectively) obtained from the selected WD sample (black dots in Figure 3.4).

3.3.2 Comparing the WD LF of NGC6752 and M13

For a proper comparison between the WD LFs of NGC 6752 and M13, we need to take into account the intrinsic mass of the two clusters. According to the procedure adopted in C21, we used as normalization the number of RGB stars. The stars are bright (corresponding to high completeness levels at any distance from the center), and for a given total stellar mass of the host population their number depends only on the evolutionary speed, which is the same in clusters with the same initial chemical composition and age (see, e.g., Renzini et al. 1986). Taking advantage of the excellent match obtained between the CMDs of the two clusters (see Fig. 3.2), the RGB population was selected in the observed CMD by using the same box adopted for M13, that samples the entire RGB extension down to its base (see Figure 3.6). Of course, the RGB stars have been counted in the same cluster area considered for the WD selection ($r > 10''$), providing a total of 335 objects.

The completeness-corrected number of WDs counted in the various magnitude bins, divided by the total number of RGB stars thus obtained, finally provided us with the WD LF normalized to the RGB reference population, shown in Fig. 3.7 (blue circles). The corresponding normalized WD LF of M13 (from C21) is plotted in the same figure in red for comparison. Although the WD LF of NGC 6752 reaches much fainter magnitudes than that of M13, the match between the results in the two systems is really impressive, with the portions in common being almost indistinguishable. This provides strong evidence that the two clusters share the same type of WD population, suggesting that also NGC 6752 hosts a relevant fraction of slowly cooling WDs, as expected from its HB morphology.

This expectation is also consistent with the conclusion by Cassisi et al. (2014) that the mass distribution along the HB in the two clusters is essentially the same, with the large majority of HB stars having masses smaller than $\sim 0.56 M_{\odot}$. According to theoretical models (BaSTI and Bono et al. 2020), at the considered metallicity ($Z = 0.001$), these stars do not experience the thermal pulse AGB stage during which the third dredge-up occurs. We can thus assume that, as in M13, approximately 70% of the WD progenitors in NGC 6752 end their evolution with hydrogen envelopes thick enough (a few $10^{-4} M_{\odot}$) to guarantee stable H-burning during the subsequent WD cooling stage. The same proportion between standard and slowly cooling WDs ($\sim$ 30% and 70%, respectively) is therefore expected in the two clusters.

To quantitatively test this prediction, the left panel of Fig. 3.8 compares the completeness-corrected cumulative LF, normalized to the number of RGB stars, of NGC 6752 WDs (thick blue line), with the results of Monte Carlo simulations of the entire evolutionary path from

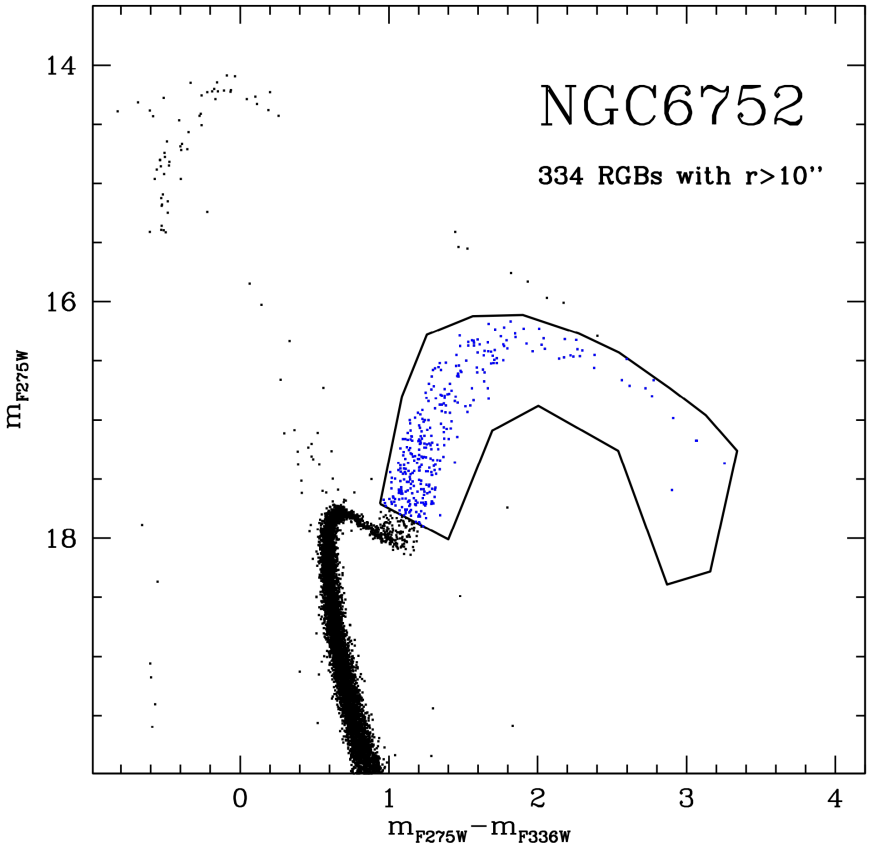

Figure 3.6: Selection box (black line) of the RGB sample (blue dots) in NGC 6752. The box is equal to that used in M13 (but for the color and magnitude shifts needed to align the two CMDs; see Figure 3.2). The number of RGB stars has been used as normalization factor of the WD samples to account for the different intrinsic richness of the two clusters.

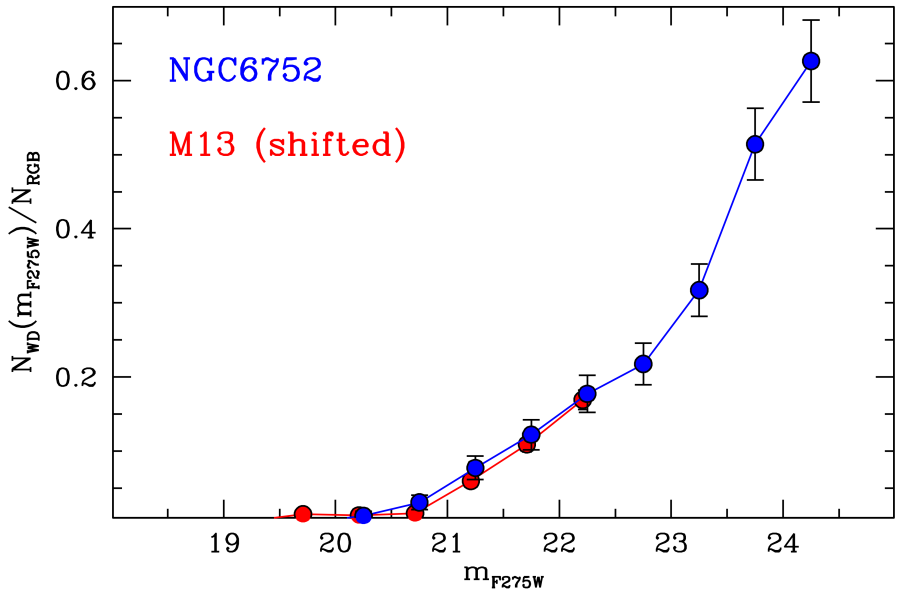

Figure 3.7: Completeness-corrected WD differential LFs, normalized to the number of RGB reference stars, for NGC 6752 (blue circles) and M13 (red circles). The same magnitude shift adopted in Fig. 3.2) has been applied to the LF of M13.

the RGB, to the HB and then the WD stages, specifically computed by adopting the HB mass distributions determined for M3 and M13 (see C21). The simulation including 100% of standard WDs (as observed in M3) corresponds to the dashed line in the figure, while the run including a combination of 30% standard WDs and 70% slowly cooling WDs is marked with the black solid line. As expected, the WD LF of NGC 6752 is in impressive agreement with the latter, demonstrating that, according to the cluster HB morphology, the WD population is dominated by a relevant fraction of slowly cooling objects. For the sake of comparison, the right panel of Figure 3.8 shows the normalized WD cumulative LF of M13 determined by C21, together with the same models plotted in the left panel. The faintest WDs sampled in NGC 6752 have luminosities of just $\sim 10^{-2.7} L_{\odot}$, significantly fainter than those probed in M13. Thus the results presented in this work provide further solid support to the existence of slowly cooling WDs, and to the scenario traced in C21 about their origin.

3.4 Conclusions

The key points linking the presence of slowly cooling WDs in a cluster to its HB morphology can be summarized as follows.

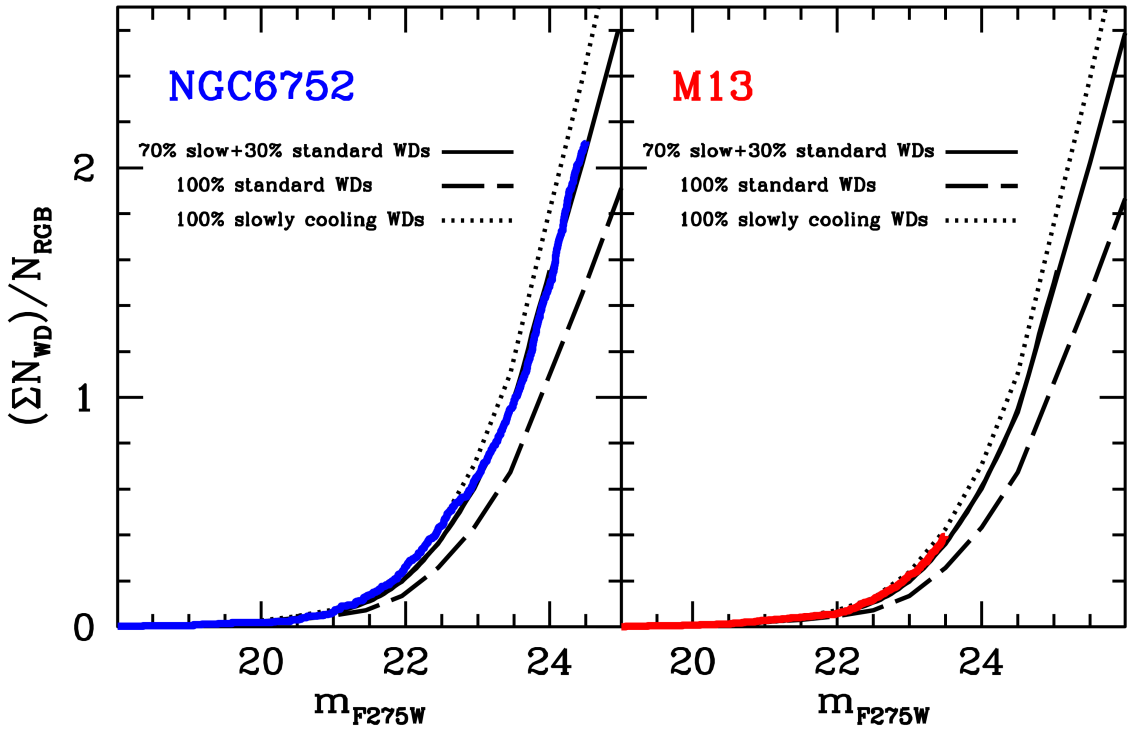

Figure 3.8: Left panel: WD cumulative LF of NGC 6752, corrected for completeness and normalized to the number of RGB stars (thick blue line), compared to the results of Monte Carlo simulations including 100% standard WDs (dashed line), 100% slowly cooling WDs (dotted line) and a combination of 30% standard WDs and 70% slowly cooling WDs (black solid line). Right panel: the same for M13 (red thick line, from C21).

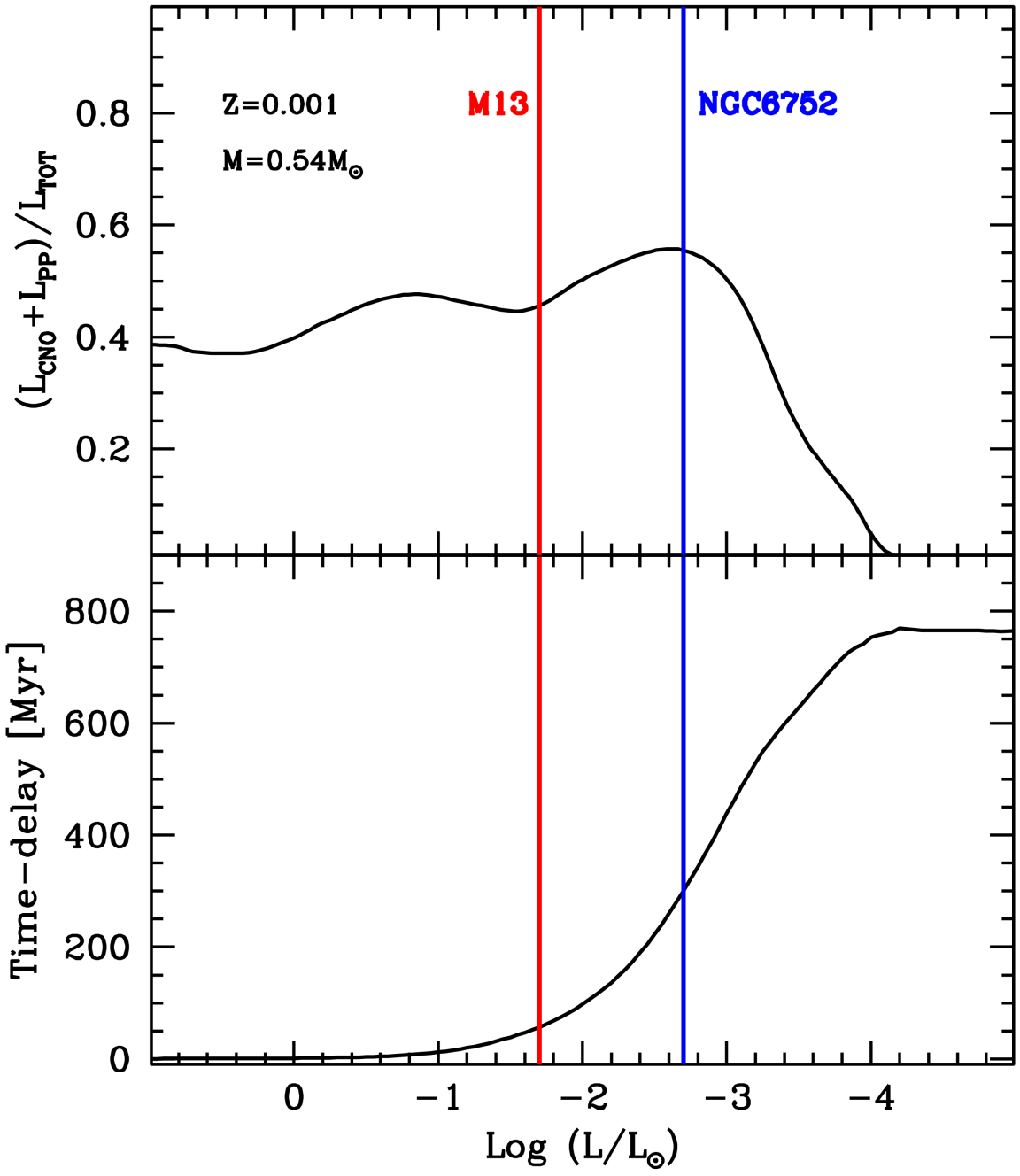

Figure 3.9: Top panel: Contribution of stable H-burning (via PP and CNO chain) to the luminosity of a low metallicity (Z=0.001), low mass (0.54 $M_{\odot}$) WD as a function of the luminosity. Bottom panel: Delay in the cooling time induced by stable H-burning, with respect to a model without burning. The two vertical lines mark the luminosity reached in NGC 6752 (present work) and in M13 (C21).

1. The energy support responsible for slowing down the cooling process is provided by stable H-burning in the WD external layers, which is made possible by the presence of a H-rich residual envelope containing enough mass (on the order of a few $10^{-4} M_{\odot}$; see, e.g., Renedo et al. 2010). More standard WDs like those in M3 have a H content below the threshold for H-burning ignition, and thus progressively cool in time with no sources of active energy production.

2. According to Leandro G. Althaus et al. (2015), the third dredge-up is the crucial event regulating the mass of the residual hydrogen in proto-WDs. In fact, during the third dredge-up carbon is carried into the convective envelope and, in turn, hydrogen is brought down inside the star, where it is burned. Thus, the occurrence (or lack thereof) of the third dredge-up affects the residual H envelope of the proto-WD when it reaches its cooling track, impacting its structure and cooling time.

3. Theoretical models (e.g., Bono et al. 2020) show that at $Z = 0.001$, HB stars with masses smaller than $\sim 0.56 M_{\odot}$ skip the thermal pulse AGB stage, where the third dredge-up occurs. This is because their envelope mass is so small that the alternate helium and hydrogen burning in shells surrounding the carbon-oxygen core cannot occur. Completely or partially skipping the AGB phase guarantees the survival of a residual hydrogen envelope in these stars when they evolve off the HB toward the WD stage: Hence, they will evolve as WDs with stable H-burning and a significant delay of their cooling time.

4. From stellar evolution theory it is also well known that HB stars with the above mentioned mass and metallicity populate the blue tail of the observed HBs.

As a result of this chain of events, significant populations of slowly cooling WDs are expected in globular clusters with well populated and extended blue HB morphologies.

By showing that NGC 6752, a Galactic GC with blue extended HB morphology, hosts a large sample ($\sim$ 70% of the total) of slowly cooling WDs, this work not only provides new evidence for the existence of this class of WDs, but also gives strong support to the picture above. Indeed, the fact that the same mixture of standard and slow WDs is able to reproduce the WD LFs observed in both NGC 6752 and M13, while 100% of standard WDs are needed for M3 (see C21), demonstrates the link between the cluster HB morphology and the presence of these stars, and provides empirical support to the proposed physical origin of these objects (i.e., the fact that they skip the third dredge-up). In fact, the only major

difference between M3 and the other two systems is the HB morphology: at odds with M3, NGC 6752 and M13 have a (remarkably similar) blue-tail HB, which is populated by such low-mass stars that they skip the third dredge-up and evolve in slowly cooling WDs.

While the WD cooling sequence in M13 samples luminosities down to $log(L/L_{\odot}) \sim -1.7$ (see C21), in NGC 6752 we reached luminosities one order of magnitude fainter, corresponding to much longer delay times with respect to the standard predictions for a pure cooling process. This is shown in Fig. 3.9, where the cooling time delay induced by stable H-burning, with respect to standard models of WDs with no burning is plotted as a function of the stellar luminosity. While the magnitude limit reached in M13 corresponds to a delay of $\sim$ 60 Myr, the limit achieved in NGC 6752 implies a delay time of $\sim$ 300 Myr, meaning that most of the faintest WDs in our adopted photometry have cooling ages of $\sim$ 760 Myr, instead of $\sim$ 460 Myr as standard models would suggest (see Figure 3.4).

The figure also shows that the contribution to the energy budget provided by the stable burning in the thin H-rich layer is essentially restricted to $\log(L/L_{\odot}) > -4$ for a low mass WD (0.54 $M_{\odot}$) at intermediate metallicity (Z=0.001). According to the models, this luminosity corresponds to a cooling age of approximately 3.5 Gyr, and during this time the accumulated delay in the cooling process can be as large as 0.8 Gyr . An exhaustive exploration of the entire H-burning phase down to magnitudes corresponding to at least $\log(L/L_{\odot}) \sim -4$ is thus required, to obtain an empirical measurement of the total amount of cooling delay induced by this mechanism.

It is worth emphasizing that the predictions shown in Figure 9 refer to a single-mass WD, whilst the modeling of the faintest end of the WD LF is much more complex. In fact, the bright portion of the cooling sequence can be well approximated by a single mass ($\sim 0.54 M_{\odot}$) cooling track, but at the faintest end the contribution of WDs with larger masses must be taken into account to properly characterize the impact of the H-burning on the WD LF. In the case of NGC 6752, which is the portion of the WD cooling sequence that is expected to be affected by the presence of slow WDs? As discussed above, slowly cooling WDs are the progeny of the (bluest) HB stars with mass below $0.56 M_{\odot}$, that skip the AGB thermal pulses. In 12-13 Gyr old clusters, the initial mass of stars on the RGB scales as $dM/dt = -0.02 M_{\odot}/Gyr$. Hence, given the current RGB mass in NGC 6752 ($\sim 0.8 M_{\odot}$), we expect that about 3 Gyr ago RGB stars had a mass around $0.86 M_{\odot}$. Under the reasonable assumption that the amount of mass lost along the RGB is approximately constant for low-mass stars of similar initial masses, this implies that about 3 Gyr ago (and even earlier in the cluster life) all the core He-burning stars had a mass above $0.56 M_{\odot}$ and thus have all

evolved through the thermal pulses along the AGB, producing 'normal' WDs. Hence, all the WDs with cooling age larger than 3 Gyr (which corresponds to $m_{F275W} \sim 31$) are expected to be normal WDs, and slowly cooling WDs are predicted to affect only the portion of the WD cooling sequence brighter than $m_{F275W} \sim 31$, with an importance that progressively decreases at fainter magnitudes down to this limit.

While the results presented here and in C21 provide a solid demonstration of the existence of slowly cooling WDs at intermediate metallicities ($Z = 0.001$), the extension of this investigation to fainter magnitudes and other metallicity regimes is now necessary to fully verify the theoretical predictions and provide an empirical measure of how common this phenomenon is in stellar systems. This is of paramount importance for the correct use of the WD cooling sequences as chronometers to measure cosmic ages.

Chapter 4

The "canonical" White Dwarf Cooling Sequence of M5

Mainly based on Chen et al. 2023, ApJ, accepted.

4.1 Introduction

White Dwarfs (WDs) constitute the ultimate evolutionary stage of stars with low and intermediate initial mass (below $8M_{\odot}$, possibly up to $11M_{\odot}$; e.g., Córsico et al., 2019). This mass range indeed includes the overwhelming majority ($\sim$ 98%; e.g., Winget et al. 2008; Woosley et al. 2015) of stars in our universe. As ending point of stellar evolution, WDs gather tremendous information about the evolutionary history of their progenitors. In addition, they are characterized by relatively simple structures, thus providing the ideal laboratory for studying the behaviour of matter in extreme high-density physical conditions (E. Garcia-Berro et al., 1995).

WDs are thought to be the remnant core of a star that has terminated its thermonuclear activity and has released its outer layers. Because tof the lack of energy production by thermonuclear reactions or gravitational contraction, the evolution of WDs is generally described as a progressive cooling process. Thus, WD aging is essentially characterized by a progressive cooling and fading at fixed radius as a function of time (the so-called "cooling time"). This provides a natural link between WD luminosities and their cooling ages, which

is often adopted as a cosmic chronometer to measure the age of stellar populations in the Galaxy (as the Galactic disk, globular and open clusters; see e.g., Bedin et al. 2010, 2023; Bellini et al. 2010; Hansen et al. 2007; Mukremin Kilic et al. 2017).

However, recent theoretical models (Leandro G. Althaus et al., 2015) have shown that a small amount of residual hydrogen (a few $10^{-4} M_{\odot}$) left on the WD surface from the previous evolutionary stages is sufficient to allow quiescent thermonuclear burning. This process provides a non-negligible source of energy that can significantly decrease the cooling rate with respect to that of normal WD, especially in the low-mass ($< 0.6 M_{\odot}$) and low-metallicity ($Z < 0.001$) regime (Miller Bertolami et al., 2013; Renedo et al., 2010), thus generating a new class of WDs that we named "slowly cooling WDs". The cooling time-scale increase is expected to enhance to number of WDs in the brightest portion of the cooling sequence, with an observable modification of the shape of the WD Luminosity Function (LF). In turn, this implies that the effect of possible residual hydrogen burning cannot be neglected in the reading of the cooling time (hence, the WD age) along the cooling sequences, especially in Galactic globular clusters (GGCs) that are the oldest and most metal-poor stellar populations in the Milky Way (thus hosting populations of low-mass and low-metallicity WDs).

The first observational evidence of the existence of slowly cooling WDs has been presented by Chen et al. (2021) who compared the WD LFs of "twin clusters" (M13 and M3) and discovered a significant WD excess in the former. These two clusters share many physical properties (e.g., the metallicity, age, central density, etc.; Dotter et al., 2010; Harris, 1996), with the notable exception of the Horizontal Branch (HB) morphology, which is completely different in the two systems (Dalessandro et al., 2013b; Francesco R. Ferraro et al., 1997). In fact, the HB morphology in M13 is characterized by an extended blue tail (see also Francesco R. Ferraro et al. 1998), while no blue extension is present in the HB of M3 (Buonanno et al., 1994; F. R. Ferraro et al., 1997). Chen et al. (2021) confirmed that the HB morphologies are related to the presence or lack thereof of slowly cooling WDs, because they correspond to quite different mass distribution: stellar masses increase from the blue edge to the red edge of the HB, implying that most of the HB stars in M13 are less massive than that in M3. On the other hand, the stellar mass in the HB phase is the key parameter that sets the subsequent evolution, in particular the occurrence of the third dredge-up, a mixing process occurring during the Asymptotic Giant Branch (AGB), which is the evolutionary phase immediately following the HB and preceding the WD stage. This process efficiently mixes the material present in the envelope of AGB stars, bringing most of the hydrogen deep into the interior where it is burned. As a consequence, a star experiencing the third

dredge-up arrives to the WD stage essentially exhausted, with no residual hydrogen to burn. Conversely, stars skipping this critical event, reach the WD stage with a residual hydrogen envelope thick enough to allow stable thermonuclear burning, and this provides the WD with an extra-energy production that delays its cooling. Theoretical models (Leandro G. Althaus et al., 2015) demonstrate that extremely low-mass HB stars (less massive than $0.56 M_{\odot}$ at intermediate metallicities) do not experience the third dredge-up. Thus, while all the (red) HB stars in M3 are more massive than this value and are therefore expected to experience the third dredge-up in AGB, approximately 70% of the stars in M13 populating the HB blue tail are predicted to skip this event and thus produce slowly cooling WDs: this is exactly the proportion needed to explain the difference detected in the two WD LFs. This scenario has been fully confirmed by Chen et al. (2022) in the case of NGC 6752, which is a GGC with almost the same metallicity and the same (extended blue) HB morphology of M13, where, consistently, $\sim$ 70% of WDs have been found to be slowly cooling, and $\sim$ 30% of them are canonical WDs. The results obtained in M13 and NGC 6752 therefore provided firm evidence of the existence of slowly cooling WDs and solid empirical support to the predicted physical origin of these objects (i.e., the fact that they skip the third dredge-up in AGB). This also consolidated the connection between the occurrence of this phenomenon and the HB morphology: significant populations of slowly cooling WDs are expected in GCs with well populated and extended blue-tail HB morphologies.

To further verify the scenario in the case of a cluster with no HB blue extension, in this paper we use deep near-ultraviolet photometry secured with the HST to investigate the LF of the brightest portion of the WD cooling sequence in M5. This is a luminous ($M_V = -8.8$) and well studied GGC (e.g. F. R. Ferraro et al., 2012; B. Lanzoni et al., 2007a, 2016, 2018; Miocchi et al., 2013; Nardiello et al., 2018; Pallanca et al., 2014; Piotto et al., 2015)), relatively close to the Sun (at a distance of $\sim$ 7.5 kpc). The HB morphology of M5 is similar to that of M3, with no blue tail extension, and characterized by a rich population of RR Lyrae (Arellano Ferro et al., 2016a,b). According to the scenario discussed above this should imply that most of the HB stars in M5 experience the third dredge-up and end their evolution as canonical WDs.

The paper is organized as follows: in Section 4.2, we describe the data reduction and artificial star tests; the WD sample selection and analysis are presented in Section 4.3; the discussion and conclusions of the work are provided in the Section 4.4.

4.2 Data reduction

In this work, we use the deep and high-resolution photometric data in the near-ultraviolet band, obtained with the HST/WFC3 camera in the UVIS channel. The dataset has been acquired as a part of the HST Large Legacy Treasury Program (GO-13297, PI: Piotto; see Piotto et al., 2015 and it is composed of 4 frames (two with exposure time $t_{\rm exp}$ = 689s, two with $t_{\rm exp}$ = 690) in the F275W filter, and 4 frames (each with $t_{\rm exp}$ = 306s) in the F336W filter.

For the photometric analysis we used UVIS exposures with "$\_flc$" extension, which are calibrated and corrected for Charge Transfer Efficiency (CTE). After the pre-reduction procedure, which includes the extraction of the science images (chip1 and chip2) from the raw fits files and the application of the Pixel Area Map correction, in order to derive the star magnitudes we performed a Point Spread Function (PSF) fitting following the so-called "UV-route". This is a photometric procedure specifically optimized for the detection of blue and hot objects, such as hot HB stars, blue straggler stars, and WDs in crowded fields (see, e.g., Dalessandro et al., 2013a,b; F. R. Ferraro et al., 1997, 2018; Francesco R. Ferraro et al., 1997, 2001a, 2003a; B. Lanzoni et al., 2007a; S. Raso et al., 2017). In particular, S. Raso et al. (2017) discussed the net advantages of using this *UV-Guided* search of the sources with respect to the standard *optical-driven* selection, in order to derive complete samples of blue and faint objects in high-density old clusters, where the optical emission is primarily dominated by a large population of bright and cool (3500 – 5000 K) giants. Specifically, in this paper we followed the approach described in M. Cadelano et al. (2019) and Mario Cadelano et al. (2020)(but see also Chen et al. 2021, 2022; S. Raso et al. 2017; Silvia Raso et al. 2020). The main idea of the procedure is to created a master list of sources detected in the near-ultraviolet images and then force the detection in images acquired at longer wavelengths (as blue and optical bands).

In short, we first selected about $\sim$ 250 bright and unsaturated stars uniformly distributed in the entire field of view to properly model the PSF function for each exposure. We then applied the resulting model to all the sources detected above 5σ from the background, and combined the stars appearing in at least 2 images, thus building the master list. Secondly, we performed the "forced" photometry with DAOPHOT/ALLFRAME (Stetson, 1994) on all the images at positions corresponding to the stars in the master list, even in a location where the signal is below 5σ. Finally, the magnitudes of all stars in each filter were homogenized, and the magnitudes and corresponding errors were calculated from their weighted mean and

standard deviation.

After correcting the instrumental positions for geometric distortions, we calibrated instrumental magnitudes to the VEGMAG system and aligned the instrument coordinates to the International Celestial Reference System by cross-correlation with the reference catalog of the HSTHST UV Globular Cluster Survey (Nardiello et al., 2018; Piotto et al., 2015). We also executed an additional visual inspection to clean up the sample from fake sources caused by saturation of extremely bright stars. As a result of the data reduction process, a final catalog listing almost 40,000 stars has been finally obtained.

4.2.1 Color-magnitude diagram

The Color Magnitude Diagram (CMD) obtained for M5 is presented in Figure 4.1. As can be seen, all the main evolutionary sequences are clearly defined and they appear negligibly affected by contamination from field stars or background extra-Galactic sources. The CMD extends from $m_{\rm F275W} = 15$ to $m_{\rm F275W} \simeq 25$, spanning more than 10 magnitudes and thus providing a panoramic over-view of the stellar population hosted in the cluster. As expected, the near-ultraviolet CMD appears significantly different from the "classical" one in the optical bands: the luminosity of red giant branch (RGB) stars is significantly suppressed (the RGB-tip is at $m_{\rm F275W} \sim 19$), and the same holds for the AGB, which is clearly distinguishable from the RGB in the color range $1.6 < (m_{\rm F275W} - m_{\rm F336W}) < 3$. The luminosity in the F275W band is instead dominated by HB stars, clearly visible at $(m_{\rm F275W} - m_{\rm F336W}) < 1.2$. A well defined sequence of blue straggler stars (see also B. Lanzoni et al., 2007a) is seen emerging from the main sequence turn-off (MS-TO, at $m_{\rm F275W} \sim 19$) and extends up to the HB at $m_{\rm F275W} \sim 16$. A copious population of RR Lyrae (observed at random phases) is also distinguishable as a sort of stream of stars diagonally crossing the HB at $0.5 < (m_{\rm F275W} - m_{\rm F336W}) < 1$. The brightest portion of the WD cooling sequence appears as a well-defined and populated, almost vertical sequence at $(m_{\rm F275W} - m_{\rm F336W}) \sim -0.8$, extending for amost 6 magnitudes from $m_{\rm F275W} \sim 25.5$ up to $m_{\rm F275W} \sim 19$.

The overall morphology of the CMD appears to be very similar to that observed in M3. This can be easily appreciated in Figure 4.2, where the CMD of M3 (from Chen et al. 2021) has been shifted to match the color and magnitude location of the evolutionary sequences of M5. Indeed, apart from the slightly different metal content ([Fe/H]= -1.5 and [Fe/H]= -1.3 for M3 and M5, respectively; see Harris 1996) that introduces some second-order differences, the evolutionary sequences in the two clusters (M3 and M5) are impressively similar. In particular, the color extension of the HB is fully comparable, with the extremely blue part,

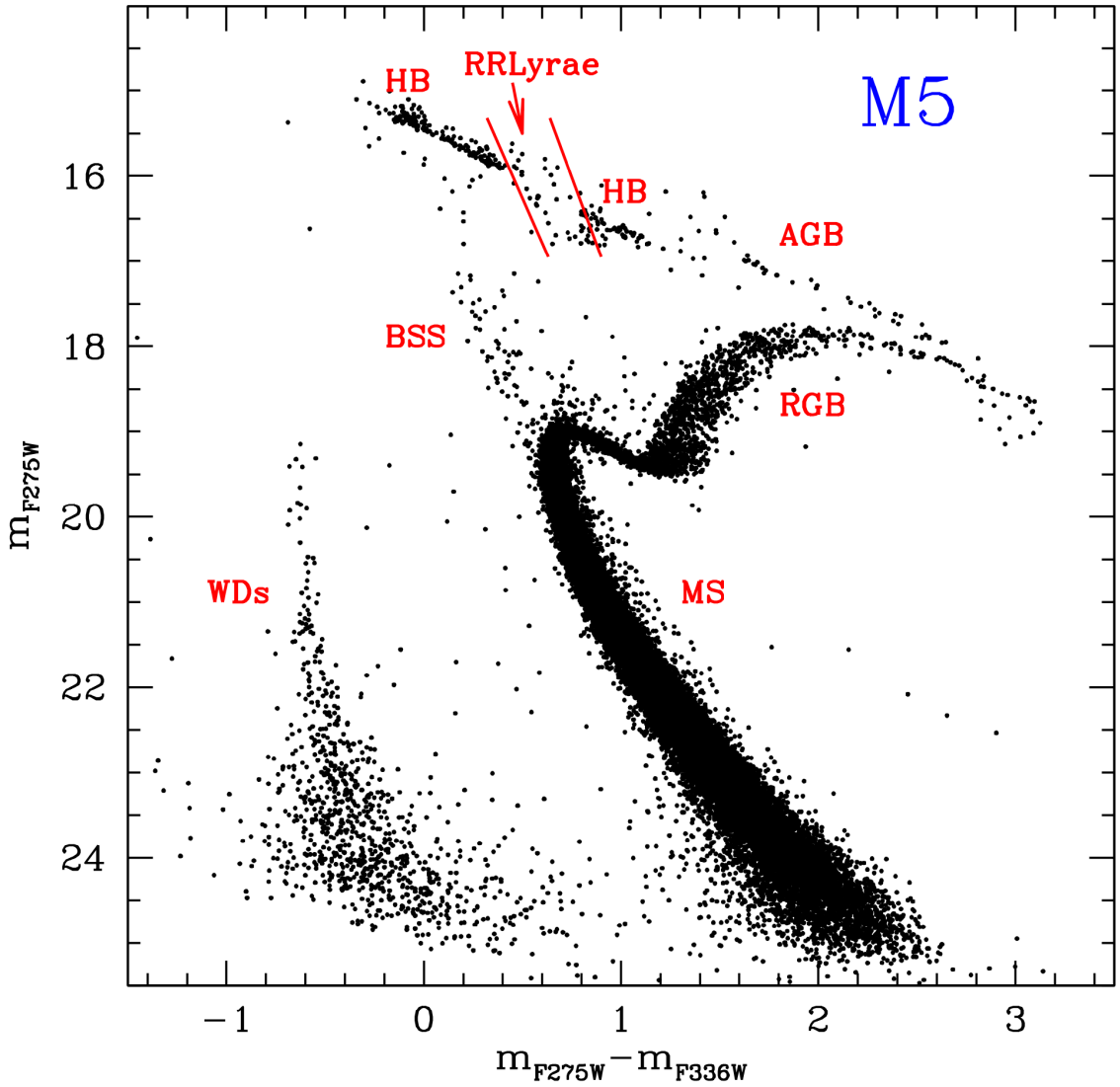

Figure 4.1: The near-ultraviolet color-magnitude diagram of the 39114 stars detected in M5. The various stellar populations are indicated. The two red lines delimitate the CMD region where most of the RR Lyrae are found..

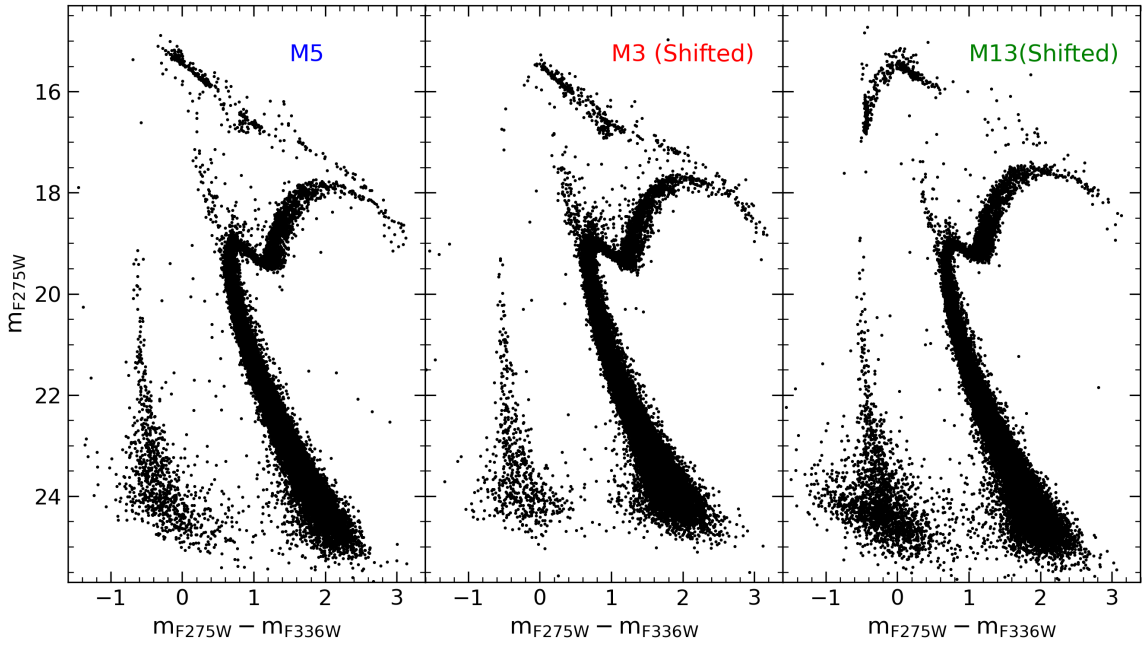

Figure 4.2: CMD of M5 *(left panel)* compared to those of M3 *(middle panel)* and M13 *(right panel)*. CMDs of M3 and M13 (from Chen et al. (2021) have been shifted, respectively, by $\Delta m_{F275W} = -0.35$ and $\Delta m_{F275W} = +0.20$ in magnitude and by $\Delta(m_{F275W} - m_{F336W}) = +0.13$ and $\Delta(m_{F275W} - m_{F336W}) = +0.07$ in color.

at $(m_{F275W} - m_{F336W}) < -0.1$, being essentially not populated in both cases. For the sake of comparison, in the same figure we also included the CMD of M13 (from Chen et al. 2021, shifted to match the color and magnitude location of the evolutionary sequences of M5) which instead shows a clearly different HB morphology with a pronounced blue tail population. The impressive similarity of the HB morphologies in M5 and M3 suggests an analogous post-HB evolutionary path for the stars in these two clusters, surely different from that expected in M13. Thus, on the basis of the HB morphology a population of canonical WDs (similar to that found in M3) and no presence of slowly cooling WDs (as those observed in M13) are expected in M5.

4.2.2 Artificial star tests

In order to perform a meaningful quantitative study of the properties of the LF of faint objects like WDs, a mandatory step is the empirical determination of the level of photometric completeness of the WD cooling sequence at different levels of magnitudes and distances from the cluster centre. This procedure should provide a first-order estimate of the amount

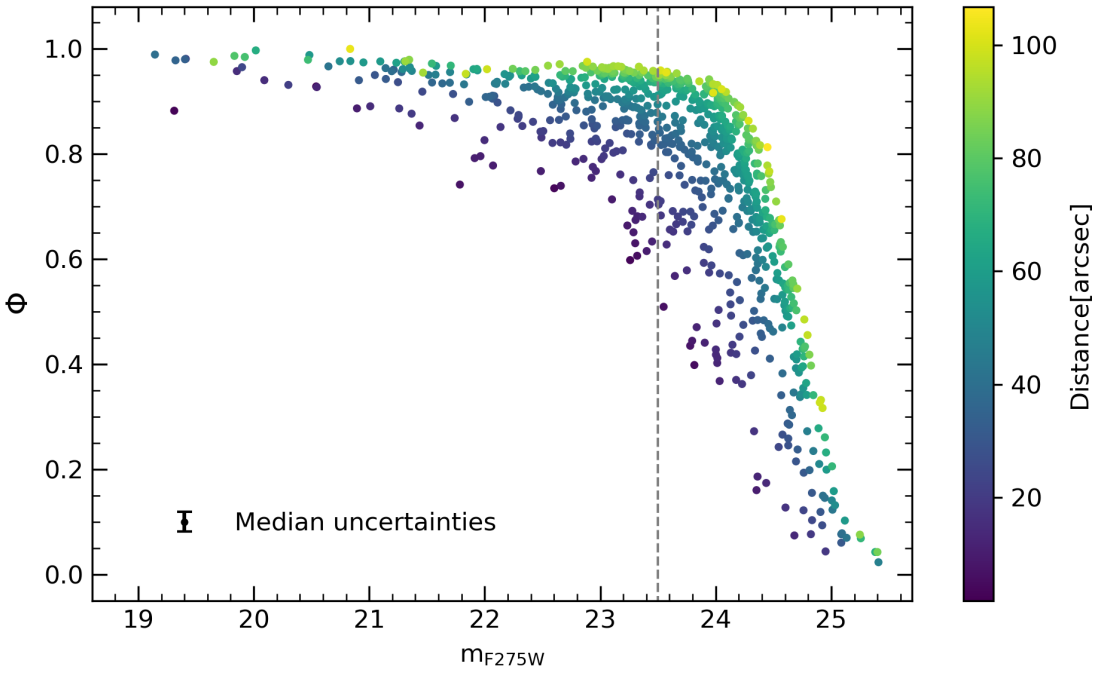

Figure 4.3: Completeness parameter Φ of the selected WDs as a function of the $m_{\rm F275W}$ magnitude, with the radial distance from the cluster center color-coded as indicated in the colorbar. The median uncertainty on Φ is marked in the panel. All the WDs located on the left of the vertical dashed line have completeness $\Phi > 0.5$.

of sources lost during the data reduction process because of their intrinsic faintness and the level of crowding of the surrounding environment. The evaluation of the photometric completeness was performed by means of extensive artificial star experiments. The standard recipe to perform these tests is described in detail in Bellazzini et al. (2002)(see also M. Cadelano et al. 2020; Chen et al. 2021; Dalessandro et al. 2015), thus here we just summarize the main steps of the procedure adopted for M5. As first step, we created a list of artificial stars with an input F275W magnitude sampling the observed extension of the WD cooling sequence. As apparent from Figure 4.1, the WD cooling sequence in M5 extends from $m_{\rm F275W} \approx 19$ to $m_{\rm F275W} \approx 25.5$. For each of these stars a corresponding magnitude in the F336W filter was assigned according to the mean ridge line of the WD cooling sequence in the $(m_{\rm F275W}, m_{\rm F275W} - m_{\rm F336W})$ CMD. A large number of artificial stars were generated and then added to each real image with DAOPHOT/ADDSTAR software. All artificial stars were placed into the images following a regular grid of 23×23 pixels (corresponding to about 15 times the FWHM of the stellar sources). Note that to avoid an artificial increase of the crowding conditions, only one artificial star was arranged in each cell. The entire photometric analysis was then repeated following exactly the same procedure described in Section 4.2. The procedure was then iterated several times to ensure a sufficiently large sample and, at the end, more than 160,000 artificial stars were simulated in the entire field of view that covers a region within approximately 90″ from the cluster center.

To quantify the level of photometric completeness, the completeness parameter Φ was determined as the ratio between the number of artificial stars recovered N_r by the photometric analysis, and the number of stars that were actually simulated (number of input stars, N_i). Of course the value of Φ is expected to be strongly dependent on both crowding (hence, the distance from the cluster center) and luminosity: it commonly decreases in the innermost regions of the clusters (due to the large stellar density) and at faint magnitudes. To properly trace both these effects, we divided the sample of simulated stars in radial bins at different distances from the cluster center (with steps of 5″) and in F275W magnitudes bins (in steps of 0.5 mag) and, for each cell of this grid, we counted the number of input and recovered stars, calculating the corresponding value of Φ. The computed value of Φ was then assigned to each WD according to its radial position and magnitude. The size of the adopted magnitude and radial distance steps was set to guarantee a reasonable statistics, while maintaining a sufficiently high spatial resolution and sensitivity of the Φ parameter to the stellar luminosity. The uncertainties on the completeness value (σ_Φ) were computed by propagating the Poissonian errors, and typically are on the order of 0.05. The radial

distances have been computed with respect to the center of gravity quoted in B. Lanzoni et al. (2007a)(see also B. Lanzoni et al. 2010; Barbara Lanzoni et al. 2019; Miocchi et al. 2013 for the details on the method adopted to estimate GC centers), which is located at right ascension $\alpha_{J2000} = 15^{h}\,18^{m}\,33^{s}.53$, and declination $\delta_{J2000} = +02°04'57''.06$, with a 1σ uncertainty of $0.''5$ in both the coordinates. The construction of such a completeness grid allowed us to assign the appropriate Φ value to each observed WD, with given F275W and F336W magnitudes, and located at any distance from the cluster center. The behavior of the completeness parameter as a function of the magnitude is shown in Figure 4.3 for all the detected WDs. According to previous works, we limited the analysis of the WD LF to the brightest portion of the cooling sequence ($m_{F275W} < 23.5$), where the completeness level is larger than 50% at any cluster-centric distance.

4.3 Analysis

4.3.1 Sample selection and WD LF

Figure 4.4 shows a portion of the CMD of M5 zoomed in the WD region. Overplotted to the data is the Carbon-Oxygen (CO) WD cooling track (M. Salaris et al., 2010) of a $0.54M_{\odot}$ with hydrogen atmosphere. As apparent, it nicely reproduces the observed cooling sequence even in its brightest portion. For the sake of comparison we also overplotted a 12.5 Gyr, α-enhanced isochrone with metal abundance $Z = 0.002$ and helium mass fraction $Y = 0.248$ extracted from the BaSTI models (Pietrinferni et al., 2006; see also Hidalgo et al., 2018; Pietrinferni et al., 2021), which well reproduces the MS-TO region of the cluster.

For a proper study of the LF, we selected a sample of *bona fide* WDs by following the same procedure already adopted in previous papers (see Chen et al. 2021, 2022): (1) we considered all the objects located within 3σ from the mean ridge line of the WD cooling sequence, with σ being the photometric error at the corresponding magnitude level, and the mean ridge line essentially corresponding to the $0.54M_{\odot}$ WD track; (2) as discussed above, we conservatively retained only WDs with completeness level above 50%, thus limiting the sample to WDs brighter than $m_{F275W} > 23.5$ mag. This magnitude cut corresponds to a cooling time of ~ 100 Myr, which is comparable to the threshold adopted in the case of M3 and M13 by Chen et al. 2022.

With the adopted selection criteria we selected a total of 311 WDs in M5. Their LF, computed in bins of 0.5 magnitudes, is shown in Figure 4.5 for both the observed and the

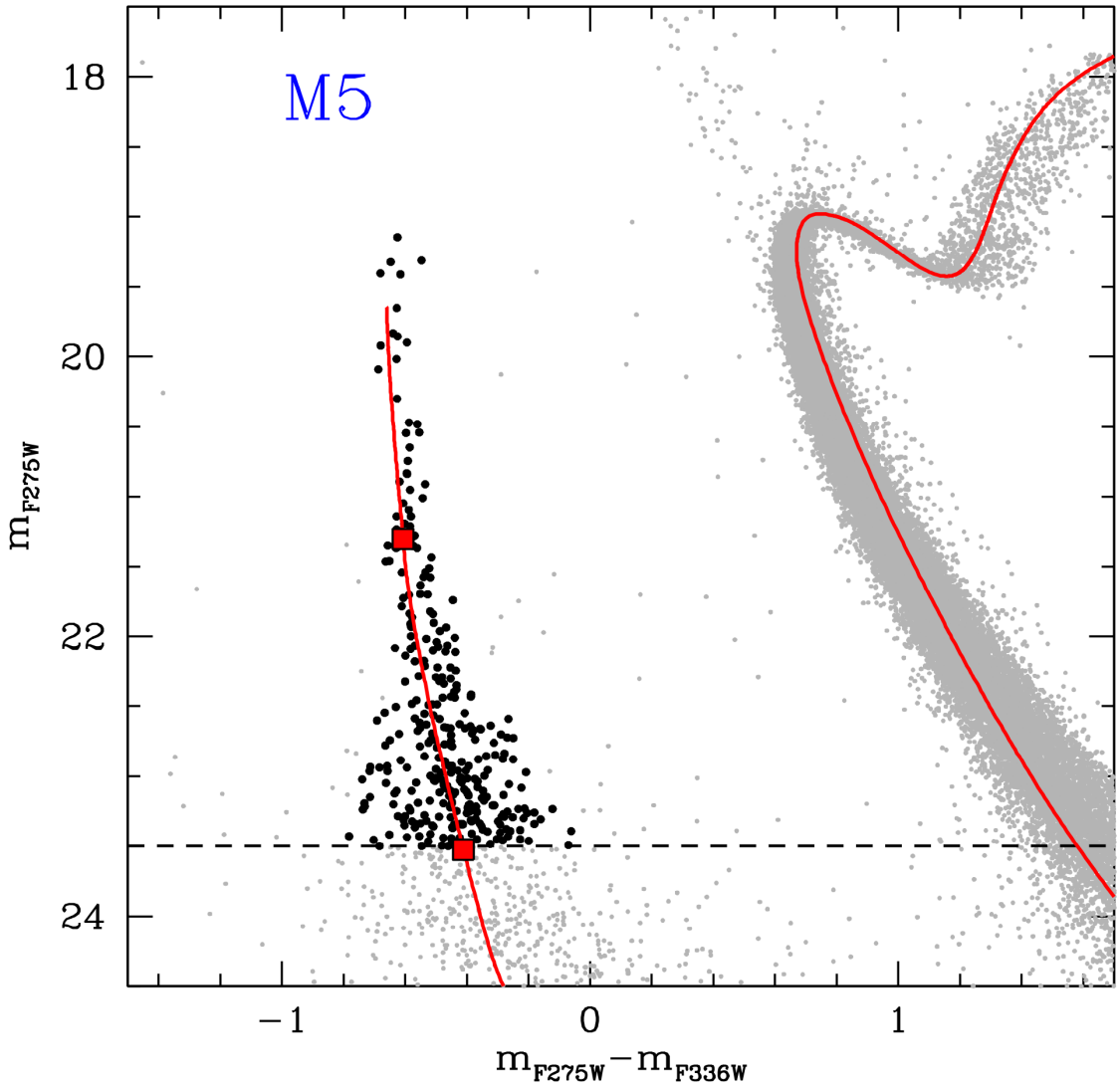

Figure 4.4: CMD of M5 zoomed in the WD Cooling sequence region. The analyzed WDs are marked with black dots, and the cut-off magnitude is marked with the horizontal dashed line located at $m_{\rm F275W} = 23.5$. The red line is the cooling track of a $0.54 M_{\odot}$ WD, along which two reference cooling ages (10 and 100 Myr) are marked with red squares. The 12.5 Gyr old isochrone (with $Z = 0.002$ and helium mass fraction $Y = 0.248$) from the BaSTI models (Hidalgo et al., 2018; Pietrinferni et al., 2021) well reproducing the cluster MS-TO is also plotted $0.54 M_{\odot}$ WD for reference.

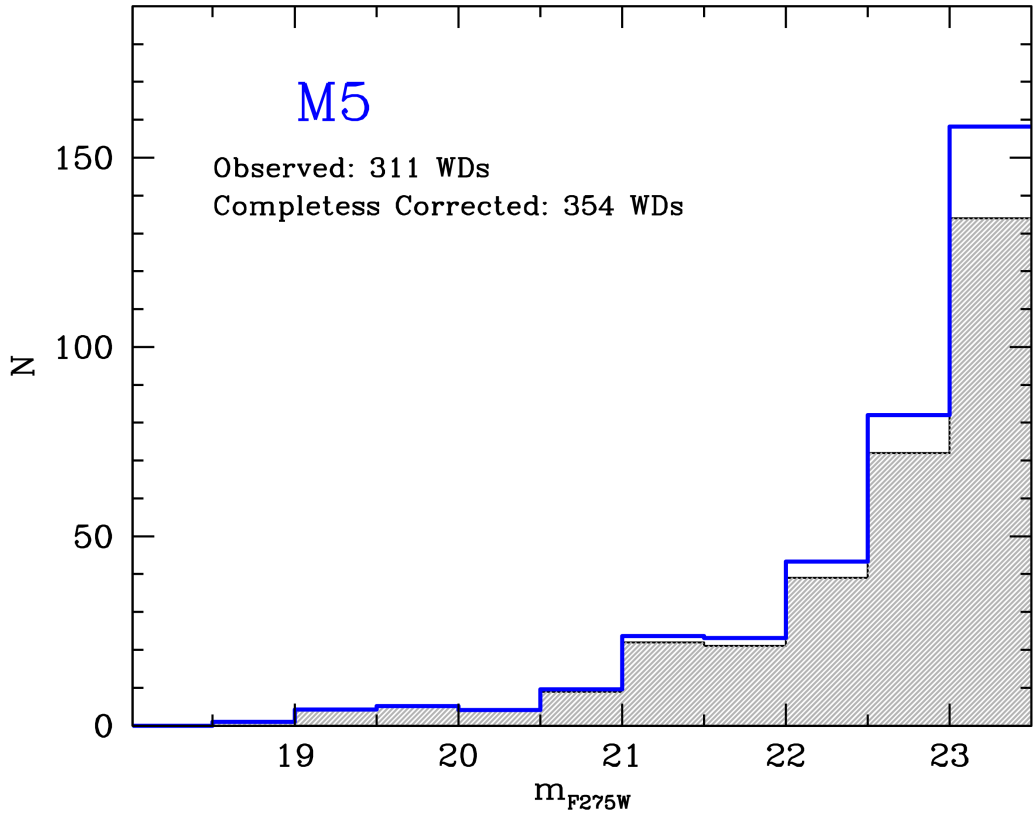

Figure 4.5: Observed (grey shaded) and completeness-corrected (blue) LF of the selected WD sample in M5.

completeness-corrected samples (grey shaded and blue histograms, respectively). It is worth of noticing that the conservative criteria adopted for the sample selection strongly limit the impact of incompleteness: the global correction to the adopted samples is smaller than 14% (43 stars in total), with the completeness-corrected population of WDs counting 354 stars.

4.3.2 Comparing WD LFs

We can now compare the completeness-corrected WD LF of M5 with those previously obtained for the two twin clusters M3 and M13 (see Chen et al., 2022). Intriguingly, both the limiting magnitude and the total number of WDs selected in M5 are very similar to those of M3. Indeed, this already suggests that the LFs observed in these clusters can be compared directly, with no need of normalization factors. In addition, by adopting the integrated apparent luminosity quoted by Harris (1996), and the distance modulus and reddening values listed in F. R. Ferraro et al. (1999, see also Table 4.2), we found that the

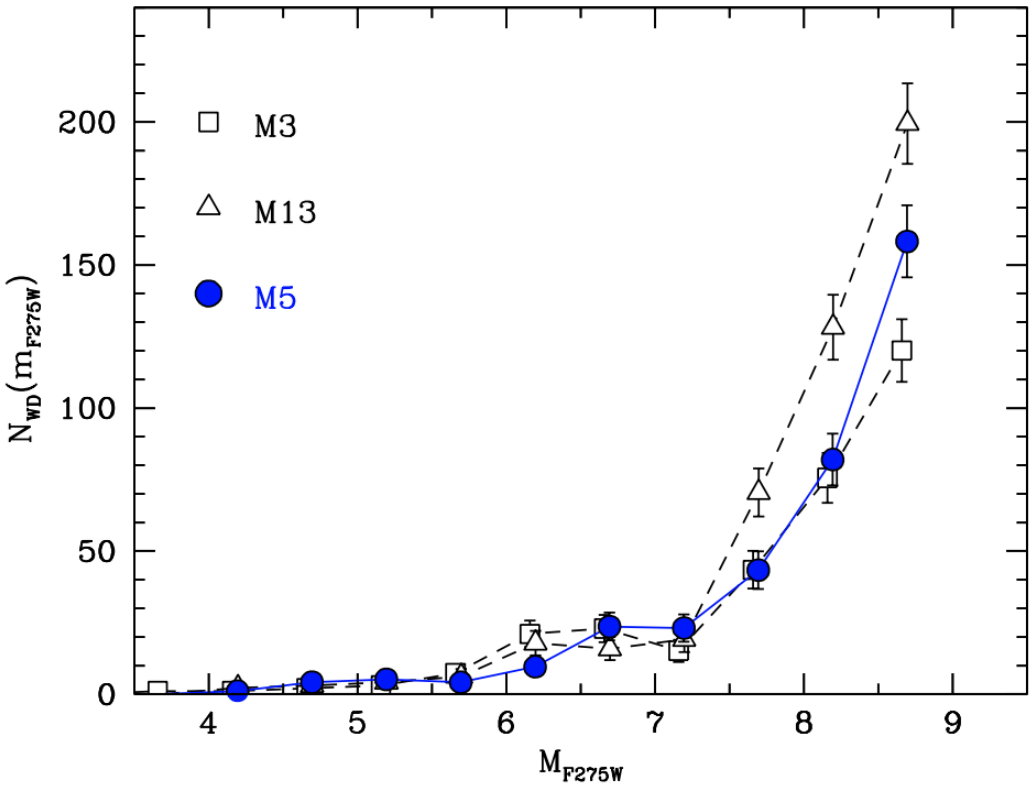

Figure 4.6: Completeness-corrected WD LF of M5 (blue circles), compared to that of M3 (empty squares) and M13 (empty triangles). The apparent m_{75W} magnitude has been transformed in absolute magnitude by adopting distance modulus and reddening of each cluster (from F. R. Ferraro et al. 1999; see also Table 4.2).

Table 4.1: Photometric and structural parameters of M5, M13 and M3

Cluster	$(m-M)_0$	$E(B-V)$	V_t	r_c	c	M_V	$L_{\rm sampled}$
M5	14.37	0.03	5.65	$28''$	1.66	-8.81	$1.67\times10^5 L_\odot$
M3	15.03	0.01	6.19	$22.7''$	1.85	-8.87	$1.78\times10^5 L_\odot$
M13	14.43	0.02	5.78	$49.5''$	1.32	-8.71	$1.25\times10^5 L_\odot$

Table 4.2: V_t is the total integrated $V-$band magnitude (from Harris, 1996); $(m-M)_0$ and $E(B-V)$ are, respectively, the distance modulus and reddening (from F. R. Ferraro et al., 1999); M_V is the derived absolute magnitude; $L_{\rm sampled}$ is the luminosity sampled by the observations, obtained from the integration of the best fit king model to the star density profile of each system (from Miocchi et al., 2013).

integrated absolute magnitudes of the three clusters are quite similar (~ -8.8; see Table 4.2), thus indicating comparable total masses and total numbers of stars. According to this evidence, we then compared the three WD LFs in terms of absolute star counts (with no normalization) as a function of the absolute F275W magnitude ($m_{\rm F275W}$). As can be seen from Figure 4.6, the LFs of M3 and M5 appear to be very similar, and they are both clearly different from the LF of M13.

To double check this result and for a more rigorous comparison (taking into proper account the slightly different intrinsic richness of each cluster), we then determined the total luminosity sampled by the adopted observations. The HST-WFC3 pointings sampled the innermost $\sim 90''$ from the center of each cluster. However, due to the different intrinsic structures in terms of core radius and concentration (Miocchi et al. 2013; see Table 4.2), this may correspond to different fractions of the total luminosity. Thus, We therefore estimated the amount of total luminosity sampled at $r < 90''$ in each system by integrating the corresponding best-fit King model from Miocchi et al. (2013). The results are listed in the last column of Table 4.2 and show that the differences are admittedly small (of the order of $10-15\%$). However, they go in the direction of making the WD LF of M5 more similar to that of M3 and increase the difference with the LF of M13, as clearly apparent from Figure 4.7, which shows the WD LFs normalized to the sampled luminosities in units of $10^5 L_\odot$. Thus the number of WDs per $10^5 L_\odot$ sampled luminosity with a cooling time < 100 Myr turns out to be are approximately an half $(47-56\%)$ of that counted in M13.

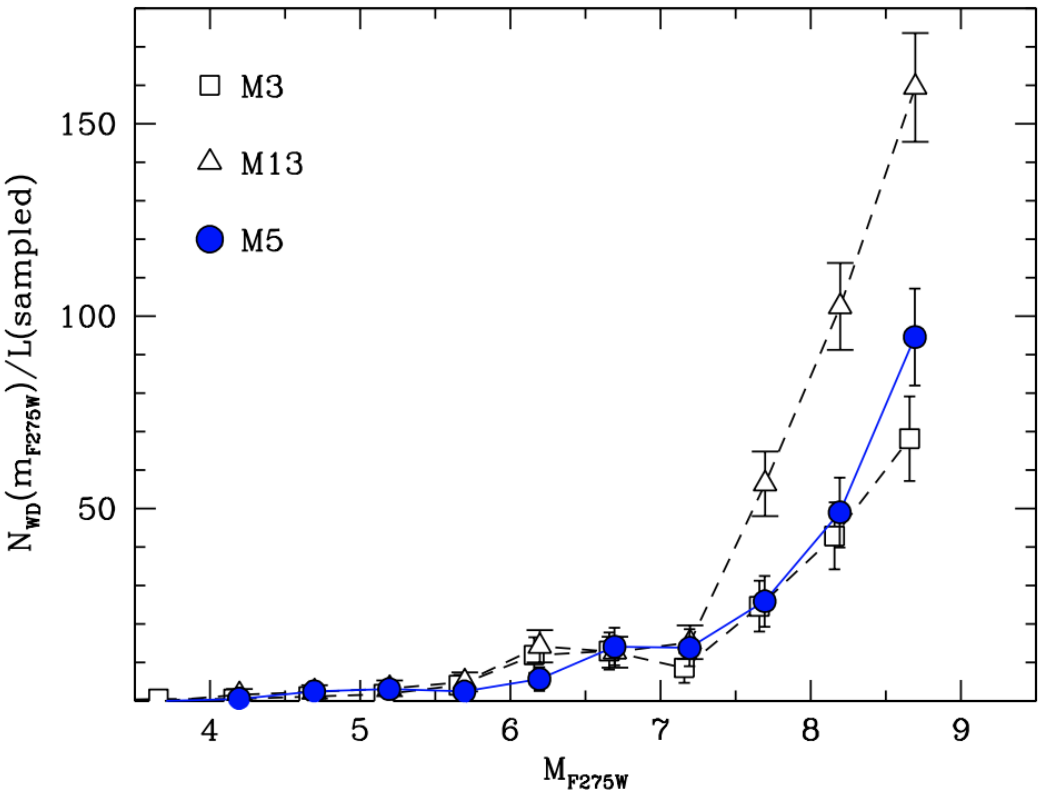

Figure 4.7: Completeness-corrected WD LFs of M5 (blue circles), M13 (empty triangles), M3 (empty squares) normalized to the sampled luminosity in units of $10^5 L_{\odot}$, as a function of the absolute $F275W$ magnitude.

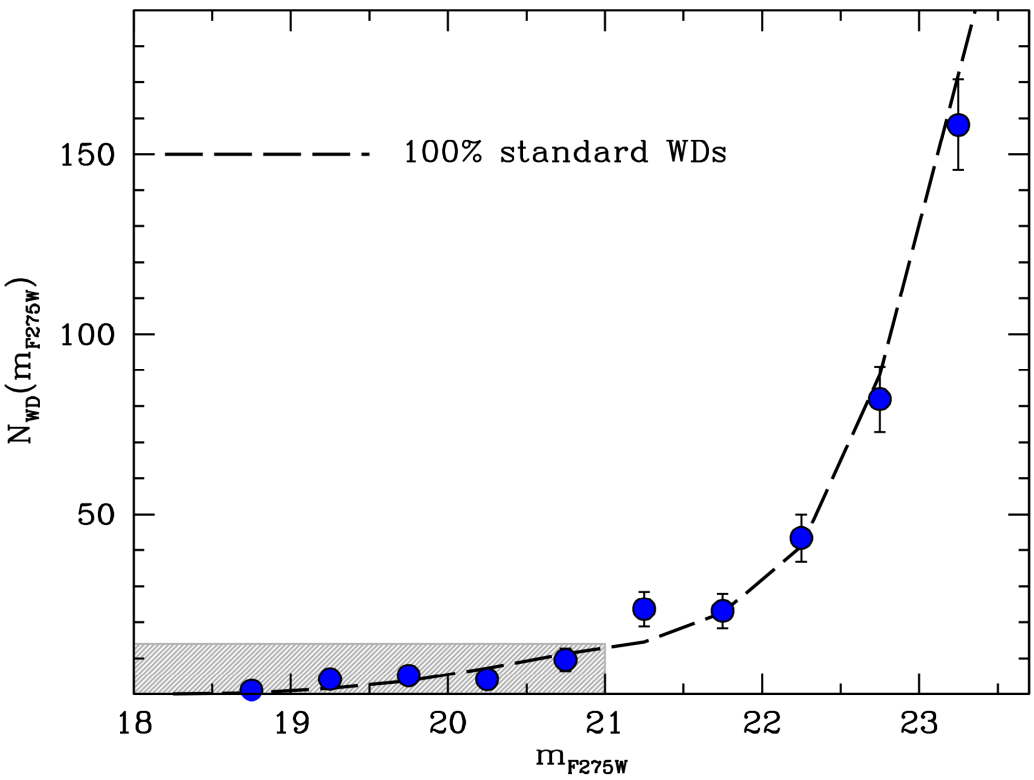

Figure 4.8: Completeness-corrected WD LF of M5 (blue circles), compared to the theoretical LF expected for a population of canonical (fast cooling) WDs (dashed line). The two LFs are normalized to the total number of WDs detected in the brightest portion of the cooling sequence ($m_{\rm F275W} < 21$), indicated by the grey shaded region.

4.4 Discussion and Conclusions

The scenario presented in Chen et al. (2021) (see also Chen et al. 2022) suggests the existence of a special class of "slowly cooling WDs", whose cooling rate is slowed down by some stable hydrogen burning in a very thin, but massive enough (of the order of $10^{-4}M_{\odot}$; Renedo et al. 2010) residual hydrogen-rich layer on the WD surface. The observational manifestation of these objects is an excess of WDs in the brightest portion of the LF, with respect to what observed in clusters where they are not present, and to what expected from models of "canonical" (fast cooling) WDs (e.g. M. Salaris et al., 2010) and Such an excess was indeed detected in M13 and NGC 6752, but not in M3.

A convincing picture of the physical origin of these objects must take into account that the mass of any residual hydrogen in proto-WDs is regulated by the occurrence or not of the third dredge-up during the AGB evolutionary phase Leandro G. Althaus et al. (2015). In fact, during the third dredge-up, convection carries carbon up to the stellar surface, while hydrogen is brought down inside the star, where it is burned. Thus, the occurrence of the AGB third dredge-up is expected to generate proto-WDs with very small hydrogen envelopes, where thermonuclear burning cannot take place: as a consequence, these stars generate canonical, totally exhausted WDs. Conversely, stars able to skip the third dredge-up reach the WD stage with a residual hydrogen envelope thick enough (with masses $> 10^{-4}M_{\odot}$) to allow stable thermonuclear burning, and this process provides the WD with an extra-energy production that delays its cooling process: slowly cooling WDs are thus generated. Chen et al. (2021) convincily demonstrated that the occurrence of this phenomenon is linked to the cluster HB morphology: significant populations of slowly cooling WDs are expected in GCs with well populated and extended blue HB morphologies. In fact, the presence of an extended HB blue tail indicates the existence of a significant fraction of stars with envelope mass so small that the subsequent AGB phase (hence, the third dredge-up) cannot occur. Thus, in M13 and NGC 6752 (both having blue tail HBs) $\sim$ 70% of the HB stars are expected to completely or partially skip the AGB, thus guaranteeing the survival of a significant residual hydrogen envelope and the consequent generation of slowly cooling WDs. Conversely, in M3 (where the HB morphology shows non extended blue tail) essentially all the HB stars are expected to evolve along the AGB, experience the third dredge-up, and thus produce canonical WDs.

From the analysis presented in this paper, the WD LF observed in M5 appears to be similar to that obtained by Chen et al. (2021) in M3. According to the scenario summarized above, the WD cooling sequence of M5 is thus expected to be essentially populated by

canonical WDs, whose progenitors all experienced the third dredge-up during the AGB phase. This is fully consistent with the expected mass distribution along the HB in the two clusters, which appears morphologically similar, with no extended blue tail (see Figure 4.2 and Dalessandro et al. 2013b for the HB mass function in M3).

To further corroborate this conclusion, we have compared the observed HB star distribution in both the UV and F606W-(F606W-F814W) optical CMDs of M5, with theoretical models from the BaSTI database (Pietrinferni et al., 2021). Specifically we used the $0.56 M_{\odot}$, α-enhanced HB tracks from Pietrinferni et al. (2006) at the cluster metallicity ([Fe/H]= -1.3) to identify the position of stars with this mass along the HB of M5. The adopted value marks approximately the lower limit of the HB masses that eventually go on experiencing the third dredge-up. To take into account the presence of a range of He abundances up to $\Delta Y \sim 0.04$ (see Milone et al. 2018), we employed tracks for both 'normal' ($Y = 0.248$) and enhanced ($Y = 0.30$) helium mass fractions. We found that only 10% (at most) of the HB stars have mass smaller than 0.56 $M_{\odot}$, thus confirming that basically all cluster WDs are expected to be canonically (fast) cooling objects.

Finally, we quantitatively tested this prediction by comparing the completeness-corrected WD LF of M5 (blue circles in Figure 4.8) with a theoretical WD LF computed in the case of 100% of canonical WDs (dashed line in the figure). The two LFs are normalized to the number of WDs detected in the brightest portion of the cooling sequence (at $m_{\rm F275W} < 21$: grey shaded region in the figure). As expected, the WD LF of M5 turns out to be in excellent agreement with the theoretical sequence, clearly demonstrating that the WD population in this cluster with no blue HB tail is entirely constituted by canonical objects.

The the results presented in this work therefore provide further solid support to the scenario traced in Chen et al. (2021, 2022) about the origin of slowly cooling WDs and their link with the HB morphology of the parent cluster. The extension of this investigation to clusters with extended HB blue tail in the extreme low metallicity regime ([Fe/H]= -2.2), where the phenomenon is expected to reach its maximum efficiency, is now urged to fully verify the theoretical predictions and provide an empirical measure of the impact of these results on the use of the WD cooling sequences as chronometers to measure cosmic ages.

Chapter 5

PSR J1641+3627F: A Low-mass He White Dwarf Orbiting a Possible High-mass Neutron Star in the Globular Cluster M13

Mainly based on Cadelano, Chen et al. 2020, ApJ, 905:63 (9pp)

5.1 Introduction

5.1.1 Millisecond Pulsars

Millisecond pulars (MSPs) are rapidly spinning Neutron Stars (NSs) usually formed in binary systems through mass-transfer from an evolving low-mass companion star ($\lesssim 1.4\ M_{\odot}$; Alpar et al., 1982; Bhattacharya et al., 1991; Lorimer et al., 2012). Active mass-transfer is commonly observed in binaries with a NS primary, generally considered as the precursors of MSPs (e.g. Archibald et al., 2010; F. R. Ferraro et al., 2015; Papitto et al., 2013; Stappers et al., 2014; T. M. Tauris et al., 2006). Following the mass-transfer phase, the NS is reactivated as a pulsar and it is usually observable in the radio bands, while the companion is expected to be the core-remnant of an exhausted and stripped evolved star: a white dwarf with a He core (He-WD; e.g. John Antoniadis et al., 2016a; M. Cadelano et al., 2019; Driebe et al., 1998;

Francesco R. Ferraro et al., 2003b; Istrate et al., 2014b; Thomas M. Tauris et al., 1999). Although this scenario has been firmly confirmed throughout the years, several deviations from it have been highlighted with the discovery, for example, of MSPs with massive CO-WD companions (e.g. Pallanca et al., 2013a; T. M. Tauris et al., 2011), double NS systems (e.g. Jacoby et al., 2006; Ridolfi et al., 2019; T. M. Tauris et al., 2017) or eclipsing MSPs with non-degenerate companion stars (e.g. Breton et al., 2013; M. Cadelano et al., 2015b; Mucciarelli et al., 2013; Pallanca et al., 2010; Roberts, 2013; Roberts et al., 2018).

5.1.2 Neutron Star Masses

The bulk of the NS population has masses around 1.4 $M_{\odot}$. However, recent studies on the NS mass function (John Antoniadis et al., 2016a) found evidence of a bi-modal distribution peaked at 1.4 $M_{\odot}$ and 1.8 $M_{\odot}$ and suggested a limiting sustainable NS mass of $\geq$ 2.018 $M_{\odot}$, before the stellar structure collapses to form a black-hole. NS mass measurements are driven by one of the most important and still unanswered question of modern physics: the behavior of cold matter at densities larger than that of nuclear saturation. Indeed, this regime is found in NS interiors, and constraining their still unknown equation of state therefore is one of the key ingredient to answer such a long-lasting unsolved question (e.g. Bogdanov et al., 2019; J. M. Lattimer et al., 2001; James M. Lattimer et al., 2007; Özel et al., 2016; Steiner et al., 2010). The increasing number of NS mass measurements and in particular the discovery of very high-mass NSs (John Antoniadis et al., 2013; Cromartie et al., 2020; Demorest et al., 2010; Fonseca et al., 2016) already helped to place constraints on the NS equation of state, leaving however a vast range of possibilities. (John Antoniadis et al., 2016b; Özel et al., 2016, and references therein).

5.1.3 Pulsars in globular clusters and their companions

While MSPs are ubiquitous throughout the whole Galaxy, their formation rate is enhanced by a factor of 10^3 in Globular Clusters (GCs). In fact, GCs are collisional systems where internal dynamics promote the formation of exotic systems like blue straggler stars, cataclysmic variables and MSPs (M. Cadelano et al., 2018; Campos et al., 2018; F. R. Ferraro et al., 2009, 2016; Hong et al., 2017; Rivera Sandoval et al., 2018), the latter sometimes in eccentric orbits with massive companions acquired by exchange encounters after the NS was already recycled (e.g. Ridolfi et al., 2019, and references therein). This makes GCs the ideal environment for studying exotic stellar systems, which can also be used as test particles

in modelling the complex interplay between cluster internal dynamics and stellar evolution (Cheng et al., 2019a,b; F. R. Ferraro et al., 2012, 2018, 2019). Moreover, they can provide a wealth of information about the physical properties of the host cluster itself (e.g. F. Abbate et al., 2018; Federico Abbate et al., 2019; P. C. C. Freire et al., 2017; Prager et al., 2017).

We are currently leading a long-term program aimed at identifying MSP companions in Galactic GCs. This program led to several discoveries and characterization of He-WD companions as well as non-degenerate and more exotic systems (M. Cadelano, 2019; M. Cadelano et al., 2015a,b, 2017a, 2019; Cocozza et al., 2008; Francesco R. Ferraro et al., 2001b, 2003b; Mucciarelli et al., 2013; Pallanca et al., 2010, 2013b, 2014), shedding light on binary and stellar evolution under extreme conditions. In this work, we report on the discovery of the companion star to the recently discovered PSR J1641+3627F (hereafter M13F) in the GC M13 (L. Wang et al., 2020).

M13 (NGC 6205) is a low-density cluster located at about 7 kpc from the Sun (Harris, 1996, 2010 edition) and affected by a very low stellar extinction $E(B-V) = 0.02$ (F. R. Ferraro et al., 1999). Its stellar population has an age around 13 Gyr (Dotter et al., 2010), an intermediate-low metallicity of $[Fe/H] = -1.5$ (Carretta et al., 2009a) and an extended blue horizontal branch (Francesco R. Ferraro et al., 1997). This cluster hosts six MSPs (Hessels et al., 2007; Kulkarni et al., 1991; L. Wang et al., 2020): two are isolated NSs, three are canonical systems likely having a WD companion and one is an eclipsing binary. M13F is one of the three canonical systems and was recently discovered with the FAST radio telescope by L. Wang et al. (2020). It has a spin period of 3 ms and an almost circular orbit of 1.4 days. The main properties of the system, useful for this work, are summarized in Table 5.1. The binary orbital parameters result in a NS mass function $f = 0.001108878\ M_{\odot}$. Such a value, assuming a typical NS mass of 1.4 $M_{\odot}$, implies an extremely low minimum companion mass (corresponding to an edge-on orbit) of 0.13 $M_{\odot}$ and a median companion mass (corresponding to an inclination angle of 60°) of 0.16 $M_{\odot}$. However, state-of-the-art binary evolution models (Istrate et al., 2014a,b, 2016) show that companion stars with intermediate-low metallicities (such that of stars in M13) are very unlikely to create a detached He-core WD less massive than $\sim 0.18\ M_{\odot}$ by the end of the mass-transfer and the binary detachment. This is mainly due to the fact that low-metallicity stars have shorter evolutionary timescales with respect to high-metallicity stars, and (having smaller radii) they are able to fill their Roche-Lobe at later stages of the binary evolution. This suggests that M13F could be a MSP with a non canonical companion star, i.e., a star different from a He-WD. Alternatively, it could be either a nearly face-on system, or a binary

Table 5.1: Main radio timing parameters for M13F[a], from L. Wang et al. (2020).

Parameter	Value
Right ascension, α (J2000)	$16^{\rm h}\,41^{\rm m}\,44^{\rm s}.6058(3)$
Declination, δ (J2000)	$36^\circ\,28'\,16''.0034(2)$
Angular offset from cluster center, $\theta_\perp$ (")	19.8
Spin period, P (ms)	3.003500835979(8)
Orbital period, P_b (days)	1.378005120(6)
Time of ascending node passage, T_{asc} (MJD)	58398.0011780(7)
Projected semi-major axis, x (s)	1.251702(3)
Eccentricity, e	$5(4)\times10^{-6}$
NS mass function, f ($M_\odot$)	0.001108878(8)

[a] Numbers in parentheses are uncertainties in the last digits quoted.

containing a NS more massive than 1.4 $M_\odot$ (in these cases, in fact, the companion mass would be larger than 0.18 $M_\odot$). All this motivates an investigation about the true nature and mass of the companion to M13F.

The paper is outlined as follows: in Section 5.2 the data-set and data reduction procedure are described; in Section 5.3 we present the identification of the companion star to M13F and we compare its properties with those predicted by binary evolution models. Finally, in Section 5.4 we draw our conclusions.

5.2 Data-set and Data Reduction

We used deep and high-resolution Hubble Space Telescope (HST) images obtained with the Wide Field Camera 3 (WFC3) and the Advanced Camera for Surveys (ACS) under GO 12605 (PI: Piotto), GO 10775 (PI: Sarajedini) and GO 10349 (PI: Lewin). The adopted data-set consists of a selection of images obtained with different filters covering a wavelengths range from near-UV to optical. The complete log of the observations is reported in Table 5.2.

The photometric analysis was performed using DAOPHOT IV (Stetson, 1987) and adopting the so-called "UV-route" described in S. Raso et al. 2017 (see also M. Cadelano et al. 2019). First of all, we selected $\sim$ 200 bright stars to model the point spread function of each image. These models were then applied to all the sources detected at more than 5σ from the background level. Then, we created a master list of stars with objects detected in at least half the F275W images. At the corresponding positions of these stars, the photometric fit was forced in all the other frames by using DAOPHOT/ALLFRAME (Stetson, 1994).

Table 5.2: Observations Log

Obs.ID	Camera	Filter	Exposures
G0 12605	WFC3/UVIS	F275W	6 x 427 s
		F336W	4 x 350 s
		F438W	4 x 46 s
GO 10775	ACS/WFC	F606W	1 x 7 s; 4 x 140 s
		F814W	1 x 7 s; 3 x 140 s
GO 10349	ACS/WFC	F435W	1 x 120 s; 2 x 680 s
		F625W	1 x 20 s; 4 x 90 s
		F658N	1x 120 s; 1 x 690 s; 1 x 800 s

By adopting such a near-UV master list, the crowding effects due to the presence of giants and turn-off stars are strongly mitigated and several blue stars like blue stragglers and white dwarfs are recovered. Finally, for each star we homogenized the magnitudes estimated in different images, and their weighted mean and standard deviation have been adopted as the star magnitude and its related photometric error. The instrumental magnitudes were calibrated to the VEGAMAG photometric system by cross-correlation with the publicly available catalogs of "*The Hubble Space Telescope UV Legacy Survey of Galactic globular clusters*" (Piotto et al., 2015), of the "*ACS Globular Cluster Survey*" (Sarajedini et al., 2007) or by using appropriate filter zero points and aperture corrections as described in Bohlin (2016).

The stellar detector positions were corrected for geometric distortion effects following the prescriptions by Meurer et al. (2003) and Bellini et al. (2011). Finally, the corrected positions were converted to the absolute coordinate system (α,δ) using the stars in common with the Gaia DR2 catalog (Gaia Collaboration et al., 2018). The coordinate system of this catalog is based on the International Celestial Reference System, which allows an accurate comparison with the MSP positions derived from timing using solar system ephemerids, since the latter are referenced to the same celestial system. The resulting combined 1σ astrometric uncertainty is $\lesssim 0.1''$.

5.3 The companion to M13F

5.3.1 Identification of the companion star

We searched for the optical counterparts to all the binary MSPs in the cluster by carefully analyzing all the stars located within a $1'' \times 1''$ region centered on the radio positions.

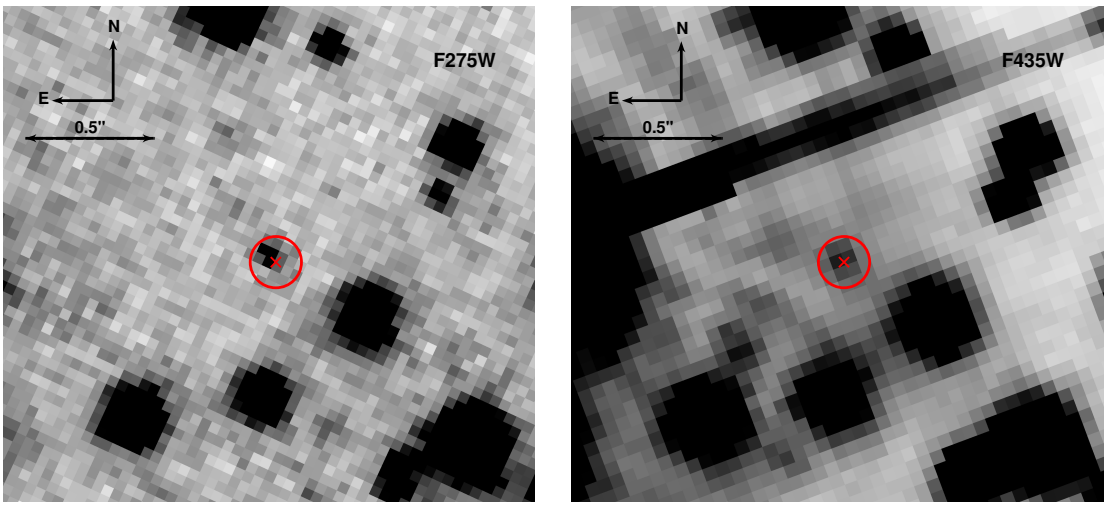

Figure 5.1: *Left Panel:* $2'' \times 2''$ region surrounding the position of M13F in a F275W image. The red cross is centered on the MSP position while the red circle has a radius of $0.1''$. The only star located within this circle is the identified companion to M13F. *Right Panel:* same as in the left panel, but for a F435W image.

For each of the candidate stars, we analyzed its position in the color-magnitude diagrams (CMDs) and investigated the presence of photometric variability, possibly associated to the binary orbital period. Unfortunately, no interesting candidates have been discovered at the positions of M13B, M13D and M13E. The detection of the counterparts to these systems was likely hampered by the presence of saturated or very bright stars close to their positions. On the other hand, we identified a promising candidate for the binary system M13F. In fact, at a distance of only 0.02" from the radio position, we discovered an extremely faint and blue star whose finding chart is reported in Figure 5.1. Despite its very low luminosity, this object is detectable in all the available filters, with the only exception of the F658N one. Its magnitudes and 1σ uncertainties are: $m_{F275W} = 23.65 \pm 0.10$, $m_{F336W} = 23.9 \pm 0.1$, $m_{F438W} = 24.2 \pm 0.2$, $m_{F435W} = 24.20 \pm 0.02$, $m_{F606W} = 24.35 \pm 0.07$, $m_{F625W} = 24.1 \pm 0.1$ and $m_{F814W} = 24.2 \pm 0.1$, while for the F658N filter we derived a lower limit of $m_{F658N} > 24.2$. As shown in Figure 5.2, these magnitudes place the candidate companion star along the red side of the WD cooling sequence, in a region compatible with the expected location of WDs with a He core. The excellent agreement between the radio and optical positions and its peculiar location in the CMDs allow us to safely conclude that the detected object is the companion star to M13F.

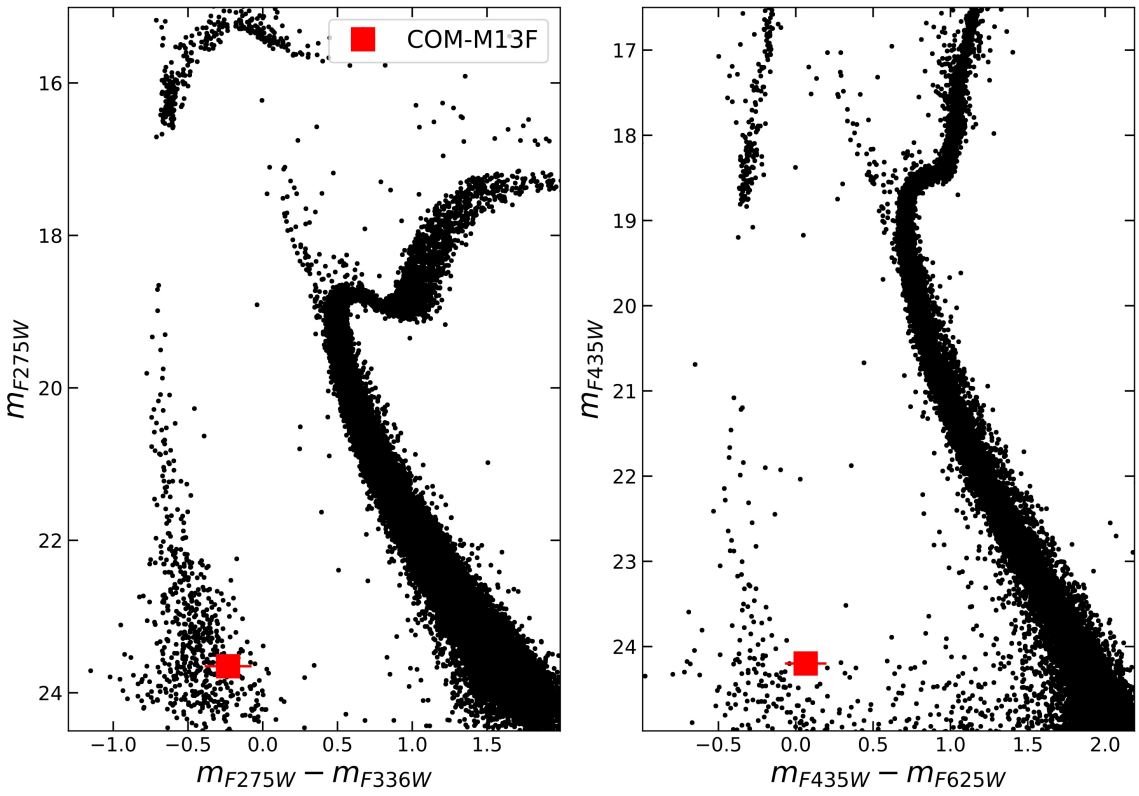

Figure 5.2: *Left panel:* (m_{F275W}, $m_{F275W} - m_{F336W}$) near-UV CMD of M13. *Right panel:* (m_{F435W}, $m_{F435W} - m_{F625W}$) optical CMD of M13. In both panels, the position of the companion star to M13F is highlighted with a red square and the error bars correspond to the 1σ confidence level uncertainties.

5.3.2 Comparison with binary evolution models

In the previous section we confirmed that M13F is orbiting a WD. In order to get insights on the properties of the companion star, it is useful to compare its observed magnitudes with binary evolution models. First, in order to properly compare the observed and theoretical frames, we checked the accuracy of the photometric calibration by comparing the observed cluster sequences in the CMDs, such as the main sequence and the CO-WD sequence, with isochrones and CO-WD cooling tracks. We generated from the *BaSTI* database (Pietrinferni et al., 2004, 2006; M. Salaris et al., 2010) an isochrone reproducing a 13 Gyr old stellar population (Dotter et al., 2010) with a metallicity $[Fe/H] = -1.62$ and $[\alpha/Fe] = 0.2$, together with a cooling track for a CO-WD with a canonical mass $M = 0.55\ M_{\odot}$. Absolute magnitudes were converted to be observed frame by adopting a distance modulus $(m-M)_0 = 14.43$, a color excess $E(B-V) = 0.02$ (Dotter et al., 2010; F. R. Ferraro et al., 1999) and appropriate extinction coefficients calculated following the prescriptions by Cardelli et al. (1989) and O'Donnell (1994). The two curves are shown in Figure 5.3. The excellent agreement between the models and the observed sequences confirms the accuracy of the photometric calibration and of the adopted cluster parameters. Moreover, the position of the companion to M13F with respect to the CO-WD cooling track also suggests that it is likely a WD with a He core, as expected from the canonical formation scenario of MSPs.

To derive the companion properties, we computed binary evolutionary models using the open source stellar evolution code MESA(Paxton et al., 2011, 2013, 2015, 2018), version 12115, in a similar fashion to Istrate et al. (2014b, 2016). The initial binary parameters consist of a 1.4 $M_{\odot}$ NS, treated as point mass, and a 1.1 $M_{\odot}$ donor star with a metallicity of $Z = 0.0005$, compatible with that of the cluster. The new evolutionary models will be soon publicly available (Istrate et al. 2020, in prep). The resulting tracks span a He-WD mass range of 0.18 $M_{\odot}$ − 0.4 $M_{\odot}$, a surface temperature range of 6000 K − 21000 K and cooling ages[1] up to the cluster age. Theoretical bolometric luminosities were transformed to HST magnitudes by using the Astrolib PySynphot package (STScI Development Team, 2013)[2] and WD spectra templates by Koester (2010)(see also Tassoul et al., 1990; Tremblay et al., 2009). A selection of these evolutionary tracks is shown in Figure 5.3, where we can qualitatively infer that the track better reproducing the companion CMD positions is the one corresponding to a mass of 0.23 $M_{\odot}$.

[1]The WD cooling age is defined, according to Istrate et al. (2016), as the time passed since the proto-WD reached the maximum surface temperature along the evolutionary track.

[2]https://pysynphot.readthedocs.io/en/latest/

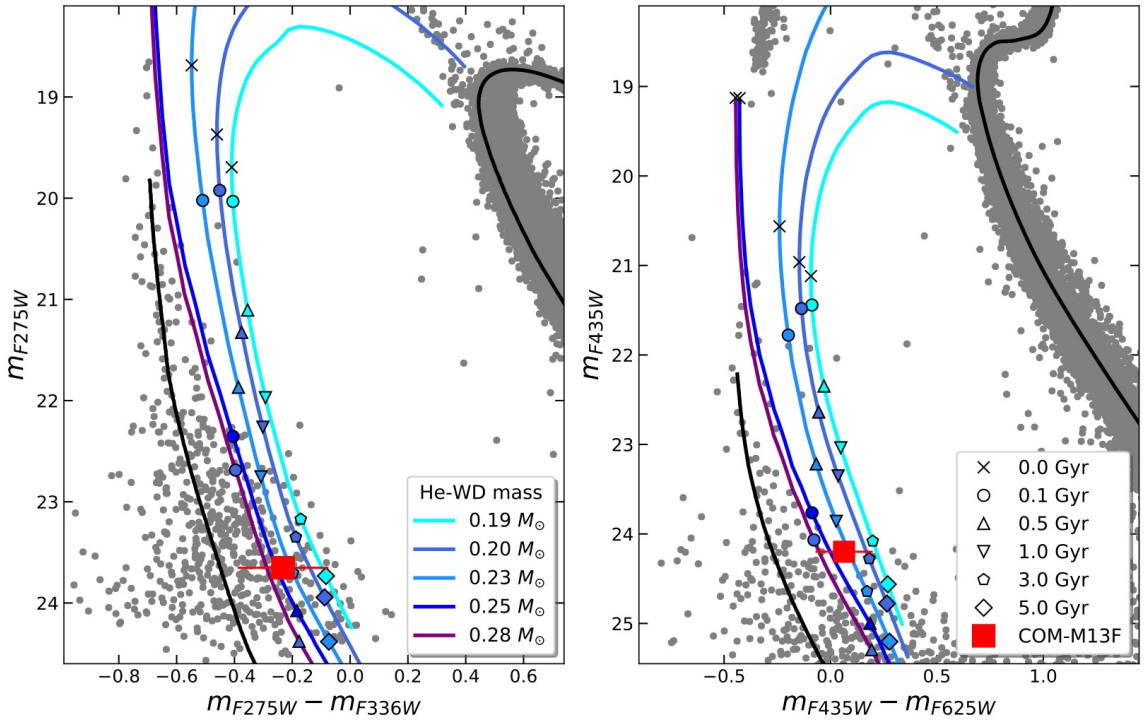

Figure 5.3: Same as in Figure 5.2 but zoomed on the WD region. The black curves are an isochrone reproducing a 13 Gyr old stellar population and a cooling track for a CO-WD with a mass of 0.55 $M_\odot$. The other curves are He-WD tracks with masses, from left to right, of 0.28 $M_\odot$, 0.25 $M_\odot$, 0.23 $M_\odot$, 0.20 $M_\odot$ and 0.19 $M_\odot$ computed similarly as in Istrate et al. (2014b, 2016). Points at different cooling ages are highlighted with different symbols as reported in the right panel legend.

Table 5.3: Derived properties of the companion to M13F

Parameter	Value
M_{COM} ($M_\odot$)	0.23 ± 0.03
$\log g$ (cm/s^2)	6.8 ± 0.2
R_{COM} ($R_\odot$)	$0.033^{+0.004}_{-0.005}$
T_{eff} (K)	11500^{+1900}_{-1300}
Cooling Age (Gyr)	3 ± 1 or 0.2 ± 0.1
Proto-WD Age (Myr)	200^{+400}_{-100}

From top to bottom: companion mass, surface gravity, radius, surface temperature, cooling age and proto-WD age.

In order to get a quantitative derivation of the companion physical properties (such as its mass, radius, age, surface gravity and temperature) we implemented an approach similar to that described in M. Cadelano (2019). We defined a logarithmic likelihood $\mathscr{L}$ to quantify the probability of each point of each evolutionary track to reproduce the observed companion magnitudes, as follows:

$$\ln \mathscr{L} = -\frac{1}{2} \sum_f \frac{(m_f - \tilde{m}_f)^2}{\delta_f^2} + \ln(2\pi\delta_f^2) \tag{5.1}$$

where the index f runs through all the available filters, m_f and $\tilde{m}_f$ are the observed and the model magnitudes in a given filter f, respectively, and δ_f is the uncertainty on the observed magnitude. The latter term also takes into account a 0.1 mag uncertainty on the cluster distance modulus and a 0.01 mag uncertainty on the cluster color excess. The likelihood $\mathscr{L}$ was also forced to zero wherever the predicted F658N magnitude was smaller than the lower limit derived in the previous section. The resulting likelihood-weighted 1D and 2D histograms are presented in the corner plot[3] of Figure 5.4. For each of the WD parameters, we derived the best values and related uncertainties as the 0.16, 0.5 and 0.84 quantiles of the distributions. All these results are also listed in Table 5.3.

Results show that the companion to M13F is indeed a low-mass He-WD with a mass around 0.23 $M_\odot$. As it can be seen in Figure 5.4, all the companion parameters have been firmly constrained with the exception of the cooling age. Indeed, the 1D histogram of the cooling ages show a clear bi-modal distribution. This feature is the result of a dichotomy in the cooling timescales due to the occurrence of diffusion induced hydrogen shell flashes in

[3] https://corner.readthedocs.io/en/latest/ (Foreman-Mackey, 2016)

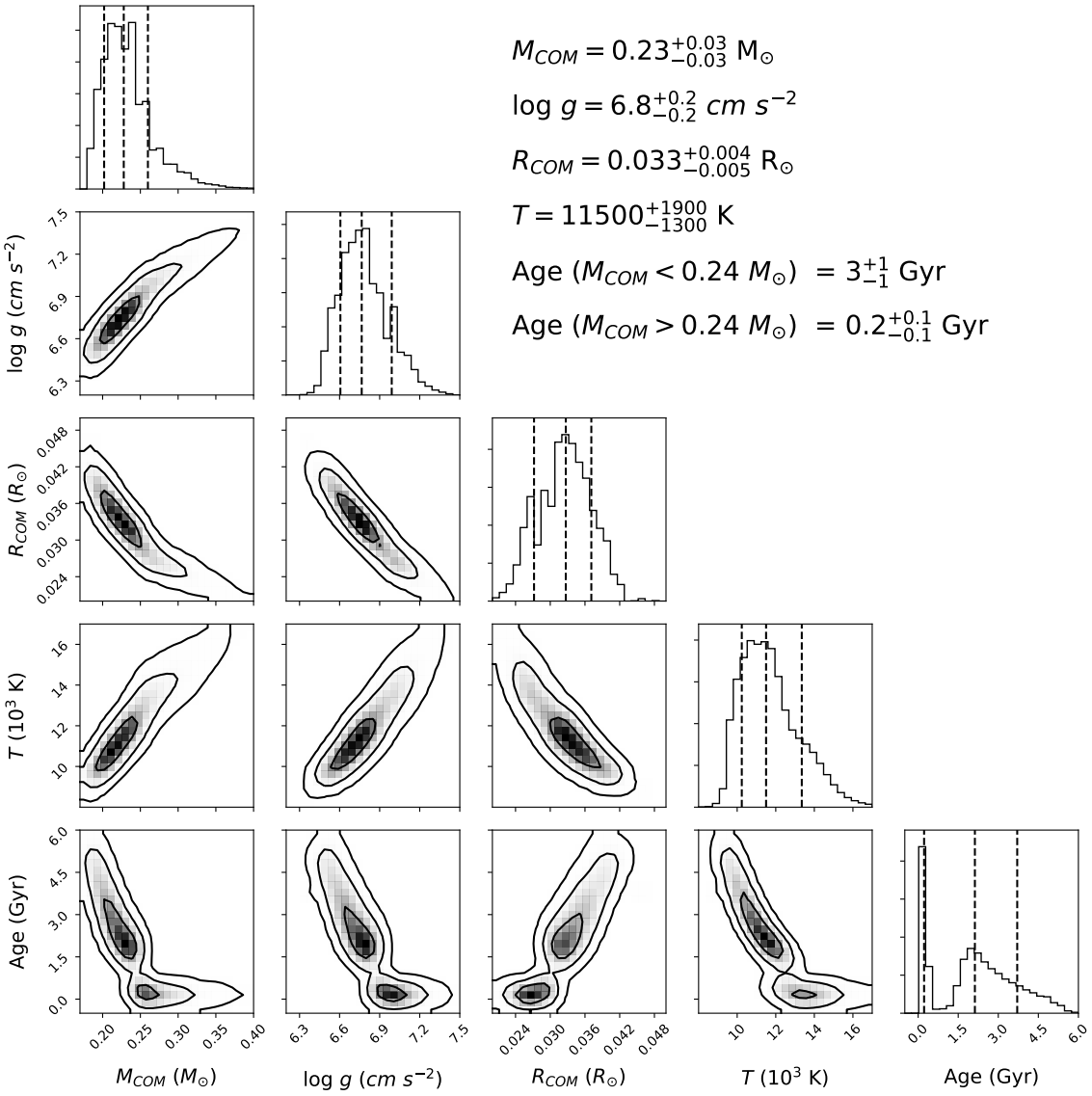

Figure 5.4: Constraints on the mass, surface gravity, radius, surface temperature and cooling age of the companion star to M13F. The 1D histograms show the likelihood weighted distributions for each of the parameters. The three vertical dashed lines for each 1D histogram correspond, from left to right, to the 0.16, 0.5, and 0.84 quantiles, respectively. The contours in the 2D histograms correspond to 1σ, 2σ and 3σ levels. The text at the top reports the derived values for each parameter.

the envelope of proto-WD with mass $M \gtrsim M_{\rm flash} \sim 0.2\ M_{\odot}$[4]. The systems which experience such flashes will enter the cooling tracks with a thin hydrogen envelope. The WDs with $M < M_{\rm flash}$ experience stable hydrogen shell burning during the proto-WD and enter the cooling track with a thick hydrogen envelope. As the cooling timescale depends primarily on the mass of the hydrogen envelope, a cooling dichotomy will be observed (see e.g. L. G. Althaus et al., 2001a,b; Istrate et al., 2014b, 2016). This dichotomy clearly applies to our results. Indeed, our models predict that the minimum mass for the flashes to occur at the cluster metallicity is around 0.24 $M_{\odot}$. A closer inspection to the 1D and 2D likelihood distributions of the cooling ages (Figure 5.4) reveals a prominent narrow peak centered around 0.3 Gyr and a long tail extending up to $\sim$ 5 Gyr. The narrow peak is associated with masses larger than 0.24 $M_{\odot}$, which experience hydrogen flashes (fast cooling), while the tail is associated with masses lower than 0.24 $M_{\odot}$, which burns hydrogen stably (slow cooling). All this hampers a proper determination of the system age and we therefore report both the cooling ages in the figure and in Table 5.3. Selecting only the narrow peak of the age likelihood distribution, the corresponding companion mass is $0.26^{+0.04}_{-0.01}\ M_{\odot}$. On the other hand, the extended tail of the age likelihood distribution implies a mass of $0.22 \pm 0.02\ M_{\odot}$. Unfortunately, not even the pulsar spin-down age can be used to better constrain the system age, since its value has been proven to be highly unreliable (e.g. T. M. Tauris et al., 2012; Thomas M. Tauris, 2012) and also depends on the intrinsic pulsar spin-down rate, which cannot be easily determined for MSPs in GCs due to the contamination by the acceleration induced by the cluster potential (e.g. Prager et al., 2017).

Although the data-set is composed of several multi-epoch images, we found no evidence of photometric variability. While this could be due to the very poor and random orbital period coverage provided by the available data-set, we stress that He WD companions only rarely show variability, which is usually due to pulsations (global stellar oscillations) of the WD itself (e.g. John Antoniadis et al., 2016a; M. Kilic et al., 2015; Maxted et al., 2013; Parsons et al., 2020). Indeed, heating of the stellar side exposed to the MSP and/or tidal distortions due to the NS tidal field are negligible , at odds with the case of non-degenerate and tidally-locked companions stars (e.g. M. Cadelano et al., 2015b; Pallanca et al., 2010, 2014), although exceptions exist (e.g. Edmonds et al., 2001; Kaplan et al., 2012).

The companion mass here derived is based on the comparison between the WD observed and predicted optical magnitudes and thus does not take into account the orbital properties

[4]Please note that this critical value strongly depends on the metallicity and physics of diffusion (Istrate et al., 2016)

of the system derived through radio timing. However, for He-WDs formed through the stable mass-transfer channel, there is a very well known and tight correlation between the binary orbital period and the mass of the proto-WD at the epoch of binary detachment (e.g. Istrate et al., 2014b; Joss et al., 1987; Lin et al., 2011; Rappaport et al., 1995; Savonije, 1987; Thomas M. Tauris et al., 1999). Such a correlation, which mainly depends on the companion star metallicity and, to a lesser extent, on other stellar parameters (e.g. mixing length parameter, initial companion mass), has been also confirmed through observations (e.g. Corongiu et al., 2012). The theoretical mass-period relation for various metallicities is shown in Figure 5.5. One should note that compared to field stars, GC exhibit helium and α elements enhancement which were ignored in this work, but might influence the mass-period relation at a given metallicity. These effects will be studied in a future work. At the orbital period of M13F and cluster metallicity ($Z \approx 0.0005$), the predicted mass for the forming He-WD is $\sim 0.21\ M_{\odot}$, in agreement with our results. Here it is assumed that the WD did not lose a significant amount of mass during the proto-WD stage and that the current orbital period is almost unchanged with respect to that at the epoch of the binary detachment.

5.3.3 Constraints on the NS mass

The determination of the companion mass together with the binary orbital parameters derived through the radio timing analysis allows us to place constraints on the NS mass. In fact, the masses of the binary components can be expressed as a function of the orbital parameters through the NS mass function:

$$\frac{(M_{COM} \sin i)^3}{(M_{NS} + M_{COM})^2} = \frac{4\pi^2 x^3}{G P_{ORB}^2} \tag{5.2}$$

where M_{COM} and M_{NS} are the companion and the NS mass, respectively, i is the orbital inclination angle, G the gravitational constant, x the projected semi-major axis and P_{ORB} the orbital period. The right-hand side of this equation depends exclusively on the binary orbital parameters (see Table 5.1) and thus its value is very well constrained: $f = 0.001108878 \pm 0.000000008\ M_{\odot}$. On the other hand, the left-hand side of the equation contains the measured companion mass and two completely unknown quantities: the NS mass and the orbital inclination angle. Figure 5.6 shows the NS mass predicted by equation 5.2 as a function of both the companion mass and the orbital inclination angle. We find that a $0.23 \pm 0.03\ M_{\odot}$ companion star could in principle imply the presence of a very massive NS.

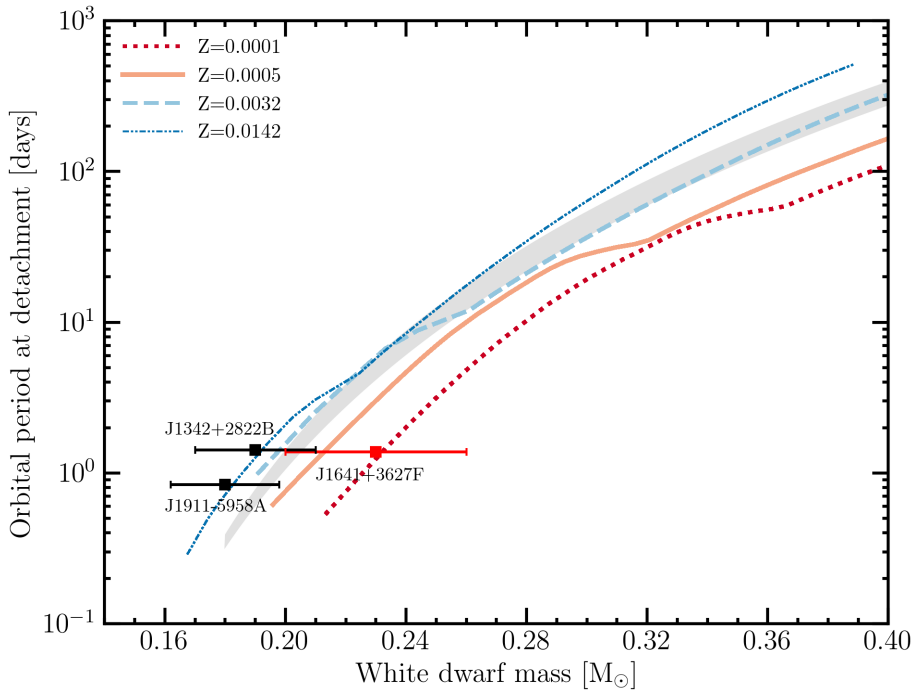

Figure 5.5: Orbital period at the end of the mass-transfer phase versus the mass of the proto-WD. The various lines represent theoretical mass-period relations for Z=0.0001, Z=0.0005, Z=0.0032 and Z=0.0142 as predicted by binary evolution models (Istrate et. al in prep.). The grey region represents the fitted mass-period relation by Thomas M. Tauris et al. (1999). The orange solid line at Z=0.0005 is representative for the metallicity of M13. The red square reports the position of the companion to M13F. We also included the positions of the companions to J1342+2822B in M3 (M. Cadelano et al., 2019) and J1911−5958A in NGC6752 (Corongiu et al., 2012), since the two clusters share approximately the same metallicity of M13.

In fact, Figure 5.6 reveals that if M13F is observed almost edge-on ($i \gtrsim 70°$), than the NS mass should be $\gtrsim 2.4\ M_\odot$. More precisely, the maximum NS mass, corresponding to $i = 90°$ is $M_{NS,max} = 3.1 \pm 0.6\ M_\odot$. Such value is larger than ever measured for any massive NS and larger than the maximum sustainable mass predicted by most of the theoretical equations of state (e.g. Özel et al., 2016). Therefore, it is unlikely that this system is observed at very large inclination angle. On the other hand, assuming that binaries are randomly inclined with respect to the observer, i.e. assuming a flat distribution of $\cos i$, we find a median NS mass (corresponding to $i = 60°$) of $M_{NS,med} = 2.4 \pm 0.5\ M_\odot$ (see right panel of Figure 5.6). Such value would place M13F on the highest-mass side of the known NS mass distribution (e.g. John Antoniadis et al., 2016b; Cromartie et al., 2020). All this suggests that either M13F is observed at quite small inclination angles ($i \lesssim 40°$) or it hosts a massive NS. Indeed, under the assumption of a flat distribution of $\cos i$, there is a $\sim 70\%$ of probability that the compact object mass is larger than $1.6\ M_\odot$, thus favoring the case of a massive NS. Finally, we further investigate the possibility of having a standard NS mass coupled with a low inclination angle. To this aim, we used a Monte Carlo Markov Chain sampler (Foreman-Mackey et al., 2019) to explore the combination of NS masses and orbital inclination angles able to reproduce the observed mass-function. We defined a standard Gaussian likelihood function to minimize the difference between the left and right side of equation 5.2. We assumed an uniform prior on the distribution of $\cos i$ and also a prior on the NS mass distribution following that empirically derived by John Antoniadis et al. (2016b), which is roughly a double Gaussian with a main component centered at $1.4\ M_\odot$ and with a dispersion of about $0.1\ M_\odot$, and a secondary component centered at $1.8\ M_\odot$ and with a dispersion of about $0.2\ M_\odot$. The posterior distribution is shown in Figure 5.7 and the results based on the 16^{th},50^{th},84^{th} percentiles show that M13F could host a NS with an almost standard mass of $1.5 \pm 0.1\ M_\odot$ if orbiting with an inclination angle $i = 43^{+15}_{-6}$ degrees.

5.4 Conclusions

PSR J1641+3627F is a binary MSP recently discovered in the GC M13 by observations with the FAST radio-telescope (L. Wang et al., 2020). Its timing analysis revealed a 1.4 day circular orbit and a NS mass function implying a minimum and median companion mass of only $0.13\ M_\odot$ and $0.16\ M_\odot$, respectively, under the assumption of a NS having with a standard mass of $1.4\ M_\odot$. However, state-of-the-art binary evolution models suggest that such low-mass companions are unlikely to be produced in a intermediate-low metallicity

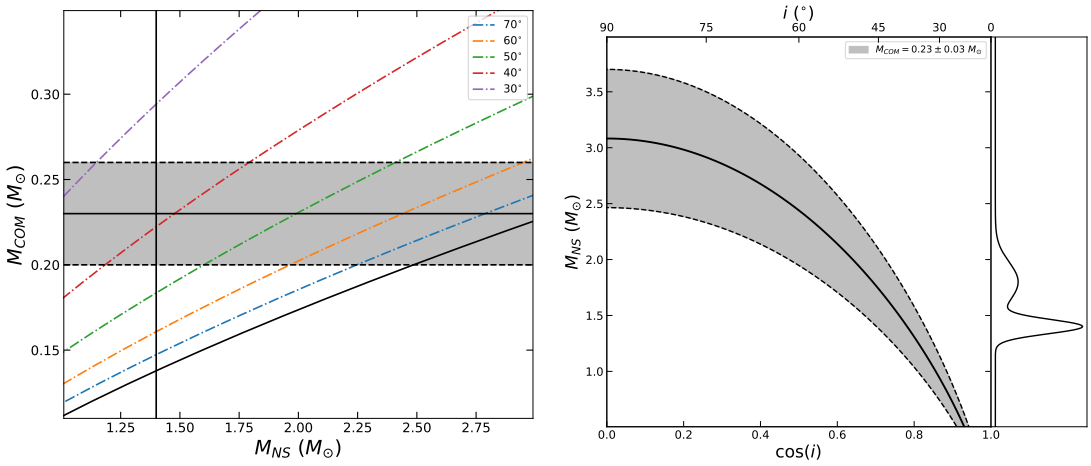

Figure 5.6: *Left panel:* companion mass as a function of the NS mass. The solid horizontal line marks the best-fit value of the companion mass ($M = 0.23\ M_\odot$) and the light-grey region delimited by the two horizontal dashed lines marks its estimated uncertainty. The dark gray shaded area is the region forbidden by the binary mass function (see equation 5.2), while the dot-dashed colored lines are the curve obtained assuming different inclination angles. The vertical line represents a canonical NS mass of 1.4 $M_\odot$. *Right panel:* NS mass as a function of the cosine of the orbital inclination angle, for the estimated mass of the companion star: the solid curve marks the combination of values allowed by the best-fit value of the companion mass (0.23 $M_\odot$), while the light-grey region delimited by the two dashed curves marks the combinations allowed within the uncertainty (see the legend). The right edge panel shows, as reference, the NS mass distribution empirically derived by John Antoniadis et al. (2016b).

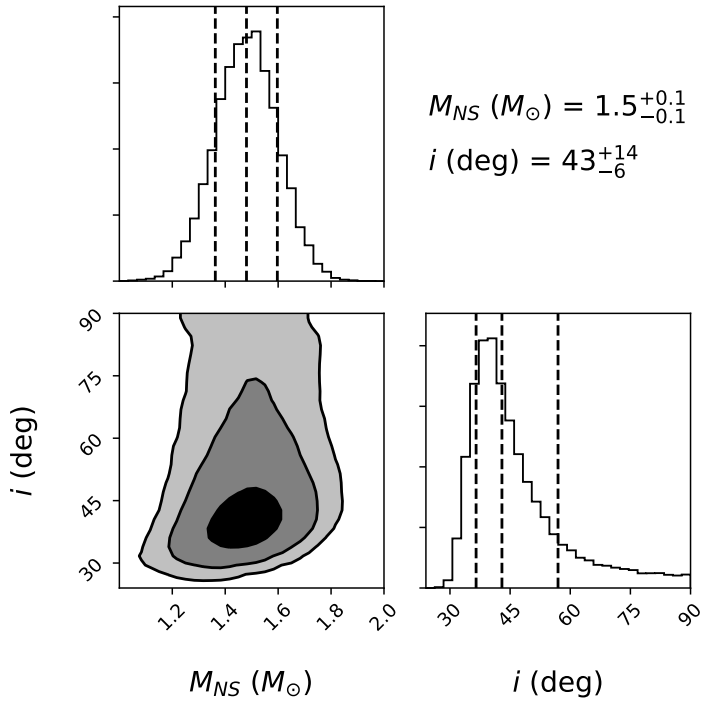

Figure 5.7: Corner plots showing the 1D and 2D projections of the posterior probability distribution of the NS mass and inclination angle of M13F. The 1D-histograms are the marginalized probability distributions and the dashed lines corresponds to their 16^{th},50^{th},84^{th} percentiles. The bottom left panel is the joint 2D posterior probability distribution and the contours corresponds to 1σ, 2σ and 3σ confidence levels.

cluster such as M13. This is mainly due to the fact that lower metallicity stars are more compact for the same He-core mass compared to higher metallicities (Istrate et al., 2016). This suggests that M13F could host a non-canonical companion or, alternatively, that the system is observed at nearly face-on orbits or that it hosts a high-mass NS. To shed light on this, we used a combination of near-UV and optical observations obtained with HST to identify the companion star. At a distance of only 0.02" from the radio MSP position, we identified a faint and blue object located on the red side of the CMD region occupied by the cluster WD cooling sequences and thus compatible with the expected position of He-WDs. Our study therefore allowed us to exclude the first possibility and conclude that the companion to M13F is a canonical He-WD. We exploited the HST multi-band photometry also to constrain the companion properties from the comparison with binary evolutionary models computed for M13 metallicity following the prescriptions in Istrate et al. (2016). We found that the companion to M13F likely has a mass $M_{COM} = 0.23 \pm 0.03\ M_{\odot}$. It is important to stress that this value is model-dependent, but different assumptions about the binary and stellar evolution physics are expected to lead to only slightly different results.

Although our analysis does not allow to break the degeneracy between the inclination angle and the NS mass, we could at least reduce the range of possibilities by combining the derived companion mass with the binary orbital parameters. We find a maximum NS mass (corresponding to an edge-on orbit, $i = 90°$) of $M_{NS,max} = 3.1 \pm 0.6\ M_{\odot}$ and a median NS mass (corresponding to $i = 60°$) of $M_{NS,med} = 2.4 \pm 0.05\ M_{\odot}$. These high values suggest that M13F is unlikely to be observed edge-on. Therefore we conclude that either M13F hosts a canonical NS with a mass $\sim 1.4\ M_{\odot}$ and is observed at nearly face-on inclination angles around 40° or its NS is part of the growing class of high-mass NSs.

To break the degeneracy between a face-on orbit and a high-mass NS, independent measurements of the companion mass and possibly of the orbital inclination are needed. These quantities could in principle be constrained, for example, through the radio detection of a Shapiro delay (e.g. Corongiu et al., 2012; Cromartie et al., 2020), in particular its orthometric amplitude parameter h_3 (see Paulo C. C. Freire et al., 2010). However, given the extreme faintness of M13F, even in FAST data, it is unlikely that such a detection can be made in the near future. Alternatively, the mass ratio between the two binary component could be measured through spectroscopic observations that however, due to the companion low-luminosity, are beyond the capabilities of the current generation of optical telescopes.

Unfortunately, the wavelength coverage and sampling of our observations is not enough to perform a reliable SED fitting of the observed magnitudes with WD spectral templates.

Although this technique could be useful to obtain an independent companion mass measurement, additional observations at UV wavelengths ($\lambda < 2700$ Å) are necessary to properly constrain the surface gravity and radius of a WD by using this method. However, multi-band and high quality observations sampling the whole wavelength range from UV to optical are indeed feasible and could confirm in the future the companion mass here derived.

Chapter 6

A young white dwarf orbiting PSR J1835-3259B in the bulge globular cluster NGC 6652

Mainly based on Chen et al. 2023, ApJ, accepted

6.1 Introduction

We are leading a long-term program aimed at identifying MSP in GCs through near-UV to near-IR photometric and spectroscopic observations of their companion stars with the aim of obtaining a complementary view of the binary properties and study their formation and evolution in the ideal GC laboratory. This program led to the discovery and characterization of several He-core WD companions (M. Cadelano et al., 2015a, 2019; Francesco R. Ferraro et al., 2003b)), one of them possibly orbiting a high-mass NS (Mario Cadelano et al., 2020), and several companions to spider MSPs (M. Cadelano et al., 2015b, 2017b; Cocozza et al., 2006; Francesco R. Ferraro et al., 2001b; Mucciarelli et al., 2013; Pallanca et al., 2010, 2013b, 2014; Sabbi et al., 2003a,b).

Here we report on the identification and characterization of the companion star to NGC 6652B based on high-resolution near-ultraviolet and optical observations obtained from the Hubble Space Telescope (HST).

Table 6.1: Observation Log of the data set.

obs. ID	F275W	F336W	F438W
	690s×2	305s×2	60s×1
GO-13297	775s×2	313s×1	69s×1
	800s×2	313s×3	86s×1

NGC 6652 is a GC located around 10 kpc from the Sun (Harris, 1996, 2010 edition), with an age of 13.25±0.5 Gyr (Dotter et al., 2010), an intermediate metallicity of [Fe/H] ≈ -0.75 and a small extinction of E(B-V) = 0.09 (Harris, 1996)(2010 edition) for a stellar system located in the Galactic bulge. PSR J1835−3259A was the first binary MSP discovered in the cluster by DeCesar et al. (2015) and it is characterized by a pulse period of 3.89 ms, an orbital period of 9.25 days and a very high eccentricity $e = 0.97$. The MSP is orbiting a companion with a minimum mass of about 0.7 $M_{\odot}$, which could be either a massive white dwarf or a secondary NS. This system likely formed through an exchange encounter in the dense cluster environment. Recently, a new binary MSP, namely J1835−3259B (hereafter NGC 6652B) has been discovered by Gautam et al. (2022). The NS is spinning at 1.83 ms and is located in a 1.2 days long orbit with an extremely small eccentricity of about 3×10^{-5}. Zhang et al. (2022) used observations obtained by the Fermi Gamma-ray Space Telescope and detected a high-energy emission of the MSP as a source with a γ-ray luminosity of 5×10^{34} erg s^{-1}.

This paper is organized as follows: in Section 6.2, we describe the data set and data reduction; the identification and characterization of the companion star are presented in section 6.3 and the conclusions are finally drawn in section 6.4.

6.2 Data Reduction

In this work, we used high-resolution and deep photometric data acquired with the HST in the near-ultraviolet band, captured by the UVIS channel of the Wide Field Camera 3 (WFC3), the obtained archival data set is a part of the HST legacy survey of galactic globular clusters under GO-13297 (PI: Piotto). There are 3 different filters used: F275W(near-UV), F336W(U), and F438W(B), the observational log of the data set is listed in Table 6.1.

The data reduction was performed on the calibrated images with extension $\_flc$ (UVIS calibrated exposure including Charge Transfer Efficiency (CTE)), after pre-reduction including Pixel Area Map correction.

In searching for the optical companion to PSR J1835−3259A and PSR J1835−3259B

we adopted the so-called "UV-route", a photometric procedure specifically optimized for the identification of blue and hot objects in crowded fields such as hot Horizontal Branch stars, BSSs and WDs and widely used by our group in previous papers (see Dalessandro et al. 2013b; F. R. Ferraro et al. 1993, 1997; Francesco R. Ferraro et al. 1997, 2001a, 2003b). Specifically, in this paper we followed the approach described in M. Cadelano et al. (2019) and Mario Cadelano et al. (2020) (see also Chen et al. 2021, 2022; S. Raso et al. 2017; Silvia Raso et al. 2020).

As the first step, about 250 bright and unsaturated stars were selected to model the Point Spread Function (PSF) for each image, then the resulting models were applied to all the sources detected above 4 σ from the background. As a second step, we created a "*master list*" of stars containing all the sources detected in at least half the F275W images. The PSF-fitting of all the sources in the master-list was forced at the corresponding positions in all the frames using DAOPHOT/ALLFRAME (Stetson, 1994). Finally, magnitudes obtained for different stars were averaged and homogenized using DAOPHOT/DAOMASTER.

The instrumental magnitudes were calibrated to the VEGAMAG system by using appropriate zero-points and aperture corrections[1]. After correction for geometric distortions (Bellini et al., 2011), the coordinates were aligned to the International Celestial Reference System by cross-correlation with the Gaia DR3 Catalog (Gaia Collaboration et al., 2022), To this aim, we used the cross-correlation software CataXcorr[2] adopting a six parameter linear transformation to convert the instrumental (x, y) positions to the (RA, Dec) absolute coordinate system. The transformation residuals returned a combined astrometric uncertainty of about 14 mas.

6.3 The companion to NGC 6652B

6.3.1 Identification of the companion star

To identify the optical counterpart of the MSP in the cluster, we carefully analyzed all the stars in the region surrounding the two MSP positions. No stars are found at a position compatible with PSR J1835−3259A. On the other hand, a peculiar bright and blue star is found at 30 mas from timing position of NGC6652B. The resulting 1σ radio timing and optical uncertainty for this MSP is 17 mas (see Section 6.2 and Table 3 in Gautam et al.

[1] https://www.stsci.edu/hst/instrumentation/wfc3/data-analysis/photometric-calibration
[2] http://davide2.bo.astro.it/~paolo/Main/CataPack.html

(2022)), therefore the two positions of the two sources turn out to be compatible within 1.8σ. Figure 6.1 shows the finding chart in the three different adopted filters. It can be easily appreciate that the source closest to NGC6652B is a very blue star as its luminosity rapidly decreases in redder filters. Nonetheless, the candidate is bright enough to be detected in all the three filters with small uncertainties: $m_{F275W} = 21.77 \pm 0.02$, $m_{F336W} = 21.93 \pm 0.04$, and $m_{F438W} = 22.62 \pm 0.07$. Observations in the F606W and F814W filters are available in the HST archive but we did not include them in the analysis since the companion is not detectable due to nearby heavily saturated star.

Figure 6.2 shows the Color Magnitude Diagram (CMD) of the cluster in two different filter combinations. Indeed, in both the color combinations shown in Figure 6.2, the candidate companion star (highlighted with a large red square) is located in the CMD region between the Main Sequence and the CO-WD cooling sequence (which is clearly visible in the left panel at color $m_{F275W} - m_{F336W} < 0$). Considering the photometric errors, its position turns out to be incompatible (at more than 10σ) with both the MS and the CO-WD cooling sequence. On the other hand this is the portion of the CMD , where the He-WD cooling sequences are expected to lie. These WDs are the standard outcome of the mass-transfer processes and typically found to be orbiting MSPs . Moreover, due to its luminosity we can also expect that this is a relatively young WD. Thus on the basis of its peculiar position in the CMD we can tentatively hypothesize that the companion to NGC6652B is a recently formed He-WD.

The adopted data-set is composed of multi-epoch observations. We investigated the magnitude of the counterpart in the different frames but we found no evidence of photometric variability could be detected for the companion star. While this can be due to the poor sampling of the binary orbit, He-WD companions only rarely show variability, which is usually not related to the binary orbit but to stellar pulsations (e.g., John Antoniadis et al. 2016a; M. Kilic et al. 2015; Maxted et al. 2013; Parsons et al. 2020). Indeed, heating and/or tidal distortions are negligible in the case of a WD companion (although exceptions exist, see, e.g., Edmonds et al. 2001; Kaplan et al. 2012), while they become significant in the case of non-degenerate and Roche-Lobe filling companions (e.g., M. Cadelano et al. 2015b; Francesco R. Ferraro et al. 2001b; Pallanca et al. 2010, 2014).

6.3.2 Comparison with Binary evolution models

In order to confirm the hypothesis that the companion to NGC6652B is a He-WD, and to derive its physical properties, we compared its position in the CMD with the prediction of

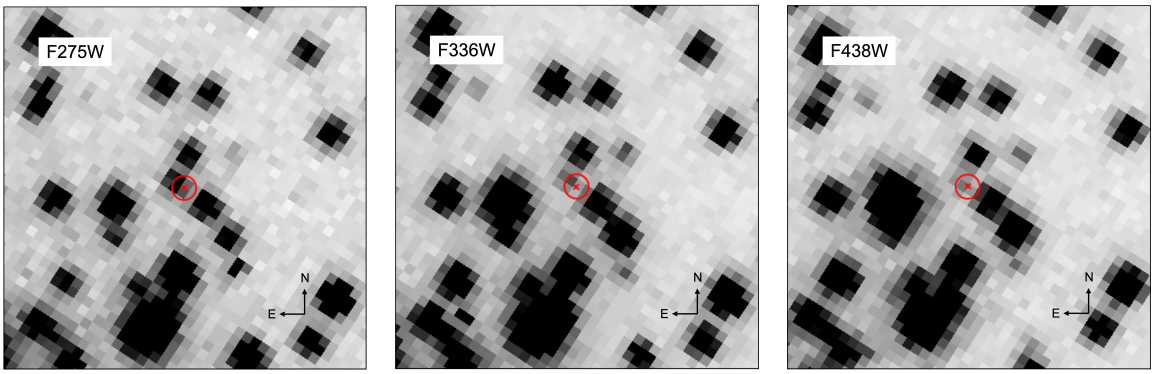

Figure 6.1: $1.5'' \times 1.5''$ finding chart of the NGC6652B companion in the F275W, F336W, and F438W filters. The red circle has a radius of 50 mas ($\sim 3sigma$ uncertainty), while the center of the circle corresponds to the position of the MSP. It is clear that the candidate counterpart (a white dwarf) gets fainter in redder filters, while most of the other stars get brighter.

theoretical binary evolution models. As first step, the performed a calibration sanity-check by comparing the observed standard evolutionary sequences (such as main-sequence and red giants) with an isochrone extracted from BaSTI database (Hidalgo et al., 2018; Pietrinferni et al., 2021) with an age of 13.25 Gyr (Dotter et al., 2010), a metallicity [Fe/H] = -0.8 (Harris, 1996, (2010 version)), and [α/Fe] = +0.4. We also compared the position of the observed WD-CO cooling sequence with a theoretical cooling track extracted from BaSTI database (Maurizio Salaris et al., 2022) for CO-WDs with a canonical mass of 0.55 $M_{\odot}$. Absolute magnitudes were converted to the observed frame by adopting a distance modulus of $(m-M)_0 = 14.97$ and a color excess of $E(B-V) = 0.1$ (in very good agreement with the values quoted by Harris 1996) and using appropriate extinction coefficients from Cardelli et al. (1989) and O'Donnell (1994). As shown in Figure 6.3, both the isochrone and the CO WD cooling track nicely reproduce the observed evolutionary sequences, thus confirming that the photometric calibration and cluster parameters are sufficiently precise to allow the next step of exploration.

In order to constrain the properties of the companion star, we extracted binary evolution models from the database described in Istrate et al. (2014b, 2016). These models follow the evolution of a NS binary during the whole mass-transfer stage, the proto-WD and the WD cooling stage. The resulting evolution tracks cover a large parameter space with a He WD mass range of 0.17 $M_{\odot}$–0.4 $M_{\odot}$, a surface temperature of 5000 K - 20000 K, and cooling ages[3]

[3]Following Istrate et al. (2016), the WD cooling age is defined as the time passed since the proto-WD reached the maximum surface temperature along the evolutionary track.

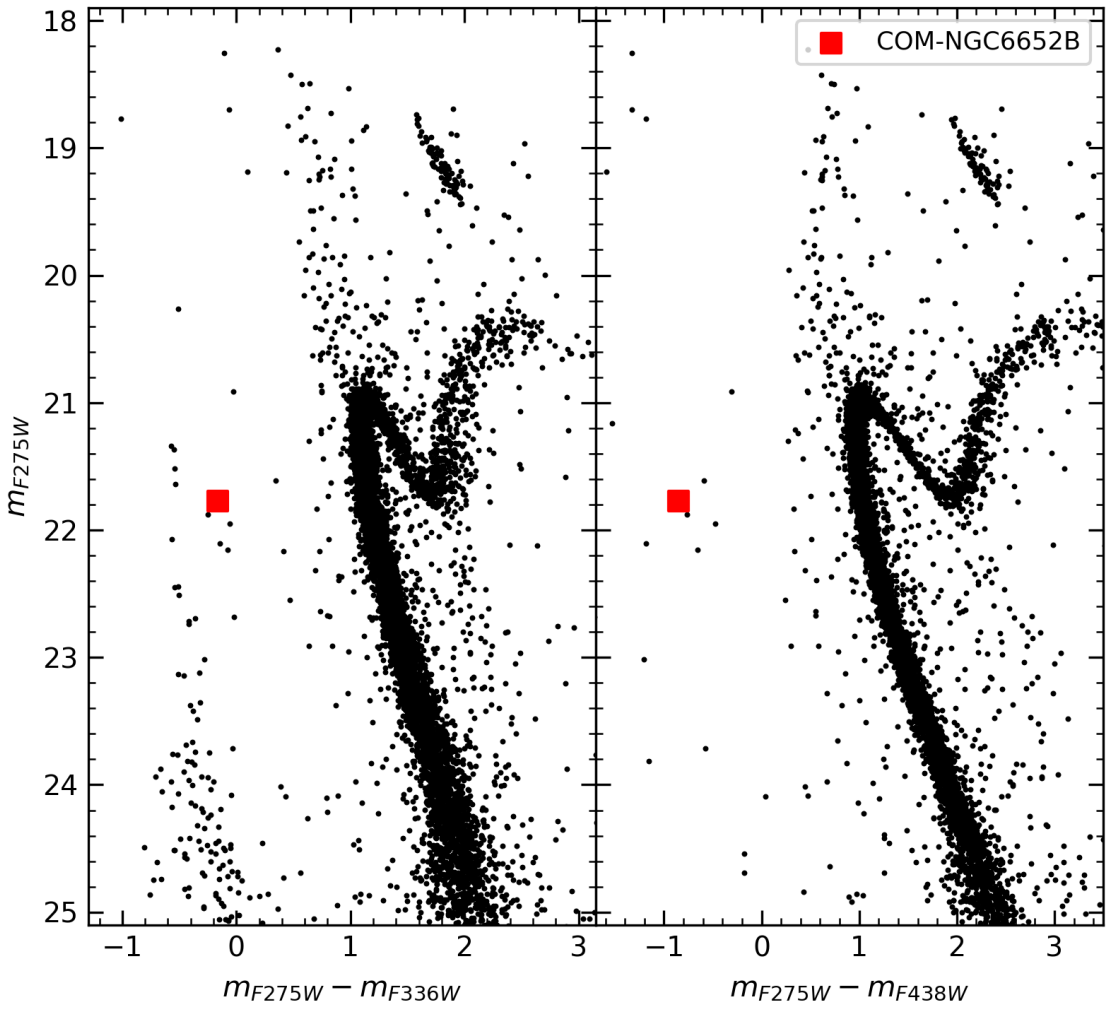

Figure 6.2: CMDs of NGC 6652. Left-panel and right-panel are ($m_{F275W} - m_{F336W}, m_{F275W}$), and ($m_{F275W} - m_{F438W}, m_{F275W}$) filter combinations, respectively. The He-core WD companion to NGC6652B is marked with a red square in each panel. The error bars are smaller than the red squares.

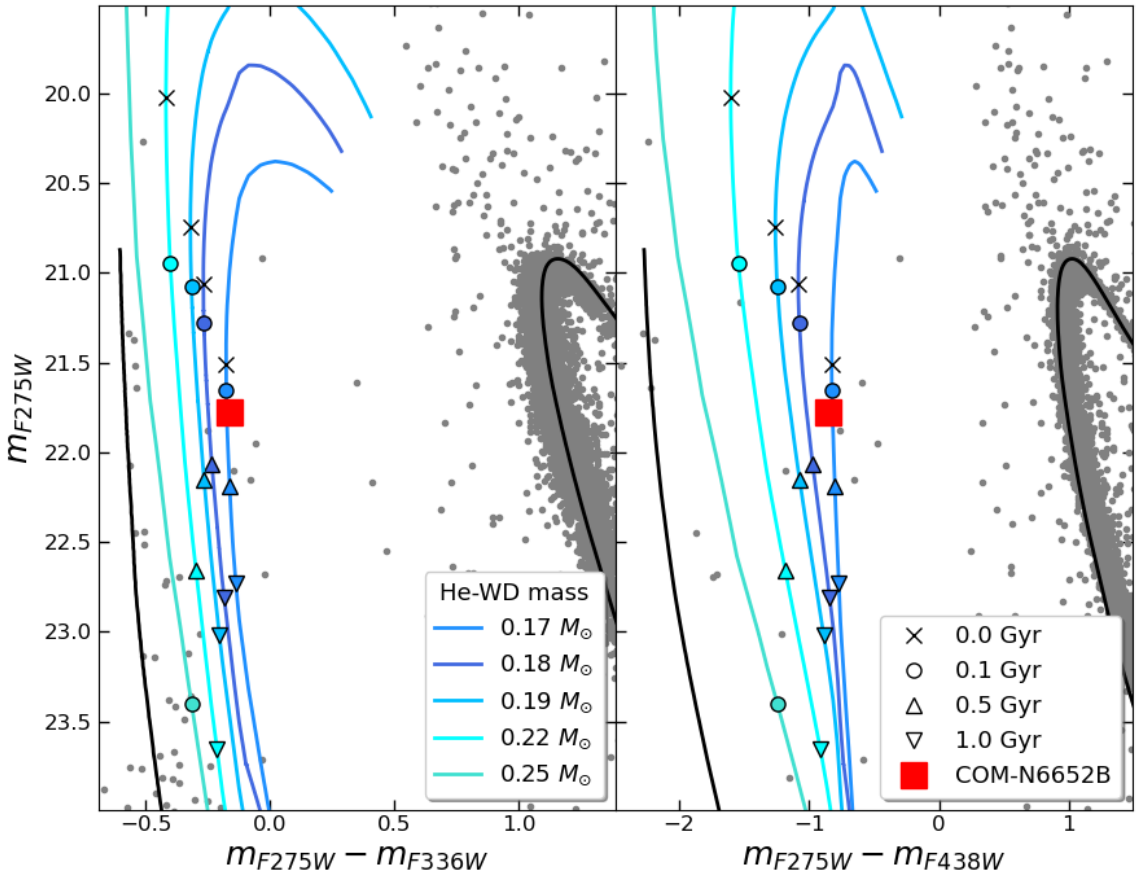

Figure 6.3: Same CMD as figure 6.2, but the WD region is zoomed in. A theoretical cooling track of a 0.55 $M_\odot$ CO-WD and an isochrone of 13.25 Gyr stellar population are marked with black lines, respectively. The other curves in color are cooling tracks of He WD with masses of $0.17M_\odot$, $0.18M_\odot$, $0.19M_\odot$,$0.22M_\odot$, from left to right, where the cooling age are marked with different symbols in tracks as reported in legend.

down to the cluster age. By using the Astrolib Pysynphot Package[4] (STScI Development Team, 2013) and WD spectra templates (Koester, 2010; Tassoul et al., 1990; Tremblay et al., 2009), the theoretical bolometric luminosities were converted to the HST-WFC3 magnitudes. A selection of the evolutionary tracks are plotted in Figure 6.3. As expected, all the tracks are located along the red side of the C-O WD sequence. The CMD position of the companion star to NGC6652B is nicely reproduced in both the filter combinations by the lowest available He-WD mass of 0.17 $M_{\odot}$, thus confirming that the identified star is an He-WD. Unfortunately, the available evolutionary tracks do not properly cover the extreme He-WD low mass end (for $M < 0.17\ M_{\odot}$). This hampers a detailed characterization of the uncertainties (see M. Cadelano et al. (2019) and Mario Cadelano et al. (2020)). However, the main physical properties of the companion star can be safely derived from the best-fit He-WD track mass (0.17 $M_{\odot}$) and deriving conservative uncertainties exploiting the available grid of higher mass tracks. In doing so the companion star turned out to have a mass of $0.17 \pm 0.02\ M_{\odot}$, a surface gravity of $\log g = 5.7 \pm 0.3\, cm\, s^{-2}$, a surface temperature of $T_{eff} = 11500 \pm 1900\, K$ and a very young age of only 200 ± 100 Myr. This confirms that the companion to NGC6652B is a recently formed He-WD. For such He-WD, the proto-WD timescale, i.e. the time spent by the companion star from the Roche-Lobe detachment to the beginning of the cooling phase is expected to last 1.2 ± 0.2 Gyr. Although this value slightly depends also on the NS mass and companion metallicity, it suggests that the mass-transfer phase in this system stopped around 1.4 Gyr ago, then the companion went through a long bloated proto-WD stage in which a significant fraction of the hydrogen in the envelope was burned through stable burning, while the star contracted eventually entering in the WD cooling sequence.

To further investigate the evolution of this system, we analyzed the growth rate of the He core of stars with different masses at the cluster metallicity extracted from the PARSEC v2.0 database (Costa et al., 2019a,b; Nguyen et al., 2022). Assuming the cluster age of 13.25 ± 0.5 Gyr (Dotter et al., 2010), the sum of the companion cooling age and proto-WD age suggests that this system experienced the end of the mass-transfer phase (i.e. Roche-Lobe detachment) when the cluster was 11.9 ± 0.5 Gyr old. Back then, only stars with masses between 0.86 $M_{\odot}$ and 0.88 $M_{\odot}$ had sufficient time to grow a He core with a mass comparable with that of the companion star (see left hand panel of Figure 6.4). This pose a firm constrain of the mass of the progenitor companion star. Stars with mass in the range 0.86 $M_{\odot}$ and 0.88 $M_{\odot}$ have developed a $0.17 \pm 0.02\ M_{\odot}$ He-core during the very early stages of the red

[4]Pysynphot: https://pysynphot.readthedocs.io/en/latest/

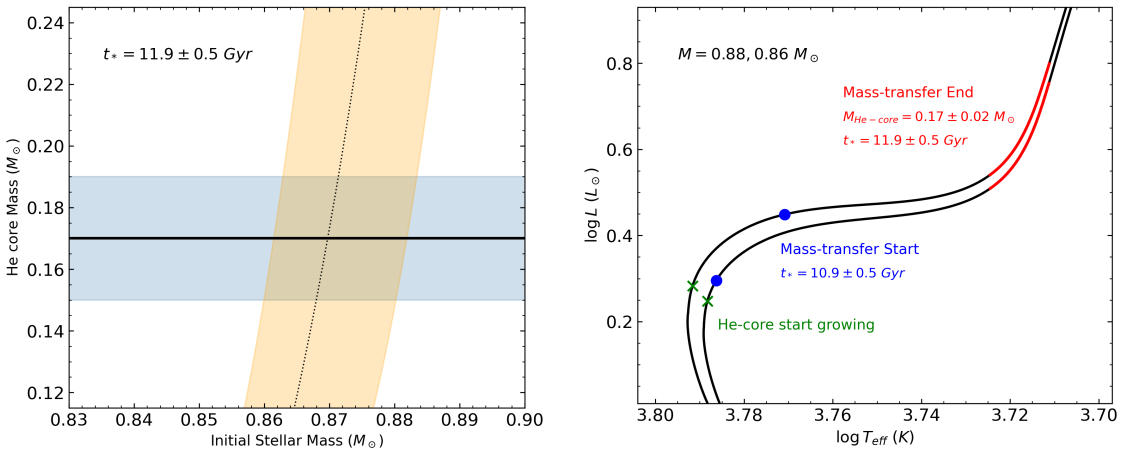

Figure 6.4: Left panel: He core mass as a function of the stellar mass as predicted by the evolutionary tracks from PARSEC v2.0 (Costa et al., 2019a,b; Nguyen et al., 2022). The black dashed curve and the light orange shaded area represent the values for an age of 11.9 ± 0.5 Gyr, corresponding to the cluster age at the epoch of Roche-Lobe detachment. The horizontal line (and blue band) marks the mass of the He WD companion to NGC6652B. Right panel: the black curves are the evolutionary track for 0.88 $M_\odot$ and 0.86 $M_\odot$ stars from left to right, respectively. The red portion of the track highlights the phase where the star had a He core with a mass comparable with the one measured for the companion star. The blue point marks the region of the tracks $\sim$ 1 Gyr before the Roche-lobe detachment, when the mass transfer probably started. Finally, the green cross marks the region where the exhausted He-core starts growing.

giant branch phase (see right hand panel of Figure 6.4). Assuming that the mass-transfer phase lasted at most 1 Gyr, then this process started when the companion star evolved to the sub-giant branch stage.

6.3.3 Constrains on the NS mass

With the determination of companion star mass, one can combine binary orbital parameters, derived through the radio timing, to constrain the mass of NS from the mass function (Andrew G. Lyne et al., 1998) :

$$f(m_p, m_c, i) = \frac{4\pi^2}{G}\frac{a^3 \sin^3 i}{P_b^2} = \frac{m_c^3 \sin^3 i}{(m_p + m_c)^2} \tag{6.1}$$

where m_p, m_c, are the NS and companion mass, respectively, i is the orbital inclination angle, a the projected semi-major axis and P_{orb} the binary period. The above equation

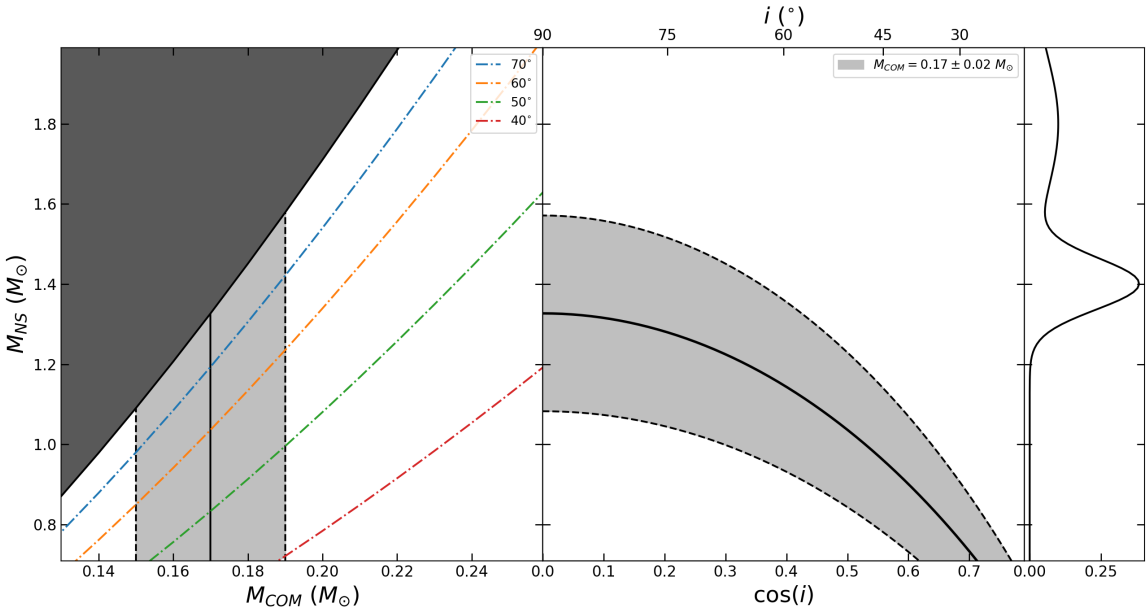

Figure 6.5: *Left-hand panel*: NS mass as a function of the companion star mass. The best-fit value of the companion mass is marked with a solid vertical line, and the corresponding uncertainties are delimited by two dashed lines. The color dotted-dashed curves indicate the NS mass - companion mass relation at different inclination angles, while the shaded area is the region forbidden by the mass-function. *Right-hand panel*: The NS mass as a function of the cosine of the inclination angle for the estimated mass of the companion star. The solid curve are values predicted by the best-fit value of the companion mass, while the light-gray shaded region delimited by the two dashed curves are the values allowed within the companion mass uncertainty. The rightmost panel shows, as reference, the NS mass distribution empirically derived by John Antoniadis et al. (2016b).

contains two unknown quantities, namely the NS mass and the orbital inclination angle. The NS mass as a function of the companion mass and inclination angles are shown in Figure 6.5, where it can be seen that the range of NS masses allowed by the known companion mass excludes the possibility of a high-mass NS. In fact, in the case of an edge-on binary, the NS mass is constrained between 1.1 $M_\odot$ and 1.6 $M_\odot$. Lower inclination angles would result in lower NS mass ranges. In principle, a canonical mass NS of $M_{NS} = 1.4\ M_\odot$ can be obtained with a large inclination angle of about $i = 80 - 90°$.

We also used a Markov Chain Monte Carlo sampler (Foreman-Mackey et al., 2019) to further constrain the mass and inclination angle of the MSP. Following Mario Cadelano et al. (2020), we defined a Gaussian likelihood function to minimize the difference between the middle and right sides of Equation 6.1. We assumed a uniform prior on the distribution

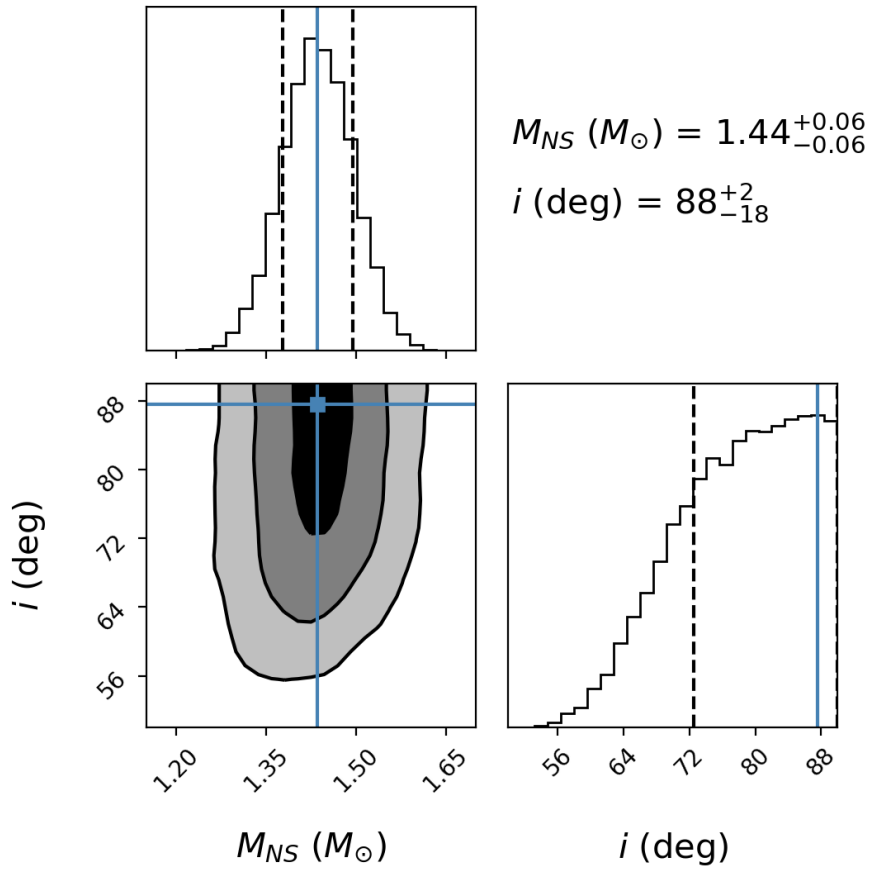

Figure 6.6: Constraints on the mass of the NS and the inclination angle of NGC 6652B. The 2D panel shows the posterior probability distribution of the two parameters, and the contours are the 1σ, 2σ, and 3σ confidence levels. The 1D histograms are the marginalized probability distributions of the two parameters, where the solid blue and black dashed lines are the best values and their related uncertainties.

of $\cos i$ and also a prior on the NS mass distribution following the one derived by John Antoniadis et al. (2016b). The posterior distribution is shown in Figure 6.6, and the results based on the 16^{th}, 50^{th}, and 84^{th} percentiles show that NGC6652B is likely a NS with a standard mass of $1.44 \pm 0.06\,M_{\odot}$ in a binary seen with a large inclination angle. In fact, the probability distribution of the inclination angle reaches the maximum values for edge-on orbits. We therefore assumed that the best value for the inclination angle corresponds to the maximum in the probability distribution and its lower uncertainty to the 16^{th} percentile: $i\,(deg) = 88^{+2}_{-18}$.

6.4 Conclusions

We used deep, high-resolution near-ultraviolet HST observations to study the binary MSPs in NGC 6652. By using the so-called “UV-route" approach, we searched for the companions to the binary MSPs in the cluster. At the corresponding position of NGC6652B we found a blue object located along the red side of the brightest portion of the WD cooling sequence. This is a He-WD, i.e. the exhausted core of an evolving star which lost its envelope likely due to the mass transfer onto the NS. The comparison with binary evolution models revealed that the companion star is a newly formed He WD with a cooling age of only 200 ± 100 Myr and a mass of $0.17 \pm 0.02\,M_{\odot}$. The companion underwent a bloated proto-WD phase which lasted 1.2 ± 0.2 Gyr. Therefore the Roche-Lobe detachment occurred $\sim$ 1.4 Gyr ago, when the cluster was 11.9 Gyr old. The progenitor star of such a young and low-mass WD was likely a $\sim 0.87\,M_{\odot}$ star which developed a He core with a mass of $0.17\,M_{\odot}$ during the first stages of the evolution along the red giant branch, before the Roche-Lobe detachment. Therefore the progenitor star lost $\sim 0.7\,M_{\odot}$ during its evolution in the binary system. Assuming that the mass-transfer stage lasted $\lesssim$ 1 Gyr, it begun when the progenitor star evolved along the sub-giant branch phase, naturally increasing its radius due to the standard stellar evolution, eventually filling its Roche-Lobe and starting the mass-transfer onto the NS primary.

Combining together the companion mass here derived and the binary orbital properties derived through radio timing, we found that this system likely hosts a NS with a mass of $1.4\,M_{\odot}$ seen at an almost edge-on orbit. The NS mass so derived is very similar to the canonical values expected and measured for these objects (e.g. Antoniadis et al. (2016b)). Since the companion lost $\sim 0.7\,M_{\odot}$ during the mass-transfer, the derived NS mass suggests that the mass-transfer phase was highly non-conservative.

A described by Gautam et al., 2022, NGC 6652A is an unusually bright pulsar, with

the pulsed component representing only a small amount of the total emission. This was inferred from the fact that it appears much more strongly in interferometric images than in the pulsed profile. This is consistent with the type of pulse profile, which seems to consist of two sinusoids, where it s not clear whether there is a real zero of emission. This already suggests that the pulsar is unusual. This was confirmed by Zhang et al., 2022: their detection of gamma-ray pulsations shows that this MSP is unusually energetic: it is only the third pulsar in a GC detected in gamma rays, after NGC 6624A (P. C. C. Freire et al., 2011) and M28A Johnson et al., 2013. From the orbital period derivative of the pulsar, Gautam et al., 2022 estimated that the intrinsic spin-down of the pulsar ($\dot{P}_{\rm int}$) is less than 6.7×10^{-20}. If the pulsar had that spin-down, it would have a characteristic age (τ_c) of 0.43 Gyr and a gamma-ray efficiency of 0.12. The latter number indicates that $\dot{P}_{\rm int}$ cannot be much smaller, otherwise the gamma-ray efficiency would be closer to 1.0. This means that τ_c cannot be much larger than 0.43 Gyr.

The idea of a young, energetic MSP revealed by the gamma-ray emission (and consistent, or at least not not contradicted by the timing) is therefore in perfect agreement with your detection of a young WD companion. The cooling age we derive (0.2 ± 0.1 Gyr) is smaller than the characteristic age ($\tau_c > 0.43$ Gyr). This is to be expected, because τ_c is computed assuming that the initial spin period is much smaller than the current spin period. For a MSP with a spin period of 1.83 ms, this is highly unlikely. For the much more probable case that the initial spin period was similar to what it is today, then the age of the pulsar is smaller than suggested by τ_c and more in agreement with the cooling age. The detection of a young WD companion is therefore valuable because it confirms the general picture of an exceptionally young, powerful MSP.

This work further confirms the strong and fruitful synergy between the new radio telescopes (such as MeerKat and FAST), and space telescopes (such as HST and JWST). Such a synergy allows to obtain a comprehensive view on the properties and evolution of binary MSPs in GCs through the observation of both the NS primaries in the radio bands and the companions in the optical bands.

Chapter 7

Summary and Conclusions

This thesis is devoted to the study of the WD populations of GGCs and it articulated in two main branches: (1) the study of the Luminosity Function (LF) of the brightest portion of the White Dwarf Cooling Sequence (WDCS) in four clusters (namely, M3, M13, M5 and NGC 6752), and (2) the search for degenerate companions to binary Millisecond pulars (MSPs) in two clusters (namely, M 13 and NGC 6652).

The results obtained in the context of first branch have yielded to the observational discovery of "slowly cooling WDs" and the presentation of a convincing scenario to explain their formation. This is described in Chapters 2, 3 and 4.

1. **Chapter 2: The first observational evidence of slowly cooling WDs, revealed in the "twin clusters" M13 and M3.** As first step of this project, we selected two GGCs (namely, M13 and M3) that share many physical properties (e.g., age, metallicity, mass etc.) and are therefore considered as "twins" systems. The main exception to this similarity concerns the morphology of their Horizontal Branch (HB): a remarkable blue extension of the HB is observed in M13, while it is absent in M3. Thanks to a "UV-guided" PSF photometry of the available HST data sets, high-quality color-magnitude diagrams (CMDs) were obtained for the two clusters. In both cases the bright portion of the WDCS is well defined and populated. We assessed the completeness of the observed WD samples through extensive artificial star experiments. Then, we compared the completeness-corrected WD LFs of the

two systems, each one properly normalized the overall respective cluster populations, finding a significant excess of WDs in M13 with respected to those counted in M3 at the same level of magnitude. This observational evidence and the comparison with the predictions of "standard" WD cooling models suggest that the WD cooling process is significantly slowed down in M13, while it agrees with the theoretical expectations in M3. Noteworthy, this result is well consistent with the different HB morphologies of the two systems. In fact, the HB blue tail of M13 is populated by low-mass stars that skip the Asymptotic Giant Branch (AGB) phase and therefore do not experience the third dredge-up, a deep convection event during which most of the hydrogen in the envelope is brought to the inner layers and there burned. This implies that most of the WDs in M13 have a residual hydrogen envelope thick enough to guarantee stable thermonuclear activity, at least during the early phase the WDCS, which yields to a significant increase of their cooling time. Conversely, all the HB stars in M3 (where no HB blue extension is observed) experience the AGB phase and the third dredge-up, thus remaining with not enough hydrogen in their envelope and evolving as "standard" (purely cooling) WDs

2. **Chapter 3: Confirming the existence of slowly cooling WDs in NGC 6752.** As next step, we investigated the WDCS in NGC 6752, a GGC with metallicity and HB morphology similar to those of M13. After performing the data reduction and artificial star tests, a high-quality and completed sample of WDs has been obtained. To properly take into account the different cluster total masses, we have normalized the WD LFs to the number of Red Giant Branch (RGB) stars counted in the two systems. The RGB populations have been selected in a perfectly coherent way because, after the application of just a small shift in magnitude, the overall morphology of the CMD of M13 nicely matches that of NGC 6752. Except for reaching much fainter magnitudes, the WD LF of NGC 6752 impressively agrees with that of M13, with the portions in common being almost indistinguishable. In addition, it is inconsistent with theoretical predictions for a population of purely cooling WDs, while it is properly reproduced by models that include $\sim 70\%$ of slowly cooling WDs, as in M13. This provides strong evidence that the two clusters share the same type of WD populations, suggesting that also NGC 6752 hosts a relevant fraction of slowly cooling WDs, and further confirm the relation between the presence of these stars and a blue tail HB morphology.

3. **Chapter 4: confirming the link between slowly cooling WDs and the HB morphol-**

ogy in M5. As a further check, we investigated the WDCS in NGC 5904 (M5), which is a GC with a HB morphology similar to that of M3, but with slightly larger metallicity (Δ[Fe/H]$\sim$ +0.2 dex). By using the same approach described above, we obtained the UV-CMD of M5, which shows a well defined WDCS. We also performed artificial star tests to evaluate the completeness along the entire extension of the WDCS. Taking into account that the different metallicity of the two clusters prevents a direct comparison of their evolutionary sequences in the CMD, to avoid introducing biases in the normalization process, we normalized the WD LFs to the cluster total luminosity. The results show that the WD LFs in the two systems are similar, thus suggesting that also M5 is mainly populated by canonical WDs, coherently with its (no blue tail) HB morphology.

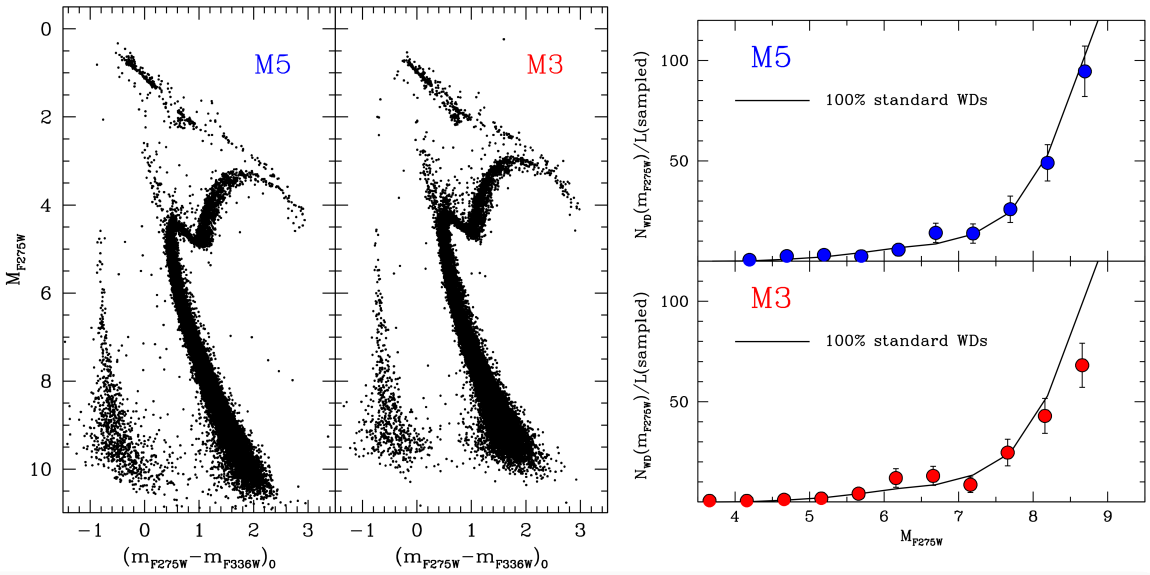

Figure 7.1: *Left:* Near-ultraviolet color-magnitude diagrams of the pair M5 and M3, reported in the absolute plane by adopting the distance modulus and reddening from F. R. Ferraro et al. (1999). *Right:* WD-LFs normalized to the cluster light sampled by the HST observations (blue and red points for M5 and M3, respectively) . The solid line is the model expectation for a population of pure "standard" WDs.

The results are summarized in Figure 7.1 and Figure 7.2 where the CMDs and the WD-LF are shown for the two pairs of clusters investigated: Figure 7.1 show the couple M5 and M3 both with a not extended HB and both showing a WD-LF fully consistent with that expected for a population of standard WDs. In Figure 7.2 the case of the pair M13-NGC6752 is

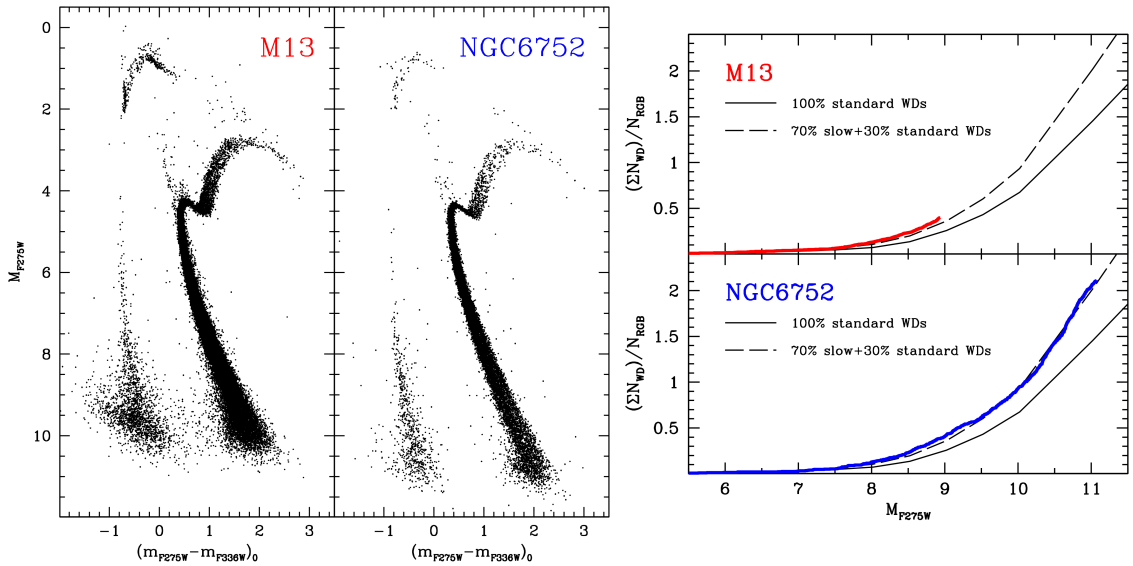

Figure 7.2: *Left:* Near-ultraviolet color-magnitude diagrams of the pair M13 and NGC6752 reported in the absolute plane by adopting the distance modulus and reddening from F. R. Ferraro et al. (1999). *Right:* Cumulative WD-LFs normalized to the number of RGB (red and blue heavy solid line for M13 and NGC6752, respectively). The black solid line is the model expectation for a population of pure "standard" WDs, while the black dashed line (that nicely reproduces the observed distribution) is the behavior expected for a population of 70% of slowly cooling WDs.

illustrated: the two clusters share the same extended blue HB-morphology and the WD-LFs turned out to be consistent with a content of $\sim$ 70% of slowly cooling WDs.

This thesis therefore presented the first observational evidence of a new class of WDs, which we named "slowly cooling WDs", in GCs showing an HB morphology with a long blue tail. These stars were predicted by Leandro G. Althaus et al. (2015), but never observed yet. Indeed, following stellar evolutionary models, stars less massive than $\sim 0.56\ M_{\odot}$ evolve along the blue extension of the HB and then skip the AGB evolutionary phase, which immediately precedes the WD stage. This implies that they do not experience the third dredge-up, and keep a very thin hydrogen-rich shell (with a mass of the order of $0.0001\ M_{\odot}$) where stable thermonuclear burning occurs: this is an active energy source that slows down their cooling process. Hence, slowly cooling WDs look similar to their canonical sisters (i.e., they are indistinguishable from their photometric properties), but have significantly longer cooling times, which makes them "accumulating" in the CMD in the bright-end of the cooling sequence. Finally, such a scenario has been solidly assessed by the observational results obtained in this thesis, through an unprecedented analysis of the WD cooling sequences in a

few GGCs. The extension of this investigation to clusters with extended HB blue tail in the extreme low metallicity regime, where the phenomenon is expected to reach its maximum efficiency, is the next step of this investigation, necessary to fully verify the theoretical predictions and provide an empirical measure of the impact of these results on the use of the WD cooling sequences as chronometers to measure cosmic ages.

The results obtained in the second research branch have yielded to the discovery of two new optical companions to binary MSPs. This is another very promising research field dealing with WD properties, since a degenerate exhausted object (an He or a CO WD) is expected as natural outcome of the evolutionary path that re-accelerates a neutron star to generate a MSP. In fact, following the canonical scenario, MSPs are thought to be originated in binary systems where a neutron star accretes matter (and angular momentum) from a companion star. At the end of the accretion process, the neutron star is re-accelerated at millisecond spin periods (hence, a MSP is born) and only the degenerate core of the peeled companion stars (i.e., a He or CO WD) remains bound to the MSP in the binary system. However, non-degenerate companion stars have been found in a few cases, thus indicating that the formation of MSPs likely is more complex than previously thought, and it is possibly affected also by internal dynamical processes occurring in GCs. Hence, the identification and the characterization of the optical companions to binary MSPs is crucial to get information on the MSP formation channels (and epoch). Moreover, it opens the possibility to estimate the mass of the companion star, which can be combined with the orbital properties of the system and provide invaluable constraints to the neutron star mass.

The present thesis work has contributed to this fascinating research field by identifying the companion stars to two binary MSPs in the GCs M13 and NGC 6652. They are both He-core WDs, according to the canonical recycling scenario. The mass of the WD companion in M13 suggests that the neutron star could be as massive as $2.4 \pm 0.5\ M_{\odot}$, while the WD cooling age estimated in the case of NGC 6652 puts a constrain on the epoch of the accretion process that re-accelerated the MSP. This has been described in Chapters 5 and 6.

1. **Chapter 5: Discovery of a low-mass He-core white dwarf orbiting a possible high-mass neutron star in M13.** PSR J1631+3627 (hereafter M13F) is a new MSP discovered in M13. We used the photometric catalog of M13 to search for the optical companion to M13F, at the same position as the radio source, a faint WD was found (F275W = 23.7). After a comparison with He WD cooling models, we estimate that it has a mass of $0.23 \pm 0.03\ M_{\odot}$. Combining the results with published constraints on the orbital parameters obtained through pulsar timing, we estimate the pulsar mass to

be $M_{NS,med} = 2.4 \pm 0.5\ M_{\odot}$ with a inclination angle of 60° or $1.5 \pm 0.1\ M_{\odot}$ with a inclination angle of around 40°.

2. **Chapter 6: Discovery of a young WD orbiting a neutron star in NGC 6652.** PSR J1835-3259B (hereafter NGC 6652B) is the second MSP discovered in NGC 6652, which is a old GC with intermediate metallicity, located in the Galactic bulge. After performing a UV-guided search for the companion star in the available HST data set, we found on object at the same position to the radio signal, lying in the He WD region of of the cluster CMD. From theoretical cooling tracks, we estimated the physical properties of this star: it is a He WD with a mass of $0.17 \pm 0.02\ M_{\odot}$, and a very short cooling time (only 200 Myr), suggesting a very recent formation epoch for the MSP. By combining this information with the neutron star mass function, we estimated that the neutron star has a canonical mass of $1.4 \pm 0.1\ M_{\odot}$ with a low-inclination angle of $\sim 88°$.

Reference

Abbate, F. et al. (Nov. 2018). "Internal gas models and central black hole in 47 Tucanae using millisecond pulsars". In: MNRAS 481.1, pp. 627–638. DOI: 10.1093/mnras/sty2298. arXiv: 1808.06621 [astro-ph.HE].

Abbate, Federico et al. (Oct. 2019). "Evidence of Nonluminous Matter in the Center of M62". In: ApJ 884.1, L9, p. L9. DOI: 10.3847/2041-8213/ab46c3. arXiv: 1909.11091 [astro-ph.HE].

Ablimit, Iminhaji et al. (July 2022). "Stellar core-merger-induced collapse: new formation pathways for black holes, Thorne-Żytkow objects, magnetars, and superluminous supernovae". In: MNRAS 513.4, pp. 4802–4813. DOI: 10.1093/mnras/stac631. arXiv: 2108.08430 [astro-ph.HE].

Alpar, M. A. et al. (Dec. 1982). "A new class of radio pulsars". In: Nature 300.5894, pp. 728–730. DOI: 10.1038/300728a0.

Althaus, L. G. et al. (May 2001a). "Diffusion and the occurrence of hydrogen-shell flashes in helium white dwarf stars". In: MNRAS 323.2, pp. 471–483. DOI: 10.1046/j.1365-8711.2001.04227.x. arXiv: astro-ph/0012545 [astro-ph].

— (June 2001b). "The impact of element diffusion on the formation and evolution of helium white dwarf stars". In: MNRAS 324.3, pp. 617–622. DOI: 10.1046/j.1365-8711.2001.04324.x.

Althaus, L. G. et al. (Sept. 2005). "The formation of DA white dwarfs with thin hydrogen envelopes". In: A&A 440.1, pp. L1–L4. DOI: 10.1051/0004-6361:200500159. arXiv: astro-ph/0507415 [astro-ph].

Althaus, Leandro G. et al. (Apr. 2015). "White dwarf evolutionary sequences for low-metallicity progenitors: The impact of third dredge-up". In: A&A 576, A9, A9. DOI: 10.1051/0004-6361/201424922. arXiv: 1502.03882 [astro-ph.SR].

Annunziatella, M. et al. (Jan. 2013). "Inside Catalogs: A Comparison of Source Extraction Software". In: PASP 125.923, p. 68. DOI: 10.1086/669333. arXiv: 1212.0564 [astro-ph.IM].

Antoniadis, J. et al. (July 2012). "The relativistic pulsar-white dwarf binary PSR J1738+0333 - I. Mass determination and evolutionary history". In: MNRAS 423.4, pp. 3316–3327. DOI: 10.1111/j.1365-2966.2012.21124.x. arXiv: 1204.3948 [astro-ph.HE].

Antoniadis, John et al. (Apr. 2013). "A Massive Pulsar in a Compact Relativistic Binary". In: *Science* 340.6131, p. 448. DOI: 10.1126/science.1233232. arXiv: 1304.6875 [astro-ph.HE].

Antoniadis, John et al. (Oct. 2016a). "An Eccentric Binary Millisecond Pulsar with a Helium White Dwarf Companion in the Galactic field". In: ApJ 830.1, 36, p. 36. DOI: 10.3847/0004-637X/830/1/36. arXiv: 1601.08184 [astro-ph.SR].

Antoniadis, John et al. (May 2016b). "The millisecond pulsar mass distribution: Evidence for bimodality and constraints on the maximum neutron star mass". In: *arXiv e-prints*, arXiv:1605.01665, arXiv:1605.01665. arXiv: 1605.01665 [astro-ph.HE].

Archibald, Anne M. et al. (Oct. 2010). "X-ray Variability and Evidence for Pulsations from the Unique Radio Pulsar/X-ray Binary Transition Object FIRST J102347.6+003841". In: ApJ 722.1, pp. 88–95. DOI: 10.1088/0004-637X/722/1/88. arXiv: 1008.1068 [astro-ph.HE].

Arellano Ferro, A. et al. (Sept. 2016a). "A new overview of secular period changes of RR Lyrae stars in M5". In: MNRAS 461.1, pp. 1032–1044. DOI: 10.1093/mnras/stw1358. arXiv: 1606.01181 [astro-ph.SR].

Arellano Ferro, A. et al. (May 2016b). "RR Lyrae stars and the horizontal branch of NGC 5904 (M5)". In: Ap&SS 361.5, 175, p. 175. DOI: 10.1007/s10509-016-2757-5. arXiv: 1604.03981 [astro-ph.SR].

Baumgardt, H. et al. (Aug. 2021). "Accurate distances to Galactic globular clusters through a combination of Gaia EDR3, HST, and literature data". In: MNRAS 505.4, pp. 5957–5977. DOI: 10.1093/mnras/stab1474. arXiv: 2105.09526 [astro-ph.GA].

Bédard, A. et al. (Oct. 2020). "On the Spectral Evolution of Hot White Dwarf Stars. I. A Detailed Model Atmosphere Analysis of Hot White Dwarfs from SDSS DR12". In: ApJ 901.2, 93, p. 93. DOI: 10.3847/1538-4357/abafbe. arXiv: 2008.07469 [astro-ph.SR].

Bedding, Timothy R. et al. (Mar. 2011). "Gravity modes as a way to distinguish between hydrogen- and helium-burning red giant stars". In: Nature 471.7340, pp. 608–611. DOI: 10.1038/nature09935. arXiv: 1103.5805 [astro-ph.SR].

Bedin, L. R. et al. (Jan. 2010). "The Bottom of the White Dwarf Cooling Sequence in the Old Open Cluster NGC 2158". In: ApJ 708.1, pp. L32–L35. DOI: 10.1088/2041-8205/708/1/L32. arXiv: 0912.0257 [astro-ph.GA].

Bedin, L. R. et al. (Sept. 2019). "The HST large programme on NGC 6752 - III. Detection of the peak of the white dwarf luminosity function". In: MNRAS 488.3, pp. 3857–3865. DOI: 10.1093/mnras/stz1968. arXiv: 1907.06300 [astro-ph.SR].

Bedin, L. R. et al. (Jan. 2023). "The HST large programme on NGC 6752 - IV. The White Dwarf sequence". In: MNRAS 518.3, pp. 3722–3736. DOI: 10.1093/mnras/stac3219. arXiv: 2211.02391 [astro-ph.SR].

Bellazzini, Michele et al. (Mar. 2002). "Deep Hubble Space Telescope WFPC2 Photometry of NGC 288. I. Binary Systems and Blue Stragglers". In: AJ 123.3, pp. 1509–1527. DOI: 10.1086/339222. arXiv: astro-ph/0112343 [astro-ph].

Bellini, A. et al. (Apr. 2010). "The end of the white dwarf cooling sequence in M 67". In: A&A 513, A50, A50. DOI: 10.1051/0004-6361/20091372110.48550/arXiv.1001.3827. arXiv: 1001.3827 [astro-ph.SR].

Bellini, A. et al. (May 2011). "Astrometry and Photometry with HST WFC3. II. Improved Geometric-Distortion Corrections for 10 Filters of the UVIS Channel". In: PASP 123.903, p. 622. DOI: 10.1086/659878. arXiv: 1102.5218 [astro-ph.IM].

Bellini, A. et al. (June 2013). "A Double White-dwarf Cooling Sequence in ω Centauri". In: ApJ 769.2, L32, p. L32. DOI: 10.1088/2041-8205/769/2/L32. arXiv: 1305.0265 [astro-ph.GA].

Belloni, Diogo et al. (Feb. 2019). "MOCCA-SURVEY database I. Accreting white dwarf binary systems in globular clusters - IV. Cataclysmic variables - properties of bright and faint populations". In: MNRAS 483.1, pp. 315–331. DOI: 10.1093/mnras/sty3097. arXiv: 1811.04937 [astro-ph.GA].

Belloni, Diogo et al. (Jan. 2020). "Are most Cataclysmic Variables in Globular Clusters dynamically formed?" In: *Star Clusters: From the Milky Way to the Early Universe*. Ed. by Angela Bragaglia et al. Vol. 351, pp. 404–407. DOI: 10.1017/S174392131900718X. arXiv: 1907.06527 [astro-ph.GA].

Benvenuto, O. G. et al. (May 2002). "Time-dependent diffusion in pulsating white dwarf stars: asteroseismology of G117-B15A". In: MNRAS 332.2, pp. 399–408. DOI: 10.1046/j.1365-8711.2002.05312.x. arXiv: astro-ph/0201226 [astro-ph].

Bhattacharya, D. et al. (Jan. 1991). "Formation and evolution of binary and millisecond radio pulsars". In: Phys. Rep. 203.1-2, pp. 1–124. DOI: 10.1016/0370-1573(91)90064-S.

Bica, E. et al. (June 2016). “Globular Clusters in the Galactic Bulge”. In: PASA 33, e028, e028. DOI: 10.1017/pasa.2015.47. arXiv: 1510.07834 [astro-ph.SR].

Bogdanov, Slavko et al. (Dec. 2019). “Constraining the Neutron Star Mass-Radius Relation and Dense Matter Equation of State with NICER. I. The Millisecond Pulsar X-Ray Data Set”. In: ApJ 887.1, L25, p. L25. DOI: 10.3847/2041-8213/ab53eb. arXiv: 1912.05706 [astro-ph.HE].

Bohlin, Ralph C. (Sept. 2016). “Perfecting the Photometric Calibration of the ACS CCD Cameras”. In: AJ 152.3, 60, p. 60. DOI: 10.3847/0004-6256/152/3/60. arXiv: 1606.01838 [astro-ph.IM].

Bono, G. et al. (Dec. 2020). “Evolutionary and pulsation properties of Type II Cepheids”. In: A&A 644, A96, A96. DOI: 10.1051/0004-6361/202038191. arXiv: 2009.06985 [astro-ph.SR].

Bradley, P. A. (June 1998). “Asteroseismological Constraints on the Structure of the ZZ Ceti Stars G117-B15A and R548”. In: ApJS 116.2, pp. 307–319. DOI: 10.1086/313102.

Bressan, Alessandro et al. (Nov. 2012). “PARSEC: stellar tracks and isochrones with the PAdova and TRieste Stellar Evolution Code”. In: MNRAS 427.1, pp. 127–145. DOI: 10.1111/j.1365-2966.2012.21948.x. arXiv: 1208.4498 [astro-ph.SR].

Breton, R. P. et al. (June 2013). “Discovery of the Optical Counterparts to Four Energetic Fermi Millisecond Pulsars”. In: ApJ 769.2, 108, p. 108. DOI: 10.1088/0004-637X/769/2/108. arXiv: 1302.1790 [astro-ph.HE].

Buonanno, R. et al. (Oct. 1994). “The stellar population of the globular cluster M 3. I. Photographic photometry of 10 000 stars”. In: A&A 290, pp. 69–103.

Cadelano, M. (Jan. 2019). “The Exotic Zoo of Millisecond Pulsars in Globular Clusters: a multi-wavelength study”. In: *arXiv e-prints*, arXiv:1901.04212, arXiv:1901.04212. arXiv: 1901.04212 [astro-ph.HE].

Cadelano, M. et al. (Oct. 2015a). “Optical Identification of He White Dwarfs Orbiting Four Millisecond Pulsars in the Globular Cluster 47 Tucanae”. In: ApJ 812.1, 63, p. 63. DOI: 10.1088/0004-637X/812/1/63. arXiv: 1509.01397 [astro-ph.SR].

Cadelano, M. et al. (July 2015b). “Radio Timing and Optical Photometry of the Black Widow System PSR J1953+1846A in the Globular Cluster M71”. In: ApJ 807.1, 91, p. 91. DOI: 10.1088/0004-637X/807/1/91. arXiv: 1505.03531 [astro-ph.SR].

Cadelano, M. et al. (Feb. 2017a). “Proper Motions and Structural Parameters of the Galactic Globular Cluster M71”. In: ApJ 836.2, 170, p. 170. DOI: 10.3847/1538-4357/aa5ca5. arXiv: 1701.07834 [astro-ph.SR].

Cadelano, M. et al. (July 2017b). "The Optical Counterpart to the Accreting Millisecond X-Ray Pulsar SAX J1748.9-2021 in the Globular Cluster NGC 6440". In: ApJ 844.1, 53, p. 53. DOI: 10.3847/1538-4357/aa7b7f. arXiv: 1706.07061 [astro-ph.HE].

Cadelano, M. et al. (Mar. 2018). "Discovery of Three New Millisecond Pulsars in Terzan 5". In: ApJ 855.2, 125, p. 125. DOI: 10.3847/1538-4357/aaac2a. arXiv: 1801.09929 [astro-ph.HE].

Cadelano, M. et al. (Apr. 2019). "An Extremely Low-mass He White Dwarf Orbiting the Millisecond Pulsar J1342+2822B in the Globular Cluster M3". In: ApJ 875.1, 25, p. 25. DOI: 10.3847/1538-4357/ab0e6b. arXiv: 1903.03345 [astro-ph.HE].

Cadelano, M. et al. (Dec. 2020). "Radial variation of the stellar mass functions in the globular clusters M15 and M30: clues of a non-standard IMF?" In: MNRAS 499.2, pp. 2390–2400. DOI: 10.1093/mnras/staa2759. arXiv: 2009.02333 [astro-ph.GA].

Cadelano, Mario et al. (Dec. 2020). "PSR J1641+3627F: A Low-mass He White Dwarf Orbiting a Possible High-mass Neutron Star in the Globular Cluster M13". In: ApJ 905.1, 63, p. 63. DOI: 10.3847/1538-4357/abc345. arXiv: 2010.09740 [astro-ph.HE].

Cadelano, Mario et al. (Dec. 2022). "Discovery of a Double Sequence of Blue Straggler Stars in the Core-collapsed Globular Cluster NGC 6256". In: ApJ 941.1, 69, p. 69. DOI: 10.3847/1538-4357/aca016. arXiv: 2211.02671 [astro-ph.SR].

Campbell, S. W. et al. (Sept. 2017). "NGC 6752 AGB stars revisited. I. Improved AGB temperatures remove apparent overionisation of Fe I". In: A&A 605, A98, A98. DOI: 10.1051/0004-6361/201731101. arXiv: 1707.02840 [astro-ph.SR].

Campbell, Simon W. et al. (June 2013). "Sodium content as a predictor of the advanced evolution of globular cluster stars". In: Nature 498.7453, pp. 198–200. DOI: 10.1038/nature12191. arXiv: 1305.7090 [astro-ph.SR].

Campos, Fabíola et al. (Mar. 2016). "A comparative analysis of the observed white dwarf cooling sequence from globular clusters". In: MNRAS 456.4, pp. 3729–3742. DOI: 10.1093/mnras/stv2911. arXiv: 1512.03114 [astro-ph.SR].

Campos, Fabíola et al. (Dec. 2018). "Outliers: multicolour photometry guiding the search for evolved binary systems in the globular cluster 47 Tucanae". In: MNRAS 481.4, pp. 4397–4409. DOI: 10.1093/mnras/sty2591. arXiv: 1809.07746 [astro-ph.SR].

Cardelli, Jason A. et al. (Oct. 1989). "The Relationship between Infrared, Optical, and Ultraviolet Extinction". In: ApJ 345, p. 245. DOI: 10.1086/167900.

Carretta, E. et al. (Dec. 2009a). "Intrinsic iron spread and a new metallicity scale for globular clusters". In: A&A 508.2, pp. 695–706. DOI: 10.1051/0004-6361/200913003. arXiv: 0910.0675 [astro-ph.GA].

Carretta, E. et al. (Oct. 2009b). "Na-O anticorrelation and HB. VII. The chemical composition of first and second-generation stars in 15 globular clusters from GIRAFFE spectra". In: A&A 505.1, pp. 117–138. DOI: 10.1051/0004-6361/200912096. arXiv: 0909.2938 [astro-ph.GA].

Carretta, E. et al. (Oct. 2009c). "Na-O anticorrelation and HB. VIII. Proton-capture elements and metallicities in 17 globular clusters from UVES spectra". In: A&A 505.1, pp. 139–155. DOI: 10.1051/0004-6361/200912097. arXiv: 0909.2941 [astro-ph.GA].

Carroll, Bradley W. et al. (2017). *An introduction to modern astrophysics, Second Edition*.

Cassisi, Santi et al. (Nov. 2014). "On the missing second generation AGB stars in NGC 6752". In: A&A 571, A81, A81. DOI: 10.1051/0004-6361/201424540. arXiv: 1410.3599 [astro-ph.SR].

Catalán, S. et al. (July 2008). "The initial-final mass relationship of white dwarfs revisited: effect on the luminosity function and mass distribution". In: MNRAS 387.4, pp. 1693–1706. DOI: 10.1111/j.1365-2966.2008.13356.x. arXiv: 0804.3034 [astro-ph].

Catelan, M. (Apr. 2009). "Horizontal branch stars: the interplay between observations and theory, and insights into the formation of the Galaxy". In: Ap&SS 320, pp. 261–309. DOI: 10.1007/s10509-009-9987-8. arXiv: astro-ph/0507464 [astro-ph].

Chen, Jianxing et al. (Nov. 2019). "G132-12: A one-mode ZZ Ceti star located at the blue edge of instability strip". In: New A 73, 101276, p. 101276. DOI: 10.1016/j.newast.2019.101276.

Chen, Jianxing et al. (Sept. 2021). "Slowly cooling white dwarfs in M13 from stable hydrogen burning". In: *Nature Astronomy* 5, pp. 1170–1177. DOI: 10.1038/s41550-021-01445-6. arXiv: 2109.02306 [astro-ph.GA].

Chen, Jianxing et al. (Aug. 2022). "Slowly Cooling White Dwarfs in NGC 6752". In: ApJ 934.2, 93, p. 93. DOI: 10.3847/1538-4357/ac7a45. arXiv: 2206.10039 [astro-ph.SR].

Cheng, Zhongqun et al. (May 2019a). "Exploring the Mass Segregation Effect of X-Ray Sources in Globular Clusters: The Case of 47 Tucanae". In: ApJ 876.1, 59, p. 59. DOI: 10.3847/1538-4357/ab1593. arXiv: 1904.01404 [astro-ph.HE].

Cheng, Zhongqun et al. (Sept. 2019b). "Exploring the Mass Segregation Effect of X-Ray Sources in Globular Clusters. II. The Case of Terzan 5". In: ApJ 883.1, 90, p. 90. DOI: 10.3847/1538-4357/ab3c6d. arXiv: 1908.06392 [astro-ph.HE].

Cho, Dong-Hwan et al. (Apr. 2005). "Different Characteristics of the Bright Branches of the Globular Clusters M3 and M13". In: AJ 129.4, pp. 1922–1933. DOI: 10.1086/428369.

Cocozza, G. et al. (Apr. 2006). "The Puzzling Properties of the Helium White Dwarf Orbiting the Millisecond Pulsar PSR J1911-5958A in NGC 6752". In: ApJ 641.2, pp. L129–L132. DOI: 10.1086/504040. arXiv: astro-ph/0603269 [astro-ph].

Cocozza, G. et al. (June 2008). "A Puzzling Millisecond Pulsar Companion in NGC 6266". In: ApJ 679.2, p. L105. DOI: 10.1086/589557. arXiv: 0804.3574 [astro-ph].

Corongiu, A. et al. (Dec. 2012). "A Shapiro Delay Detection in the Binary System Hosting the Millisecond Pulsar PSR J1910-5959A". In: ApJ 760.2, 100, p. 100. DOI: 10.1088/0004-637X/760/2/100. arXiv: 1210.1167 [astro-ph.SR].

Córsico, Alejandro H. et al. (Sept. 2019). "Pulsating white dwarfs: new insights". In: A&A Rev. 27.1, 7, p. 7. DOI: 10.1007/s00159-019-0118-4. arXiv: 1907.00115 [astro-ph.SR].

Costa, Guglielmo et al. (June 2019a). "Mixing by overshooting and rotation in intermediate-mass stars". In: MNRAS 485.4, pp. 4641–4657. DOI: 10.1093/mnras/stz728. arXiv: 1903.04368 [astro-ph.SR].

Costa, Guglielmo et al. (Nov. 2019b). "Multiple stellar populations in NGC 1866. New clues from Cepheids and colour-magnitude diagram". In: A&A 631, A128, A128. DOI: 10.1051/0004-6361/201936409. arXiv: 1909.01907 [astro-ph.SR].

Cromartie, H. T. et al. (Jan. 2020). "Relativistic Shapiro delay measurements of an extremely massive millisecond pulsar". In: *Nature Astronomy* 4, pp. 72–76. DOI: 10.1038/s41550-019-0880-2. arXiv: 1904.06759 [astro-ph.HE].

Dai, S. et al. (June 2017). "The Identification of the White Dwarf Companion to the Millisecond Pulsar J2317+1439". In: ApJ 842.2, 105, p. 105. DOI: 10.3847/1538-4357/aa7209. arXiv: 1705.02593 [astro-ph.SR].

Dalessandro, E. et al. (Dec. 2013a). "Double Blue Straggler Sequences in Globular Clusters: The Case of NGC 362". In: ApJ 778.2, 135, p. 135. DOI: 10.1088/0004-637X/778/2/13510.48550/arXiv.1310.2389. arXiv: 1310.2389 [astro-ph.SR].

Dalessandro, E. et al. (Mar. 2013b). "The horizontal branch in the UV colour-magnitude diagrams - II. The case of M3, M13 and M79". In: MNRAS 430.1, pp. 459–471. DOI: 10.1093/mnras/sts644. arXiv: 1212.4419 [astro-ph.SR].

Dalessandro, E. et al. (Sept. 2015). "No Evidence of Mass Segregation in the Low-mass Galactic Globular Cluster NGC 6101". In: ApJ 810.1, 40, p. 40. DOI: 10.1088/0004-637X/810/1/40. arXiv: 1507.04776 [astro-ph.GA].

Dalessandro, E. et al. (Oct. 2018a). "IC 4499 revised: Spectro-photometric evidence of small light-element variations". In: A&A 618, A131, A131. DOI: 10.1051/0004-6361/201833650. arXiv: 1807.07618 [astro-ph.SR].

Dalessandro, E. et al. (May 2018b). "The Peculiar Radial Distribution of Multiple Populations in the Massive Globular Cluster M80". In: ApJ 859.1, 15, p. 15. DOI: 10.3847/1538-4357/aabb56. arXiv: 1804.03222 [astro-ph.SR].

DeCesar, Megan E. et al. (July 2015). "A Highly Eccentric 3.9 Millisecond Binary Pulsar in the Globular Cluster NGC 6652". In: ApJ 807.2, L23, p. L23. DOI: 10.1088/2041-8205/807/2/L23. arXiv: 1506.03367 [astro-ph.HE].

Demorest, P. B. et al. (Oct. 2010). "A two-solar-mass neutron star measured using Shapiro delay". In: Nature 467.7319, pp. 1081–1083. DOI: 10.1038/nature09466. arXiv: 1010.5788 [astro-ph.HE].

Denissenkov, Pavel A. et al. (Nov. 2017). "Constraints on the Distance Moduli, Helium, and Metal Abundances, and Ages of Globular Clusters from Their RR Lyrae and Non-variable Horizontal Branch Stars. II. Multiple Stellar Populations in 47 Tuc, M3, and M13". In: ApJ 849.2, 159, p. 159. DOI: 10.3847/1538-4357/aa92c9. arXiv: 1706.05454 [astro-ph.SR].

Dotter, Aaron et al. (Jan. 2010). "The ACS Survey of Galactic Globular Clusters. IX. Horizontal Branch Morphology and the Second Parameter Phenomenon". In: ApJ 708.1, pp. 698–716. DOI: 10.1088/0004-637X/708/1/698. arXiv: 0911.2469 [astro-ph.SR].

Douglas, Andrew et al. (Mar. 2022). "Two New Black Widow Millisecond Pulsars in M28". In: ApJ 927.1, 126, p. 126. DOI: 10.3847/1538-4357/ac4744. arXiv: 2201.11238 [astro-ph.HE].

Dressel, Linda (2022). "WFC3 Instrument Handbook for Cycle 30 v. 14". In: *WFC3 Instrument Handbook for Cycle 30 v. 14*. Vol. 14, p. 14.

Driebe, T. et al. (Nov. 1998). "The evolution of helium white dwarfs. I. The companion of the millisecond pulsar PSR J1012+5307". In: A&A 339, pp. 123–133. arXiv: astro-ph/9809079 [astro-ph].

Edmonds, Peter D. et al. (Aug. 2001). "Optical Detection of a Variable Millisecond Pulsar Companion in 47 Tucanae". In: ApJ 557.1, pp. L57–L60. DOI: 10.1086/323122. arXiv: astro-ph/0107096 [astro-ph].

Eisenstein, Daniel J. et al. (Nov. 2006). "A Catalog of Spectroscopically Confirmed White Dwarfs from the Sloan Digital Sky Survey Data Release 4". In: ApJS 167.1, pp. 40–58. DOI: 10.1086/507110. arXiv: astro-ph/0606700 [astro-ph].

Ferraro, F. R. et al. (June 1992). "The galactic globular cluster NGC 5897 and its population of blue stragglers." In: MNRAS 256, pp. 376–390. DOI: 10.1093/mnras/256.3.376.

Ferraro, F. R. et al. (July 1993). "Hubble Space Telescope / Faint Object Camera Observations of the Inner Regions of the Galactic Globular Cluster M15". In: AJ 106, p. 154. DOI: 10.1086/116625.

Ferraro, F. R. et al. (Aug. 1997). "HST observations of blue Straggler stars in the core of the globular cluster M 3." In: A&A 324, pp. 915–928. arXiv: astro-ph/9703026 [astro-ph].

Ferraro, F. R. et al. (Oct. 1999). "The Giant, Horizontal, and Asymptotic Branches of Galactic Globular Clusters. I. The Catalog, Photometric Observables, and Features". In: AJ 118.4, pp. 1738–1758. DOI: 10.1086/301029. arXiv: astro-ph/9906248 [astro-ph].

Ferraro, F. R. et al. (Feb. 2003). "Accurate Mass Ratio and Heating Effects in the Dual-Line Millisecond Binary Pulsar in NGC 6397". In: ApJ 584.1, pp. L13–L16. DOI: 10.1086/368279. arXiv: astro-ph/0301244 [astro-ph].

Ferraro, F. R. et al. (Dec. 2009). "Two distinct sequences of blue straggler stars in the globular cluster M 30". In: Nature 462.7276, pp. 1028–1031. DOI: 10.1038/nature08607. arXiv: 1001.1096 [astro-ph.GA].

Ferraro, F. R. et al. (Dec. 2012). "Dynamical age differences among coeval star clusters as revealed by blue stragglers". In: Nature 492.7429, pp. 393–395. DOI: 10.1038/nature11686. arXiv: 1212.5071 [astro-ph.SR].

Ferraro, F. R. et al. (July 2015). "Probing the MSP Prenatal Stage: The Optical Identification of the X-Ray Burster EXO 1745-248 in Terzan 5". In: ApJ 807.1, L1, p. L1. DOI: 10.1088/2041-8205/807/1/L1. arXiv: 1506.03219 [astro-ph.SR].

Ferraro, F. R. et al. (Jan. 2016). "Weighing Stars: The Identification of an Evolved Blue Straggler Star in the Globular Cluster 47 Tucanae". In: ApJ 816.2, 70, p. 70. DOI: 10.3847/0004-637X/816/2/70. arXiv: 1512.00649 [astro-ph.SR].

Ferraro, F. R. et al. (June 2018). "The Hubble Space Telescope UV Legacy Survey of Galactic Globular Clusters. XV. The Dynamical Clock: Reading Cluster Dynamical Evolution from the Segregation Level of Blue Straggler Stars". In: ApJ 860.1, 36, p. 36. DOI: 10.3847/1538-4357/aac01c. arXiv: 1805.00968 [astro-ph.GA].

Ferraro, F. R. et al. (Sept. 2019). "Size diversity of old Large Magellanic Cloud clusters as determined by internal dynamical evolution". In: *Nature Astronomy* 3, pp. 1149–1155. DOI: 10.1038/s41550-019-0865-1. arXiv: 1909.02049 [astro-ph.GA].

Ferraro, Francesco R. et al. (Aug. 1997). "Hubble Space Telescope Ultraviolet Observations of the Cores of M3 and M13". In: ApJ 484.2, pp. L145–L148. DOI: 10.1086/310780.

Ferraro, Francesco R. et al. (June 1998). "Multimodal Distributions along the Horizontal Branch". In: ApJ 500.1, pp. 311–319. DOI: 10.1086/305712. arXiv: astro-ph/9708210 [astro-ph].

Ferraro, Francesco R. et al. (Nov. 2001a). "Blue Stragglers, Young White Dwarfs, and UV-Excess Stars in the Core of 47 Tucanae". In: ApJ 561.1, pp. 337–345. DOI: 10.1086/322773. arXiv: astro-ph/0107056 [astro-ph].

Ferraro, Francesco R. et al. (Nov. 2001b). "The Bright Optical Companion to the Eclipsing Millisecond Pulsar in NGC 6397". In: ApJ 561.1, pp. L93–L96. DOI: 10.1086/324563. arXiv: astro-ph/0108252 [astro-ph].

Ferraro, Francesco R. et al. (May 2003a). "Blue Straggler Stars: A Direct Comparison of Star Counts and Population Ratios in Six Galactic Globular Clusters". In: ApJ 588.1, pp. 464–477. DOI: 10.1086/374042. arXiv: astro-ph/0301261 [astro-ph].

Ferraro, Francesco R. et al. (Oct. 2003b). "The Helium White Dwarf Orbiting the Millisecond Pulsar in the Halo of the Globular Cluster NGC 6752". In: ApJ 596.2, pp. L211–L214. DOI: 10.1086/379536. arXiv: astro-ph/0309151 [astro-ph].

Ferraro, Francesco R. et al. (Mar. 2004). "Discovery of Another Peculiar Radial Distribution of Blue Stragglers in Globular Clusters: The Case of 47 Tucanae". In: ApJ 603.1, pp. 127–134. DOI: 10.1086/381229. arXiv: astro-ph/0311317 [astro-ph].

Ferraro, Francesco R. et al. (Mar. 2020). "The "dynamical clock": dating the internal dynamical evolution of star clusters with Blue Straggler Stars". In: *Rendiconti Lincei. Scienze Fisiche e Naturali* 31.1, pp. 19–31. DOI: 10.1007/s12210-020-00873-2. arXiv: 2001.07435 [astro-ph.GA].

Fonseca, Emmanuel et al. (Dec. 2016). "The NANOGrav Nine-year Data Set: Mass and Geometric Measurements of Binary Millisecond Pulsars". In: ApJ 832.2, 167, p. 167. DOI: 10.3847/0004-637X/832/2/167. arXiv: 1603.00545 [astro-ph.HE].

Foreman-Mackey, Daniel (June 2016). "corner.py: Scatterplot matrices in Python". In: *The Journal of Open Source Software* 1, p. 24. DOI: 10.21105/joss.00024.

Foreman-Mackey, Daniel et al. (Nov. 2019). "emcee v3: A Python ensemble sampling toolkit for affine-invariant MCMC". In: *The Journal of Open Source Software* 4.43, 1864, p. 1864. DOI: 10.21105/joss.01864. arXiv: 1911.07688 [astro-ph.IM].

Freire, P. C. C. et al. (Nov. 2011). "Fermi Detection of a Luminous γ-Ray Pulsar in a Globular Cluster". In: *Science* 334.6059, p. 1107. DOI: 10.1126/science.1207141. arXiv: 1111.3754 [astro-ph.GA].

Freire, P. C. C. et al. (Oct. 2017). "Long-term observations of the pulsars in 47 Tucanae - II. Proper motions, accelerations and jerks". In: MNRAS 471.1, pp. 857–876. DOI: 10.1093/mnras/stx1533. arXiv: 1706.04908 [astro-ph.HE].

Freire, Paulo C. C. et al. (Nov. 2010). "The orthometric parametrization of the Shapiro delay and an improved test of general relativity with binary pulsars". In: MNRAS 409.1, pp. 199–212. DOI: 10.1111/j.1365-2966.2010.17319.x. arXiv: 1007.0933 [astro-ph.IM].

Freire, Paulo C. C. et al. (Feb. 2014). "Direct formation of millisecond pulsars from rotationally delayed accretion-induced collapse of massive white dwarfs". In: MNRAS 438.1, pp. L86–L90. DOI: 10.1093/mnrasl/slt164. arXiv: 1311.3478 [astro-ph.SR].

Gaia Collaboration et al. (Aug. 2018). "Gaia Data Release 2. Summary of the contents and survey properties". In: A&A 616, A1, A1. DOI: 10.1051/0004-6361/201833051. arXiv: 1804.09365 [astro-ph.GA].

Gaia Collaboration et al. (July 2022). "Gaia Data Release 3: Summary of the content and survey properties". In: *arXiv e-prints*, arXiv:2208.00211, arXiv:2208.00211. DOI: 10.48550/arXiv.2208.00211. arXiv: 2208.00211 [astro-ph.GA].

Garcia-Berro, E. et al. (Dec. 1995). "The rate of change of the gravitational constant and the cooling of white dwarfs". In: MNRAS 277.3, pp. 801–810. DOI: 10.1093/mnras/277.3.801.

Garcia-Berro, Enrique et al. (Aug. 1997). "The cooling of oxygen-neon white dwarfs". In: MNRAS 289.4, pp. 973–978. DOI: 10.1093/mnras/289.4.973.

Gautam, T. et al. (Aug. 2022). "Upgraded GMRT survey for pulsars in globular clusters. I. Discovery of a millisecond binary pulsar in NGC 6652". In: A&A 664, A54, A54. DOI: 10.1051/0004-6361/202243062. arXiv: 2205.15274 [astro-ph.HE].

Gennaro, Mario (2018). "WFC3 Data Handbook v. 4". In: *WFC3 Data Handbook v. 4*. Vol. 4, p. 4.

Giddings, Steven B. et al. (Aug. 2008). "Astrophysical implications of hypothetical stable TeV-scale black holes". In: Phys. Rev. D 78.3, 035009, p. 035009. DOI: 10.1103/PhysRevD.78.035009. arXiv: 0806.3381 [hep-ph].

Goldsbury, R. et al. (Apr. 2016). "Constraining White Dwarf Structure and Neutrino Physics in 47 Tucanae". In: ApJ 821.1, 27, p. 27. DOI: 10.3847/0004-637X/821/1/27. arXiv: 1602.06286 [astro-ph.SR].

Gratton, R. G. et al. (Sept. 2005). "Precise reddening and metallicity of NGC 6752 from FLAMES spectra". In: A&A 440.3, pp. 901–908. DOI: 10.1051/0004-6361:20053019. arXiv: astro-ph/0505201 [astro-ph].

Gratton, R. G. et al. (Nov. 2010). "The connection between missing AGB stars and extended horizontal branches". In: A&A 522, A77, A77. DOI: 10.1051/0004-6361/201015405. arXiv: 1010.5913 [astro-ph.SR].

Gratton, Raffaele et al. (Sept. 2004). "Abundance Variations Within Globular Clusters". In: ARA&A 42.1, pp. 385–440. DOI: 10.1146/annurev.astro.42.053102.133945.

Gratton, Raffaele G. et al. (Feb. 2012). "Multiple populations in globular clusters. Lessons learned from the Milky Way globular clusters". In: A&A Rev. 20, 50, p. 50. DOI: 10.1007/s00159-012-0050-3. arXiv: 1201.6526 [astro-ph.SR].

Greggio, Laura et al. (Nov. 1990). "Clues on the Hot Star Content and the Ultraviolet Output of Elliptical Galaxies". In: ApJ 364, p. 35. DOI: 10.1086/169384.

Gruyters, Pieter et al. (July 2017). "First evidence of multiple populations along the AGB from Strömgren photometry". In: A&A 603, A37, A37. DOI: 10.1051/0004-6361/201630341.

Hansen, Brad M. S. et al. (Dec. 2007). "The White Dwarf Cooling Sequence of NGC 6397". In: ApJ 671.1, pp. 380–401. DOI: 10.1086/522567. arXiv: astro-ph/0701738 [astro-ph].

Harris, William E. (Oct. 1996). "A Catalog of Parameters for Globular Clusters in the Milky Way". In: AJ 112, p. 1487. DOI: 10.1086/118116.

Hermes, J. J. et al. (Oct. 2017). "White Dwarf Rotation as a Function of Mass and a Dichotomy of Mode Line Widths: Kepler Observations of 27 Pulsating DA White Dwarfs through K2 Campaign 8". In: ApJS 232.2, 23, p. 23. DOI: 10.3847/1538-4365/aa8bb5. arXiv: 1709.07004 [astro-ph.SR].

Hessels, J. W. T. et al. (Nov. 2007). "A 1.4 GHz Arecibo Survey for Pulsars in Globular Clusters". In: ApJ 670.1, pp. 363–378. DOI: 10.1086/521780. arXiv: 0707.1602 [astro-ph].

Hidalgo, Sebastian L. et al. (Apr. 2018). "The Updated BaSTI Stellar Evolution Models and Isochrones. I. Solar-scaled Calculations". In: ApJ 856.2, 125, p. 125. DOI: 10.3847/1538-4357/aab158. arXiv: 1802.07319 [astro-ph.GA].

Hills, J. G. et al. (Feb. 1976). “Stellar Collisions in Globular Clusters”. In: Astrophys. Lett. 17, p. 87.

Hong, Jongsuk et al. (Jan. 2017). “Dynamical formation of cataclysmic variables in globular clusters”. In: MNRAS 464.2, pp. 2511–2516. DOI: 10.1093/mnras/stw2595. arXiv: 1611.00779 [astro-ph.GA].

Isern, J. et al. (Aug. 2008). “Axions and the Cooling of White Dwarf Stars”. In: ApJ 682.2, p. L109. DOI: 10.1086/591042. arXiv: 0806.2807 [astro-ph].

Isern, J. et al. (Aug. 2018). “Axions and the luminosity function of white dwarfs: the thin and thick discs, and the halo”. In: MNRAS 478.2, pp. 2569–2575. DOI: 10.1093/mnras/sty1162. arXiv: 1805.00135 [astro-ph.SR].

Isern, J. et al. (Jan. 2022). “White dwarfs as Physics laboratories: lights and shadows”. In: *Frontiers in Astronomy and Space Sciences* 9, 6, p. 6. DOI: 10.3389/fspas.2022.815517. arXiv: 2202.02052 [astro-ph.HE].

Istrate, A. G. et al. (Nov. 2014a). “The formation of low-mass helium white dwarfs orbiting pulsars . Evolution of low-mass X-ray binaries below the bifurcation period”. In: A&A 571, A45, A45. DOI: 10.1051/0004-6361/201424680. arXiv: 1410.5470 [astro-ph.SR].

Istrate, A. G. et al. (Nov. 2014b). “The timescale of low-mass proto-helium white dwarf evolution”. In: A&A 571, L3, p. L3. DOI: 10.1051/0004-6361/201424681. arXiv: 1410.5471 [astro-ph.SR].

Istrate, A. G. et al. (Oct. 2016). “Models of low-mass helium white dwarfs including gravitational settling, thermal and chemical diffusion, and rotational mixing”. In: A&A 595, A35, A35. DOI: 10.1051/0004-6361/201628874. arXiv: 1606.04947 [astro-ph.SR].

Jacoby, B. A. et al. (June 2006). “Measurement of Orbital Decay in the Double Neutron Star Binary PSR B2127+11C”. In: ApJ 644.2, pp. L113–L116. DOI: 10.1086/505742. arXiv: astro-ph/0605375 [astro-ph].

Jeffery, Elizabeth J. et al. (Sept. 2016). “A Bayesian Analysis of the Ages of Four Open Clusters”. In: ApJ 828.2, 79, p. 79. DOI: 10.3847/0004-637X/828/2/79. arXiv: 1611.00835 [astro-ph.SR].

Johnson, T. J. et al. (Dec. 2013). “Broadband Pulsations from PSR B1821-24: Implications for Emission Models and the Pulsar Population of M28”. In: ApJ 778.2, 106, p. 106. DOI: 10.1088/0004-637X/778/2/106. arXiv: 1310.1852 [astro-ph.HE].

Joss, P. C. et al. (Aug. 1987). “The Core Mass–Radius Relation for Giants: A New Test of Stellar Evolution Theory”. In: ApJ 319, p. 180. DOI: 10.1086/165443.

Kaplan, D. L. et al. (July 2012). "Discovery of the Optical/Ultraviolet/Gamma-Ray Counterpart to the Eclipsing Millisecond Pulsar J1816+4510". In: ApJ 753.2, 174, p. 174. DOI: 10.1088/0004-637X/753/2/174. arXiv: 1205.3699 [astro-ph.HE].

Kepler, S. O. et al. (Jan. 2021). "The Pulsating White Dwarf G117-B15A: Still the Most Stable Optical Clock Known". In: ApJ 906.1, 7, p. 7. DOI: 10.3847/1538-4357/abc626. arXiv: 2010.16062 [astro-ph.SR].

Kilic, M. et al. (Jan. 2015). "PSR J1738+0333: the first millisecond pulsar + pulsating white dwarf binary." In: MNRAS 446, pp. L26–L30. DOI: 10.1093/mnrasl/slu152. arXiv: 1410.4898 [astro-ph.SR].

Kilic, Mukremin et al. (Dec. 2007). "The Future Is Now: The Formation of Single Low-Mass White Dwarfs in the Solar Neighborhood". In: ApJ 671.1, pp. 761–766. DOI: 10.1086/522228. arXiv: 0706.3045 [astro-ph].

Kilic, Mukremin et al. (Mar. 2017). "The Ages of the Thin Disk, Thick Disk, and the Halo from Nearby White Dwarfs". In: ApJ 837.2, 162, p. 162. DOI: 10.3847/1538-4357/aa62a5. arXiv: 1702.06984 [astro-ph.SR].

Kilic, Mukremin et al. (July 2020). "The 100 pc White Dwarf Sample in the SDSS Footprint". In: ApJ 898.1, 84, p. 84. DOI: 10.3847/1538-4357/ab9b8d. arXiv: 2006.00323 [astro-ph.SR].

King, Ivan R. (Feb. 1966). "The structure of star clusters. III. Some simple dynamical models". In: AJ 71, p. 64. DOI: 10.1086/109857.

Kippenhahn, Rudolf et al. (2013). *Stellar Structure and Evolution*. DOI: 10.1007/978-3-642-30304-3.

Kirichenko, A. Yu et al. (Feb. 2020). "Searching for optical companions to four binary millisecond pulsars with the Gran Telescopio Canarias". In: MNRAS 492.2, pp. 3032–3040. DOI: 10.1093/mnras/staa066. arXiv: 2001.02722 [astro-ph.SR].

Koester, D. (Jan. 2010). "White dwarf spectra and atmosphere models". In: Mem. Soc. Astron. Italiana 81, pp. 921–931.

Kulkarni, S. R. et al. (Jan. 1991). "Old pulsars in the low-density globular clusters MI3 and M53". In: Nature 349.6304, pp. 47–49. DOI: 10.1038/349047a0.

Lanzoni, B. et al. (July 2007a). "The Blue Straggler Population of the Globular Cluster M5". In: ApJ 663.1, pp. 267–276. DOI: 10.1086/518592. arXiv: 0704.0139 [astro-ph].

Lanzoni, B. et al. (Oct. 2007b). "The Surface Density Profile of NGC 6388: A Good Candidate for Harboring an Intermediate-Mass Black Hole". In: ApJ 668.2, pp. L139–L142. DOI: 10.1086/522927. arXiv: 0709.0119 [astro-ph].

Lanzoni, B. et al. (July 2010). "New Density Profile and Structural Parameters of the Complex Stellar System Terzan 5". In: ApJ 717.2, pp. 653–657. DOI: 10.1088/0004-637X/717/2/653. arXiv: 1005.2847 [astro-ph.GA].

Lanzoni, B. et al. (Dec. 2016). "Refining the Dynamical Clock for Star Clusters". In: ApJ 833.2, L29, p. L29. DOI: 10.3847/2041-8213/833/2/L29.

Lanzoni, B. et al. (July 2018). "The Strong Rotation of M5 (NGC 5904) as Seen from the MIKiS Survey of Galactic Globular Clusters". In: ApJ 861.1, 16, p. 16. DOI: 10.3847/1538-4357/aac26a. arXiv: 1804.10509 [astro-ph.GA].

Lanzoni, Barbara et al. (Dec. 2019). "Star-density Profiles of Six Old Star Clusters in the Large Magellanic Cloud". In: ApJ 887.2, 176, p. 176. DOI: 10.3847/1538-4357/ab54c2. arXiv: 1911.01928 [astro-ph.GA].

Lapenna, E. et al. (July 2016). "Lost and Found: Evidence of Second-generation Stars Along the Asymptotic Giant Branch of the Globular Cluster NGC 6752". In: ApJ 826.1, L1, p. L1. DOI: 10.3847/2041-8205/826/1/L1. arXiv: 1606.09256 [astro-ph.SR].

Lattimer, J. M. et al. (Mar. 2001). "Neutron Star Structure and the Equation of State". In: ApJ 550.1, pp. 426–442. DOI: 10.1086/319702. arXiv: astro-ph/0002232 [astro-ph].

Lattimer, James M. (Nov. 2012). "The Nuclear Equation of State and Neutron Star Masses". In: *Annual Review of Nuclear and Particle Science* 62.1, pp. 485–515. DOI: 10.1146/annurev-nucl-102711-095018. arXiv: 1305.3510 [nucl-th].

Lattimer, James M. et al. (Apr. 2007). "Neutron star observations: Prognosis for equation of state constraints". In: Phys. Rep. 442.1-6, pp. 109–165. DOI: 10.1016/j.physrep.2007.02.003. arXiv: astro-ph/0612440 [astro-ph].

Leonard, Peter J. T. (July 1989). "Stellar Collisions in Globular Clusters and the Blue Straggler Problem". In: AJ 98, p. 217. DOI: 10.1086/115138.

Libralato, Mattia et al. (Aug. 2022). "The Hubble Space Telescope UV Legacy Survey of Galactic Globular Clusters. XXIII. Proper-motion Catalogs and Internal Kinematics". In: ApJ 934.2, 150, p. 150. DOI: 10.3847/1538-4357/ac7727. arXiv: 2206.09924 [astro-ph.GA].

Lin, Jinrong et al. (May 2011). "LMXB and IMXB Evolution: I. The Binary Radio Pulsar PSR J1614-2230". In: ApJ 732.2, 70, p. 70. DOI: 10.1088/0004-637X/732/2/70. arXiv: 1012.1877 [astro-ph.HE].

Lorimer, D. R. et al. (2012). *Handbook of Pulsar Astronomy*.

Lyne, A. G. et al. (July 1987). "The discovery of a millisecond pulsar in the globular cluster M28". In: Nature 328.6129, pp. 399–401. DOI: 10.1038/328399a0.

Lyne, Andrew G. et al. (1998). *Pulsar astronomy*.

Malec, Beata et al. (Nov. 2001). "White Dwarfs as a Source of Constraints on Exotic Physics". In: *Acta Physica Polonica B* 32.11, p. 3683.

Mata Sánchez, D. et al. (May 2020). "PSR J1012+5307: a millisecond pulsar with an extremely low-mass white dwarf companion". In: MNRAS 494.3, pp. 4031–4042. DOI: 10.1093/mnras/staa983. arXiv: 2004.02901 [astro-ph.HE].

Maxted, Pierre F. L. et al. (June 2013). "Multi-periodic pulsations of a stripped red-giant star in an eclipsing binary system". In: Nature 498.7455, pp. 463–465. DOI: 10.1038/nature12192. arXiv: 1307.1654 [astro-ph.SR].

McCrea, W. H. (Jan. 1964). "Extended main-sequence of some stellar clusters". In: MNRAS 128, p. 147. DOI: 10.1093/mnras/128.2.147.

Mestel, L. (Jan. 1952). "On the theory of white dwarf stars. I. The energy sources of white dwarfs". In: MNRAS 112, p. 583. DOI: 10.1093/mnras/112.6.583.

Meurer, Gerhardt R. et al. (Feb. 2003). "Calibration of geometric distortion in the ACS detectors". In: *Future EUV/UV and Visible Space Astrophysics Missions and Instrumentation.* Ed. by J. Chris Blades et al. Vol. 4854. Society of Photo-Optical Instrumentation Engineers (SPIE) Conference Series, pp. 507–514. DOI: 10.1117/12.460259.

Miller Bertolami, Marcelo M. et al. (Sept. 2013). "Quiescent Nuclear Burning in Low-metallicity White Dwarfs". In: ApJ 775.1, L22, p. L22. DOI: 10.1088/2041-8205/775/1/L22. arXiv: 1308.2062 [astro-ph.SR].

Milone, A. P. et al. (Jan. 2017). "The Hubble Space Telescope UV Legacy Survey of Galactic globular clusters - IX. The Atlas of multiple stellar populations". In: MNRAS 464.3, pp. 3636–3656. DOI: 10.1093/mnras/stw2531. arXiv: 1610.00451 [astro-ph.SR].

Milone, A. P. et al. (Dec. 2018). "The Hubble Space Telescope UV legacy survey of galactic globular clusters - XVI. The helium abundance of multiple populations". In: MNRAS 481.4, pp. 5098–5122. DOI: 10.1093/mnras/sty2573. arXiv: 1809.05006 [astro-ph.SR].

Miocchi, P. et al. (Sept. 2013). "Star Count Density Profiles and Structural Parameters of 26 Galactic Globular Clusters". In: ApJ 774.2, 151, p. 151. DOI: 10.1088/0004-637X/774/2/151. arXiv: 1307.6035 [astro-ph.GA].

Moehler, S. et al. (June 2008). "White Dwarfs in Globular Clusters". In: *arXiv e-prints*, arXiv:0806.4456, arXiv:0806.4456. arXiv: 0806.4456 [astro-ph].

Mucciarelli, A. et al. (Aug. 2013). "New Clues on the Nature of the Companion to PSR J1740-5340 in NGC 6397 from XSHOOTER Spectroscopy". In: ApJ 772.2, L27, p. L27. DOI: 10.1088/2041-8205/772/2/L27. arXiv: 1307.0919 [astro-ph.SR].

Mucciarelli, A. et al. (Jan. 2019). "Confirming the Presence of Second-population Stars and the Iron Discrepancy along the AGB of the Globular Cluster NGC 6752". In: ApJ 870.2, 124, p. 124. DOI: 10.3847/1538-4357/aaf3a4. arXiv: 1811.10626 [astro-ph.SR].

Nardiello, D. et al. (Dec. 2018). "The Hubble Space Telescope UV Legacy Survey of Galactic Globular Clusters - XVII. Public Catalogue Release". In: MNRAS 481.3, pp. 3382–3393. DOI: 10.1093/mnras/sty2515. arXiv: 1809.04300 [astro-ph.SR].

Nguyen, C. T. et al. (Sept. 2022). "PARSEC V2.0: Stellar tracks and isochrones of low- and intermediate-mass stars with rotation". In: A&A 665, A126, A126. DOI: 10.1051/0004-6361/202244166. arXiv: 2207.08642 [astro-ph.SR].

Nomoto, Ken'ichi (Nov. 1987). "Evolution of 8–10 M_{sun} Stars toward Electron Capture Supernovae. II. Collapse of an O + NE + MG Core". In: ApJ 322, p. 206. DOI: 10.1086/165716.

O'Donnell, James E. (Feb. 1994). "R v-dependent Optical and Near-Ultraviolet Extinction". In: ApJ 422, p. 158. DOI: 10.1086/173713.

Özel, Feryal et al. (Sept. 2016). "Masses, Radii, and the Equation of State of Neutron Stars". In: ARA&A 54, pp. 401–440. DOI: 10.1146/annurev-astro-081915-023322. arXiv: 1603.02698 [astro-ph.HE].

Pallanca, C. et al. (Dec. 2010). "The Optical Companion to the Binary Millisecond Pulsar J1824-2452H in the Globular Cluster M28". In: ApJ 725.1, pp. 1165–1169. DOI: 10.1088/0004-637X/725/1/1165. arXiv: 1010.2661 [astro-ph.SR].

Pallanca, C. et al. (Aug. 2013a). "The Optical Companion to the Intermediate-mass Millisecond Pulsar J1439-5501 in the Galactic Field". In: ApJ 773.2, 127, p. 127. DOI: 10.1088/0004-637X/773/2/127. arXiv: 1306.3787 [astro-ph.SR].

Pallanca, C. et al. (Aug. 2013b). "The Optical Counterpart to the X-Ray Transient IGR J1824-24525 in the Globular Cluster M28". In: ApJ 773.2, 122, p. 122. DOI: 10.1088/0004-637X/773/2/122. arXiv: 1306.6416 [astro-ph.SR].

Pallanca, C. et al. (Nov. 2014). "Radio Timing and Optical Photometry of the Black Widow System PSR J1518+0204C in the Globular Cluster M5". In: ApJ 795.1, 29, p. 29. DOI: 10.1088/0004-637X/795/1/29. arXiv: 1409.1424 [astro-ph.SR].

Papitto, A. et al. (Sept. 2013). "Swings between rotation and accretion power in a binary millisecond pulsar". In: Nature 501.7468, pp. 517–520. DOI: 10.1038/nature12470. arXiv: 1305.3884 [astro-ph.HE].

Parsons, Steven G. et al. (Mar. 2020). "A pulsating white dwarf in an eclipsing binary". In: *Nature Astronomy* 4, pp. 690–696. DOI: 10.1038/s41550-020-1037-z. arXiv: 2003.07371 [astro-ph.SR].

Paxton, Bill et al. (Jan. 2011). "Modules for Experiments in Stellar Astrophysics (MESA)". In: ApJS 192.1, 3, p. 3. DOI: 10.1088/0067-0049/192/1/3. arXiv: 1009.1622 [astro-ph.SR].

Paxton, Bill et al. (Sept. 2013). "Modules for Experiments in Stellar Astrophysics (MESA): Planets, Oscillations, Rotation, and Massive Stars". In: ApJS 208.1, 4, p. 4. DOI: 10.1088/0067-0049/208/1/4. arXiv: 1301.0319 [astro-ph.SR].

Paxton, Bill et al. (Sept. 2015). "Modules for Experiments in Stellar Astrophysics (MESA): Binaries, Pulsations, and Explosions". In: ApJS 220.1, 15, p. 15. DOI: 10.1088/0067-0049/220/1/15. arXiv: 1506.03146 [astro-ph.SR].

Paxton, Bill et al. (Feb. 2018). "Modules for Experiments in Stellar Astrophysics (MESA): Convective Boundaries, Element Diffusion, and Massive Star Explosions". In: ApJS 234.2, 34, p. 34. DOI: 10.3847/1538-4365/aaa5a8. arXiv: 1710.08424 [astro-ph.SR].

Pietrinferni, Adriano et al. (Sept. 2004). "A Large Stellar Evolution Database for Population Synthesis Studies. I. Scaled Solar Models and Isochrones". In: ApJ 612.1, pp. 168–190. DOI: 10.1086/422498. arXiv: astro-ph/0405193 [astro-ph].

— (May 2006). "A Large Stellar Evolution Database for Population Synthesis Studies. II. Stellar Models and Isochrones for an α-enhanced Metal Distribution". In: ApJ 642.2, pp. 797–812. DOI: 10.1086/501344. arXiv: astro-ph/0603721 [astro-ph].

Pietrinferni, Adriano et al. (Feb. 2021). "Updated BaSTI Stellar Evolution Models and Isochrones. II. α-enhanced Calculations". In: ApJ 908.1, 102, p. 102. DOI: 10.3847/1538-4357/abd4d5. arXiv: 2012.10085 [astro-ph.SR].

Piotto, G. et al. (Mar. 2015). "The Hubble Space Telescope UV Legacy Survey of Galactic Globular Clusters. I. Overview of the Project and Detection of Multiple Stellar Populations". In: AJ 149.3, 91, p. 91. DOI: 10.1088/0004-6256/149/3/91. arXiv: 1410.4564 [astro-ph.SR].

Portegies Zwart, Simon et al. (May 2019). "A Triple Origin for Twin Blue Stragglers in Close Binaries". In: ApJ 876.2, L33, p. L33. DOI: 10.3847/2041-8213/ab1b75. arXiv: 1901.11088 [astro-ph.SR].

Prager, Brian J. et al. (Aug. 2017). "Using Long-term Millisecond Pulsar Timing to Obtain Physical Characteristics of the Bulge Globular Cluster Terzan 5". In: ApJ 845.2, 148, p. 148. DOI: 10.3847/1538-4357/aa7ed7. arXiv: 1612.04395 [astro-ph.SR].

Ransom, Scott M. et al. (Feb. 2005). "Twenty-One Millisecond Pulsars in Terzan 5 Using the Green Bank Telescope". In: *Science* 307.5711, pp. 892–896. DOI: 10.1126/science.1108632. arXiv: astro-ph/0501230 [astro-ph].

Rappaport, S. et al. (Apr. 1995). "The relation between white dwarf mass and orbital period in wide binary radio pulsars". In: MNRAS 273.3, pp. 731–741. DOI: 10.1093/mnras/273.3.731.

Raso, S. et al. (Apr. 2017). "The "UV-route" to Search for Blue Straggler Stars in Globular Clusters: First Results from the HST UV Legacy Survey". In: ApJ 839.1, 64, p. 64. DOI: 10.3847/1538-4357/aa6891. arXiv: 1704.01453 [astro-ph.SR].

Raso, Silvia et al. (May 2020). "A Kinematic View of NGC 1261: Structural Parameters, Internal Dispersion, Absolute Proper Motion, and Blue Straggler Stars". In: ApJ 895.1, 15, p. 15. DOI: 10.3847/1538-4357/ab8ae7. arXiv: 2004.09540 [astro-ph.SR].

Renedo, I. et al. (July 2010). "New Cooling Sequences for Old White Dwarfs". In: ApJ 717.1, pp. 183–195. DOI: 10.1088/0004-637X/717/1/183. arXiv: 1005.2170 [astro-ph.SR].

Renzini, Alvio (July 2017). "Finding forming globular clusters at high redshifts". In: MNRAS 469.1, pp. L63–L67. DOI: 10.1093/mnrasl/slx057. arXiv: 1704.04883 [astro-ph.GA].

Renzini, Alvio et al. (Jan. 1986). "Global properties of stellar populations and the spectral evolution of galaxies." In: *Spectral Evolution of Galaxies*. Ed. by Cesare Chiosi et al. Vol. 122. Astrophysics and Space Science Library, pp. 195–231. DOI: 10.1007/978-94-009-4598-2_19.

Richer, Harvey B. et al. (June 2008). "Deep Advanced Camera for Surveys Imaging in the Globular Cluster NGC 6397: the Cluster Color-Magnitude Diagram and Luminosity Function". In: AJ 135.6, pp. 2141–2154. DOI: 10.1088/0004-6256/135/6/2141. arXiv: 0708.4030 [astro-ph].

Richer, Harvey B. et al. (Dec. 2013). "Comparing the White Dwarf Cooling Sequences in 47 Tuc and NGC 6397". In: ApJ 778.2, 104, p. 104. DOI: 10.1088/0004-637X/778/2/104. arXiv: 1310.0111 [astro-ph.SR].

Ridolfi, A. et al. (Dec. 2019). "Upgraded Giant Metrewave Radio Telescope timing of NGC 1851A: a possible millisecond pulsar - neutron star system". In: MNRAS 490.3, pp. 3860–3874. DOI: 10.1093/mnras/stz2645. arXiv: 1909.06163 [astro-ph.HE].

Ridolfi, A. et al. (Aug. 2022). "TRAPUM discovery of 13 new pulsars in NGC 1851 using MeerKAT". In: A&A 664, A27, A27. DOI: 10.1051/0004-6361/202143006. arXiv: 2203.12302 [astro-ph.HE].

Rivera Sandoval, L. E. et al. (Apr. 2018). "New cataclysmic variables and other exotic binaries in the globular cluster 47 Tucanae*". In: MNRAS 475.4, pp. 4841–4867. DOI: 10.1093/mnras/sty058. arXiv: 1705.07100 [astro-ph.SR].

Roberts, Mallory S. E. (Mar. 2013). "Surrounded by spiders! New black widows and redbacks in the Galactic field". In: *Neutron Stars and Pulsars: Challenges and Opportunities after 80 years*. Ed. by Joeri van Leeuwen. Vol. 291, pp. 127–132. DOI: 10.1017/S174392131202337X. arXiv: 1210.6903 [astro-ph.HE].

Roberts, Mallory S. E. et al. (Aug. 2018). "X-Ray and Optical Properties of Black Widows and Redbacks". In: *Pulsar Astrophysics the Next Fifty Years*. Ed. by P. Weltevrede et al. Vol. 337, pp. 43–46. DOI: 10.1017/S1743921318000480. arXiv: 1801.09903 [astro-ph.HE].

Sabbi, E. et al. (Dec. 2003a). "The chemical composition of the peculiar companion to the millisecond pulsar in NGC 6397". In: A&A 412, pp. 829–836. DOI: 10.1051/0004-6361:20031475. arXiv: astro-ph/0309541 [astro-ph].

Sabbi, E. et al. (May 2003b). "The Complex Hα Line Profile of the Bright Companion to PSR J1740-5340 in NGC 6397". In: ApJ 589.1, pp. L41–L44. DOI: 10.1086/375729. arXiv: astro-ph/0304159 [astro-ph].

Sabbi, E. et al. (Dec. 2004). "The Small Blue Straggler Star Population in the Dense Galactic Globular Cluster NGC 6752". In: ApJ 617.2, pp. 1296–1306. DOI: 10.1086/425492. arXiv: astro-ph/0409001 [astro-ph].

Salaris, M. et al. (June 2002). "Homogeneous age dating of 55 Galactic globular clusters. Clues to the Galaxy formation mechanisms". In: A&A 388, pp. 492–503. DOI: 10.1051/0004-6361:20020554. arXiv: astro-ph/0204410 [astro-ph].

Salaris, M. et al. (June 2010). "A Large Stellar Evolution Database for Population Synthesis Studies. VI. White Dwarf Cooling Sequences". In: ApJ 716.2, pp. 1241–1251. DOI: 10.1088/0004-637X/716/2/1241. arXiv: 1005.1791 [astro-ph.SR].

Salaris, M. et al. (July 2013). "Comparison of theoretical white dwarf cooling timescales". In: A&A 555, A96, A96. DOI: 10.1051/0004-6361/201220622. arXiv: 1306.2575 [astro-ph.SR].

Salaris, Maurizio et al. (Feb. 2022). "The updated BASTI stellar evolution models and isochrones - III. White dwarfs". In: MNRAS 509.4, pp. 5197–5208. DOI: 10.1093/mnras/stab3359. arXiv: 2111.09285 [astro-ph.SR].

Sandage, A. R. (Jan. 1953). "The color-magnitude diagram for the globular cluster M 3." In: AJ 58, pp. 61–75. DOI: 10.1086/106822.

Sandquist, Eric L. et al. (Aug. 2004). "Exploring the Upper Red Giant and Asymptotic Giant Branches: The Globular Cluster M5". In: ApJ 611.1, pp. 323–337. DOI: 10.1086/422134. arXiv: astro-ph/0404447 [astro-ph].

Sandquist, Eric L. et al. (June 2010). "A Re-evaluation of the Evolved Stars in the Globular Cluster M13". In: AJ 139.6, pp. 2374–2409. DOI: 10.1088/0004-6256/139/6/2374. arXiv: 1003.5942 [astro-ph.SR].

Sarajedini, Ata et al. (Apr. 2007). "The ACS Survey of Galactic Globular Clusters. I. Overview and Clusters without Previous Hubble Space Telescope Photometry". In: AJ 133.4, pp. 1658–1672. DOI: 10.1086/511979. arXiv: astro-ph/0612598 [astro-ph].

Savonije, G. J. (Jan. 1987). "A determination of the white-dwarf masses in wide binary radio-pulsar systems". In: Nature 325.6103, pp. 416–418. DOI: 10.1038/325416a0.

Stappers, B. W. et al. (July 2014). "A State Change in the Missing Link Binary Pulsar System PSR J1023+0038". In: ApJ 790.1, 39, p. 39. DOI: 10.1088/0004-637X/790/1/39. arXiv: 1311.7506 [astro-ph.HE].

Steiner, Andrew W. et al. (Oct. 2010). "The Equation of State from Observed Masses and Radii of Neutron Stars". In: ApJ 722.1, pp. 33–54. DOI: 10.1088/0004-637X/722/1/33. arXiv: 1005.0811 [astro-ph.HE].

Stetson, Peter B. (Mar. 1987). "DAOPHOT: A Computer Program for Crowded-Field Stellar Photometry". In: PASP 99, p. 191. DOI: 10.1086/131977.

— (Mar. 1994). "The Center of the Core-Cusp Globular Cluster M15: CFHT and HST Observations, ALLFRAME Reductions". In: PASP 106, p. 250. DOI: 10.1086/133378.

STScI Development Team (Mar. 2013). *pysynphot: Synthetic photometry software package*. Astrophysics Source Code Library, record ascl:1303.023. ascl: 1303.023.

Su, Wen-Chao et al. (Aug. 2021). "A triplet of the only pulsation mode detected in the DAV star G132-12". In: *Research in Astronomy and Astrophysics* 21.6, 139, p. 139. DOI: 10.1088/1674-4527/21/6/139. arXiv: 2107.03023 [astro-ph.SR].

Tassoul, M. et al. (Feb. 1990). "Evolutionary Models for Pulsation Studies of White Dwarfs". In: ApJS 72, p. 335. DOI: 10.1086/191420.

Tauris, T. M. et al. (2006). "Formation and evolution of compact stellar X-ray sources". In: *Compact stellar X-ray sources*. Vol. 39, pp. 623–665.

Tauris, T. M. et al. (Sept. 2011). "Formation of millisecond pulsars with CO white dwarf companions - I. PSR J1614-2230: evidence for a neutron star born massive". In: MNRAS 416.3, pp. 2130–2142. DOI: 10.1111/j.1365-2966.2011.19189.x. arXiv: 1103.4996 [astro-ph.SR].

— (Sept. 2012). "Formation of millisecond pulsars with CO white dwarf companions - II. Accretion, spin-up, true ages and comparison to MSPs with He white dwarf companions". In: MNRAS 425.3, pp. 1601–1627. DOI: 10.1111/j.1365-2966.2012.21446.x. arXiv: 1206.1862 [astro-ph.SR].

Tauris, T. M. et al. (Oct. 2013). "Evolution towards and beyond accretion-induced collapse of massive white dwarfs and formation of millisecond pulsars". In: A&A 558, A39, A39. DOI: 10.1051/0004-6361/201321662. arXiv: 1308.4887 [astro-ph.SR].

Tauris, T. M. et al. (Sept. 2017). "Formation of Double Neutron Star Systems". In: ApJ 846.2, 170, p. 170. DOI: 10.3847/1538-4357/aa7e89. arXiv: 1706.09438 [astro-ph.HE].

Tauris, Thomas M. (Feb. 2012). "Spin-Down of Radio Millisecond Pulsars at Genesis". In: *Science* 335.6068, p. 561. DOI: 10.1126/science.1216355. arXiv: 1202.0551 [astro-ph.SR].

Tauris, Thomas M. et al. (Oct. 1999). "Formation of millisecond pulsars. I. Evolution of low-mass X-ray binaries with P_orb> 2 days". In: A&A 350, pp. 928–944. arXiv: astro-ph/9909147 [astro-ph].

Tremblay, P. -E. et al. (May 2009). "Spectroscopic Analysis of DA White Dwarfs: Stark Broadening of Hydrogen Lines Including Nonideal Effects". In: ApJ 696.2, pp. 1755–1770. DOI: 10.1088/0004-637X/696/2/1755. arXiv: 0902.4182 [astro-ph.SR].

van Kerkwijk, M. H. et al. (July 2005). "Optical Studies of Companions to Millisecond Pulsars". In: *Binary Radio Pulsars*. Ed. by Fred A. Rasio et al. Vol. 328. Astronomical Society of the Pacific Conference Series, p. 357. arXiv: astro-ph/0405283 [astro-ph].

VandenBerg, Don A. et al. (Oct. 2013). "The Ages of 55 Globular Clusters as Determined Using an Improved ΔV_{TO}^{HB} Method along with Color-Magnitude Diagram Constraints, and Their Implications for Broader Issues". In: ApJ 775.2, 134, p. 134. DOI: 10.1088/0004-637X/775/2/134. arXiv: 1308.2257 [astro-ph.GA].

Wang, Bo et al. (Mar. 2022). "Formation of millisecond pulsars with long orbital periods by accretion-induced collapse of white dwarfs". In: MNRAS 510.4, pp. 6011–6021. DOI: 10.1093/mnras/stac114. arXiv: 2201.03827 [astro-ph.SR].

Wang, Lin et al. (Mar. 2020). “Discovery and Timing of Pulsars in the Globular Cluster M13 with FAST”. In: ApJ 892.1, 43, p. 43. DOI: 10.3847/1538-4357/ab76cc. arXiv: 2002.05938 [astro-ph.HE].

Wijnands, Rudy et al. (July 1998). “A millisecond pulsar in an X-ray binary system”. In: Nature 394.6691, pp. 344–346. DOI: 10.1038/28557.

Winget, D. E. et al. (Sept. 2008). “Pulsating white dwarf stars and precision asteroseismology.” In: ARA&A 46, pp. 157–199. DOI: 10.1146/annurev.astro.46.060407.145250. arXiv: 0806.2573 [astro-ph].

Woosley, S. E. et al. (Sept. 2015). “The Remarkable Deaths of 9-11 Solar Mass Stars”. In: ApJ 810.1, 34, p. 34. DOI: 10.1088/0004-637X/810/1/34. arXiv: 1505.06712 [astro-ph.SR].

Zhang, Pengfei et al. (Aug. 2022). “Discovery of γ-Ray Pulsations from PSR J1835-3259B in the Globular Cluster NGC 6652”. In: ApJ 935.2, L36, p. L36. DOI: 10.3847/2041-8213/ac88bf. arXiv: 2206.13667 [astro-ph.HE].

Zinn, R. et al. (Nov. 1976). “The masses of the anomalous cepheids in the Draco system.” In: ApJ 209, pp. 734–747. DOI: 10.1086/154772.

List of Figures

List of Tables

List of Acronyms

ACS Advanced Camera for Surveys. 16, 19, 86

AGB Asymptotic Giant Branch. 9, 25, 28, 32, 38, 39, 44, 46, 47, 56, 61–63, 66, 67, 69, 81, 82, 150

BaSTI a Bag of Stellar Tracks and Isochrones. 25, 27, 36, 38, 39, 90, 107, 148

BSS Blue Straggle Star. 5, 34, 37, 105

CMD Color Magnitude Diagram. 3, 4, 13, 23, 28, 34, 38, 49–52, 54, 56, 69, 71, 74, 75, 89, 90, 100, 106, 109, 110, 150–152, 155

CO Carbon-Oxygen. 11, 13, 25, 74, 107

CTE Charge Transfer Efficiency. 18, 33, 48, 68, 104

ELM WDs Extremely low-mass white dwarfs. 13

FOC Faint Object Camera. 19

GCs Globular Clusters. i, 1, 4, 10, 12, 14, 16, 22, 45, 47, 67, 81, 84, 85, 94, 103, 115

HB Horizontal Branch. vi, 9, 22, 23, 25, 28, 31, 32, 34, 36–39, 44, 66–69, 81, 82, 117, 150

HR-diagram Hertzsprung–Russell Diagram. 3, 11, 12, 147

HST Hubble Space Telescope. i, 16, 17, 21, 23, 33, 48, 67–69, 78, 86, 103, 104, 106, 110, 114, 115, 147

IR Infrared channel. 18

LF Luminosity Function. 13, 16, 22, 28, 32, 34, 45, 66, 117

LMXBs Low-Mass X-ray Binaries. 14

MS Main Sequence. 5

MS-TO Main Sequence Turn-Off Stars. 7, 23, 27, 34, 37, 48, 148

MSPs Millisecond pulars. 14–16, 83–85, 87, 90, 94, 103, 106, 114, 115, 117

NGC New General Catalogue. 41, 46, 104, 118, 122

NSs Neutron Stars. 14, 15, 83–85, 100

PSF Point Spread Function. 33, 48, 68, 105

RGB Red Giant Branch. 7, 23, 24, 29–31, 35–39, 42, 49, 148, 149

SGB Sub-Giant Branch. 7

SSP Simple Stellar Population. 1, 4

UVIS Ultraviolet-Visible channels. 18, 23, 33, 68, 104

WDCS White Dwarf Cooling Sequence. 117

WDs White Dwarfs. i, vi, 10, 11, 16, 21–25, 27, 28, 30–33, 36–39, 45–48, 53, 54, 56, 58, 59, 61–63, 65–68, 71, 72, 74–76, 78, 80–82, 88, 94, 95, 100, 105–107, 148, 150–152

WFC3 Wide Field Camera 3. 16, 18, 23, 27, 33, 38, 48, 68, 78, 86, 104, 110, 148

WFPC2 Wide Field Planetary Camera 2. 18